

ABLATION MODELING FOR HIGH SPEED INTERNAL AND EXTERNAL
FLOWS

A THESIS SUBMITTED TO
THE GRADUATE SCHOOL OF NATURAL AND APPLIED SCIENCES
OF
MIDDLE EAST TECHNICAL UNIVERSITY

BY

OĞUZ KAAN ONAY

IN PARTIAL FULFILLMENT OF THE REQUIREMENTS
FOR
THE DEGREE OF DOCTOR OF PHILOSOPHY
IN
AEROSPACE ENGINEERING

JANUARY 2020

Approval of the thesis:

ABLATION MODELING FOR HIGH SPEED INTERNAL AND EXTERNAL FLOWS

submitted by **OĞUZ KAAN ONAY** in partial fulfillment of the requirements for the degree of **Doctor of Philosophy in Aerospace Engineering Department, Middle East Technical University** by,

Prof. Dr. Halil Kalıpçılar
Dean, Graduate School of **Natural and Applied Sciences**

Prof. Dr. İsmail Hakkı Tuncer
Head of Department, **Aerospace Engineering**

Prof. Dr. Sinan Eyi
Supervisor, **Aerospace Engineering, METU**

Examining Committee Members:

Prof. Dr. Yusuf Özyörük
Aerospace Engineering, METU

Prof. Dr. Sinan Eyi
Aerospace Engineering, METU

Prof. Dr. Oğuz Uzol
Aerospace Engineering, METU

Assist. Prof. Dr. Sıtkı Uslu
Mechanical Engineering, TOBB-ETU

Assist. Prof. Dr. Onur Baş
Mechanical Engineering, TED University

Date: 15.01.2020

I hereby declare that all information in this document has been obtained and presented in accordance with academic rules and ethical conduct. I also declare that, as required by these rules and conduct, I have fully cited and referenced all material and results that are not original to this work.

Name, Surname: Oğuz Kaan Onay

Signature:

ABSTRACT

ABLATION MODELING FOR HIGH SPEED INTERNAL AND EXTERNAL FLOWS

Onay, Oğuz Kaan
Doctor of Philosophy, Aerospace Engineering
Supervisor: Prof. Dr. Sinan Eyi

January 2020, 120 pages

In this thesis study, the ablation of graphitic materials is modeled and two different analysis tools are developed. In the first model, the computations are conducted with a decoupled approach. Secondly, a more generalized calculation method is introduced via coupling the flow field and solid conduction analysis codes. In the modeling studies, both the gas and solid domains are assumed to be axisymmetric and the physical domains are discretized with structured finite volume cells. For the flow field analyses, Godunov type approximate Riemann solvers are used for the convective flux calculations and the gradient terms of the viscous fluxes are calculated with the help of grid transformation metrics. Mass diffusion terms are included in the Navier-Stokes equations. Baldwin-Lomax, Baldwin-Barth and Spalart-Allmaras turbulence models are implemented and the results are compared for the coupled approach. A linear solver is developed for the computation of gas phase chemical reaction source terms. The effects of the solid thermal properties with temperature are not neglected in the computations. The models are tested for hypersonic air and Solid Rocket Motor (SRM) nozzle flow conditions. Wall equilibrium is assumed for graphite in air problem and an implicit solver is developed for the calculation of surface species mass fractions rather than using previously prepared lookup tables. Both equilibrium and

finite rate surface thermochemistry approaches are tested for the internal flows of the SRM nozzles.

Keywords: Graphite, Ablation, Reactive Flows, Riemann Solver, Conjugate Heat Transfer

ÖZ

YÜKSEK HIZLI İÇ VE DIŞ AKIŞLAR İÇİN ISIL AŞINMANIN MODELLENMESİ

Onay, Oğuz Kaan
Doktora, Havacılık ve Uzay Mühendisliği
Tez Danışmanı: Prof. Dr. Sinan Eyi

Ocak 2020, 120 sayfa

Bu tez çalışmasında, karbon bazlı malzemelerin aşınması modellenmiş ve iki farklı hesaplama aracı geliştirilmiştir. İlk modelleme çalışmasında hesaplamalar bütünleşik olmayan bir yaklaşımla yürütülmüştür. Sonrasında, akış ve katıda ısı iletimi kodlarının bütünleştirilmesiyle daha genelleştirilmiş bir hesaplama yöntemi ortaya konmuştur. Modelleme çalışmalarında hem akış hem de katı bölgelerin eksenel simetrik olduğu varsayılmış ve fiziksel bölgeler yapısal sonlu hacimlerin kullanılmasıyla ayrıklaştırılmıştır. Akış çözümlerinde viskoz olmayan akı hesaplamaları için Godunov tipi yaklaşık Riemann çözücüler kullanılmış, viskoz akı terimlerinin hesaplanmasında ise ağ dönüşüm metriklerinden faydalanılmıştır. Navier-Stokes denklemlerine kütle difüzyonu terimleri dahil edilmiştir. Akış hesaplamalarında Baldwin-Lomax, Baldwin-Barth ve Spalart-Allmaras türbülans modelleri kullanılmıştır ve sonuçlar bu üç model için karşılaştırılmıştır. Gaz fazı kimyasal tepkimelerinin kaynak terimlerinin hesaplanabilmesi için yeni bir çözücü geliştirilmiştir. Katı bölgede ısı iletimi hesaplamalarında malzemenin termal özelliklerinin sıcaklıkla değişimi ihmal edilmemiştir. Modeller, hipersonik hava akışı ve katı yakıtlı roket motorlarının lülelerindeki iç akış şartları için test edilmiştir. Grafitin hava içerisinde aşınması problemi için duvarda kimyasal denge varsayımı yapılmış ve duvar türlerinin kütle oranlarının hesaplanabilmesi amacıyla kapalı formülasyon kullanan bir çözücü

geliştirilmiştir. Bu problemin kimyasal denge hesaplamalarında önceden hazırlanmış interpolasyon tabloları kullanılmamıştır. Katı yakıtlı roket motorlarının lülelerindeki iç akış problemleri için, aşınan duvarda hem kimyasal denge hem de sonlu hızlı yüzey termokimyası yaklaşımları test edilmiştir.

Anahtar Kelimeler: Grafit, Isıl Aşınma, Tepkimeli Akış, Riemann Çözücü, Akuple Isı Transferi

...to the little twinkle in the eye of my daughter Ferah Feza!

ACKNOWLEDGEMENTS

First of all, I want to thank my supervisor Prof. Dr. Sinan Eyi for sharing his valuable knowledge and experience. He was always patient with me and never hesitated about sharing his precious time during my thesis study. I was so lucky to have the chance to be guided by such a wise and modest person.

I am thankful to ROKETSAN A.S. and I would like to mention that, I am proud to be a member of the CFD group which I am currently working with. I want to thank to Dr. Güzide Özen for sharing her experience on reactive fluid flow problems; Dr. Bora Kalpaklı for his ideas and suggestions on numerical methods; Özgür Harputlu, Ali Yıldırım, Hasan Akın and Ozan Köken for long and beneficial discussions on the physics of fluids and Özge Şen for sharing related chemistry data and information. Accordingly, I have to pay my respects to Dr. Mine Yumuşak and Emir Bediğ Acar for their encouragements and Mustafa Akdemir for his patience on my endless questions.

I want to express my gratitude to Uğur Arkun for his supports on this thesis study.

Special thanks to TÜBİTAK for giving me the chance to work in the project with the number 112M129 and partially funding this study.

I would also thank to Tuba Bucak Onay for never giving up on me. She worked hard to bliss me up during my most anxious times. I also want to mention that, she has always been a hero and an inspirational brain working for the conservation of our nature and the future of this beautiful country. Knowing her for more than the half of my life was the biggest chance for me.

Finally, my last sentences are for my daughter. Thank you for reading together with me on my breaks. I hope we will have more time from now on. We can continue...

“Three cats on the roof: Piti, Pati and Pus are lying on their backs, watching the night sky... (Three cats, One wish - Sara Şahinkanat)”

TABLE OF CONTENTS

ABSTRACT	v
ÖZ	vii
ACKNOWLEDGEMENTS	x
TABLE OF CONTENTS	xi
LIST OF TABLES	xiv
LIST OF FIGURES	xv
LIST OF ABBREVIATIONS	xx
LIST OF SYMBOLS	xxi
CHAPTERS	
1. INTRODUCTION	1
1.1. Motivation	1
1.2. Scope of the Thesis Study	5
2. MODELING APPROACH.....	9
2.1. Aerothermodynamics Analysis	9
2.1.1. Discretization of Flow Equations	11
2.1.2. Convective Flux Calculation	12
2.1.3. Viscous Flux Calculation.....	14
2.1.4. Turbulence Closure.....	16
2.1.4.1. Baldwin-Lomax Turbulence Model	16
2.1.4.2. Baldwin-Barth (k - R_T) Turbulence Model	18
2.1.4.3. Spalart-Allmaras Turbulence Model.....	19
2.1.5. Thermodynamic Model.....	20

2.1.6. Flow Thermochemistry Calculation Method	21
2.1.7. Calculation of Mixture Viscosity and Species Diffusion Terms.....	24
2.2. Ablation Modeling	26
2.2.1. In-depth Energy Analysis	26
2.2.2. Surface Thermochemistry Analysis	26
2.2.2.1. Graphite in Air	26
2.2.2.2. Graphite in SRM.....	28
2.2.3. Ablation Boundary Condition	31
2.2.3.1. Boundary Condition for Decoupled Analysis.....	31
2.2.3.2. Boundary Condition for Coupled Analysis	35
3. VALIDATION AND VERIFICATION OF SUBMODELS	37
3.1. Solid Conduction Model	37
3.1.1. Stefan (Melting) Problem	37
3.1.2. 1-D Ablation Problem with Known Recession Velocity	40
3.1.3. 2-D Conduction Problem.....	41
3.2. Surface Thermochemistry Model.....	44
3.3. Flow Thermochemistry Model.....	47
3.4. Aerothermodynamics Model.....	52
4. GRAPHITE IN AIR ABLATION MODELING RESULTS	57
4.1. Problem Definition and Grid Convergence Study	57
4.2. Ablation Analysis Results	62
4.3. Ablation Analysis of a Drag Optimized Nose-Tip Geometry.....	67
4.4. Discussions on External Flow Solution Results	73
5. EROSION MODELING RESULTS FOR SRM NOZZLE THROATS	75

5.1. Comparison of Equilibrium and Finite Rate Models using Decoupled Analysis	75
5.2. Time Accuracy Check for the Decoupled Model.....	80
5.3. Coupled Analysis Results.....	85
5.4. Discussions on Internal Flow Solution Results	100
6. CONCLUSION AND FUTURE WORK	103
6.1. Conclusion.....	103
6.2. Future Work	105
REFERENCES.....	107
CURRICULUM VITAE	119

LIST OF TABLES

TABLES

Table 2.1. An Example Interpolation Table for Graphite Ablation ($T=2800$ K)	30
Table 3.1. Different initialization cases for single point solution of B'	47
Table 3.2. Initial Species Mass Fractions [20] – Air Reactions	50
Table 3.3. Initial Species Mass Fractions [56] – SRM Nozzle Reactions	50
Table 3.4. Free Stream Conditions of Lobb’s Experiment [57]	53
Table 4.1. Free Stream Conditions of Arc-Jet Test [20,22,23].....	57
Table 5.1. Nozzle Inlet Conditions of the Test Cases [46]	75
Table 5.2. Computed Temperature and Erosion Rate Values on the Throat	78
Table 5.3. Nozzle Inlet Conditions of the Test Case (Nonmetallized Propellant) [7, 60]	85
Table 5.4. Comparison of Calculated Erosion Rates on the Throat	91
Table 5.5. Nozzle Inlet Conditions of the Test Case (Metallized Propellant) [7, 60]	96

LIST OF FIGURES

FIGURES

Figure 1.1. Energy Transfer Mechanism on Ablating Wall.....	2
Figure 1.2. Flow Charts of (a) Decoupled (b) Coupled Analysis Tools	6
Figure 2.1. Wave and State Structure of HLLC Solver (adapted from [29]).....	13
Figure 2.2. Computation of Derivative Terms on the Cell Edges.....	16
Figure 2.3. Variation of Species Mass Fractions with Wall Temperature (30 Bar)...	30
Figure 3.1. Variation of Temperature Distribution inside the Teflon Ablator.....	39
Figure 3.2. Comparison of the Calculated Recession with the Reference Study [48]	39
Figure 3.3. Comparison of Calculated Temperature Distributions with the Analytical Solution	40
Figure 3.4. Description and the Boundary Conditions of the Validation Problem	41
Figure 3.5. 52x52 Structured Grid (intentionally skewed)	42
Figure 3.6. Calculated Temperature Distributions $\tau = 0.2, 0.4, 0.6$ and 0.8	43
Figure 3.7. Comparison of Numerical and Analytical Results	44
Figure 3.8. Comparison of blowing rate parameters at 101325 Pa with Computational Results from References [50, 52, 53].....	46
Figure 3.9. Partial pressures of species on ablating wall at 101325 Pa boundary layer edge pressure.....	46
Figure 3.10. Converged Species Mass Fraction Results of Marching Solution with 17 Reactions and Comparison with CEA Equilibrium Results (1500 Pa).....	48
Figure 3.11. Converged Species Mass Fraction Results of Marching Solution with 49 Reactions and Comparison with CEA Equilibrium Results (1500 Pa).....	49
Figure 3.12. Variation of Species Mass Fractions with Time ($T=12000$ K, $p = 1500$ Pa)	50

Figure 3.13. Converged Species Mass Fraction Results of Marching Solution with SRM Nozzle Reactions and Comparison with CEA Equilibrium Results (50 Bar) ..	51
Figure 3.14. Variation of Species Mass Fractions with Time (T=1000 K, p = 50 Bar)	52
Figure 3.15. Grid Convergence Study and Comparison of Shock Standoff Distances	53
Figure 3.16. Distributions of Mach number, Pressure, Temperature and Density	54
Figure 3.17. Comparison of Temperature Distributions for Viscid and Inviscid Solutions	55
Figure 4.1. Residual Histories for Grid Convergence Study	59
Figure 4.2. Grid Convergence Study - Variation Along (a) Stagnation Line (b) Nose-tip Surface	60
Figure 4.3. Numerical Results Using 96x52 Grid	61
Figure 4.4. Residual Histories inside the Flow Field (Coupled Analysis)	63
Figure 4.5. Residual Histories of Mass Blowing Rate and Wall Temperature on the Stagnation Point (Coupled Analysis).....	63
Figure 4.6. Comparison of Calculated Wall Temperature Distributions with References [20, 23].....	63
Figure 4.7. Temperature Distributions inside the Solid Domain.....	64
Figure 4.8. Comparison of Calculated Mass Blowing Rate Distributions with References [20, 22, 23].....	65
Figure 4.9. Temperature Distributions inside the Flow Field.....	65
Figure 4.10. Mass Fraction Distributions of C ₃ and CO inside the Flow Field (Coupled Analysis).....	66
Figure 4.11. Mass Fraction Distributions along the Stagnation Line (Coupled Analysis).....	67
Figure 4.12. Nose-Tip Geometries	68
Figure 4.13. Numerical Results Using 96x52 Grid - Nose-Tip B (Adiabatic Wall) .	69
Figure 4.14. Comparison of Mass Blowing Rate and Wall Temperature Distributions - (a) Decoupled Analysis (b) Coupled Analysis	70

Figure 4.15. Mass Fraction Distributions of C_3 and CO inside the Flow Field - Nose-Tip B (Coupled Analysis)	70
Figure 4.16. Temperature and Pressure Contours Around the Nose-tips A and B	71
Figure 4.17. Comparison of Ablation Analysis Results (Solid Black Lines: Nose-Tip A Results, Solid Red Lines: Nose-Tip B Results, Solid Grey lines: Geometry of Nose-Tip A, Dashed Grey Lines: Geometry of Nose-Tip B).....	72
Figure 4.18. Comparison of Temperature Distributions inside the Solid Domains...	73
Figure 5.1. Numerical Results for 15 % Aluminized Propellant (Adiabatic Wall, Frozen Flow)	76
Figure 5.2. Comparison of Computed Erosion Rate Values with Experiment from [46] (Decoupled Analysis).....	77
Figure 5.3. Variation of Erosion Rate with Time (Finite Rate, Decoupled Analysis)	78
Figure 5.4. Variation of Total Recession with Time (Finite Rate, Decoupled Analysis)	79
Figure 5.5. Temperature Contours inside the Solid Domain at $t = 1, 5$ and 10 s for 15 % Aluminized Propellant (Finite Rate Surface Thermochemistry, Decoupled Analysis)	80
Figure 5.6. View of the Simplified Model of the Test Motor	81
Figure 5.7. Variation of Temperature Contours with Time	82
Figure 5.8. Variation of Wall Temperature with Time	83
Figure 5.9. Variation of Recession Rate with Time.....	83
Figure 5.10. Variation of Total Recession with Time and Comparison with Measurement.....	83
Figure 5.11. Distributions of Energy Transferred to the Solid - Reactive and Nonreactive Walls.....	84
Figure 5.12. Comparison of Wall Temperature Distributions for Reactive and Nonreactive Walls.....	84

Figure 5.13. Temperature Contours inside the Solid Domain at $t = 1.5$ and 3 s for Nonmetallized Propellant (Finite Rate Surface Thermochemistry, Decoupled Analysis).....	86
Figure 5.14. Numerical Results Nonmetallized Propellant (Adiabatic Wall, Frozen Flow).....	87
Figure 5.15. Comparison of Calculated Erosion Rate Distributions using Coupled and Decoupled Analyses (Frozen Flow, Spalart-Allmaras Turbulence Model, Nonmetallized Propellant).....	88
Figure 5.16. Comparison of Calculated Wall Temperature Distributions using Coupled and Decoupled Analysis (Frozen Flow, Spalart-Allmaras Turbulence Model, Nonmetallized Propellant).....	89
Figure 5.17. Contours of Turbulent Viscosity Ratio (Frozen Flow, Spalart-Allmaras Turbulence Model, Nonmetallized Propellant)	89
Figure 5.18. Contours of Temperature and H_2 , CO and H_2O Mass Fractions near the Throat (Frozen Flow, Spalart-Allmaras Turbulence Model, Nonmetallized Propellant)	90
Figure 5.19. Turbulent Viscosity Distributions inside the Boundary Layer (Diverging Section, 0.03 m of Axial Distance from the Throat)	92
Figure 5.20. Turbulent Viscosity Contours for Spalart-Allmaras and Baldwin-Barth Turbulence Models	92
Figure 5.21. Comparison of Calculated Erosion Rate Distributions using Different Turbulence Models (Frozen Flow, Nonmetallized Propellant)	93
Figure 5.22. Comparison of Calculated Wall Temperature Distributions using Different Turbulence Models (Frozen Flow, Nonmetalized Propellant).....	93
Figure 5.23. Variation of Erosion Rate Distribution with the Closure Coefficient c_{b1}	94
Figure 5.24. Variation of Wall Temperature Distribution with the Closure Coefficient c_{b1}	94
Figure 5.25. Diffusive Behavior of HLL Method for Shear Flow Parallel to the Ablating Wall.....	95

Figure 5.26. Comparison of Calculated Erosion Rate Distributions for Frozen and Reactive Flows (Spalart-Allmaras Turbulence Model, Metallized Propellant).....	97
Figure 5.27. Comparison of Calculated Wall Temperature Distributions for Frozen and Reactive Flows (Spalart-Allmaras Turbulence Model, Metallized Propellant) ..	97
Figure 5.28. Comparison of Species Mass Fractions for Frozen and Reactive Flows (Spalart-Allmaras Turbulence Model, Metallized Propellant).....	98
Figure 5.29. Temperature Contours inside the Fluid and Solid Domains (Frozen Flow, Spalart-Allmaras Turbulence Model, Metallized Propellant, Steady State Analysis)	99

LIST OF ABBREVIATIONS

ABBREVIATIONS

- 1-D : 1 Dimensional
- 2-D : 2 Dimensional
- C/C : Carbon/Carbon Composite
- CFD : Computational Fluid Dynamics
- HLL : Harten, Lax and van Leer
- HLLC : Harten, Lax and van Leer - Contact
- SRM : Solid Rocket Motor

LIST OF SYMBOLS

SYMBOLS

A	: Area vector (m)
A_f	: Pre-exponential or frequency factor ($\text{m}^3/\text{mol.s}$ or $\text{m}^6/\text{mol.s}$)
a	: Coefficient for equilibrium constant calculation and speed of sound (m/s)
b	: Coefficient for equilibrium constant calculation (K)
B'	: Dimensionless mass blowing rate
Bi	: Biot number
C_m	: Mass transfer coefficient
C_p	: Constant pressure specific heat capacity (J/kg.K)
C	: Generic flow variable and Mole fraction of gas species
D	: Diffusion coefficient (m^2/s)
e_t	: Total energy (J/kg)
E_f	: Activation Energy (J/mole)
F	: Convective flux vector in z direction
G	: Convective flux vector in r direction
F_v	: Viscous flux vector in z direction
G_v	: Viscous flux vector in r direction
h	: Enthalpy (J/kg)
H	: Convective axisymmetric source vector and molar enthalpy (J/mole)
H_v	: Viscous axisymmetric source vector
J	: Mass diffusion flux ($\text{kg}/\text{m}^2.\text{s}$) and grid transformation Jacobian (m^2)
k	: Conduction coefficient (W/m.K)
k_b	: Backward reaction rate ($\text{m}^3/\text{mol.s}$ or $\text{m}^6/\text{mol.s}$)
k_f	: Forward reaction rate ($\text{m}^3/\text{mol.s}$ or $\text{m}^6/\text{mol.s}$)
K_r	: Equilibrium constant of reaction
l_{mix}	: Mixing length (m)

Le	: Lewis number
\dot{m}	: Mass blowing rate (kg/m ² .s)
P	: Pressure (Pa)
Pr	: Prandtl number
q	: Heat flux (W/m ²)
r	: Radial coordinate (m)
R	: Universal gas constant (J/mol.K) and radius (m)
s	: Recession (m) and distance through streamwise direction (m)
S	: Molar entropy (J/mol.K) and wave speed (m/s)
\hat{S}	: Modified vorticity (1/s)
Sc	: Schmidt number
St	: Stanton number
\dot{s}	: Recession rate (mm/s)
t	: Time (s)
T	: Temperature (K)
u	: Velocity in z direction (m/s)
\hat{u}	: Roe averaged speed in normal direction to the cell edge (m/s)
v	: Velocity in r direction, Landau advection velocity (m/s) and stoichiometric coefficient
\dot{w}	: Species source term (kg/m ³ .s)
W	: Flow variable vector and vorticity (1/s)
x	: Coordinate in 1-D (m)
X	: Nondimensional coordinate in 1-D (m)
y	: Mass fraction of gas species
y^+	: Dimensionless vertical distance
z	: Axial coordinate (m)
α	: Thermal diffusivity (m ² /s)
β_f	: Temperature exponent
ε	: Surface emissivity

μ	: Dynamic viscosity (Pa.s)
ρ	: Density (kg/m ³)
τ	: Shear Stress (Pa) and Nondimensional time
θ	: Nondimensional temperature
ξ	: Nondimensional coordinate
η	: Nondimensional coordinate
Ω	: Magnitude of vorticity (1/s)
σ	: Stefan Boltzmann constant (W/m ² .K ⁴)
ν	: Kinematic viscosity (m ² /s)
ν_t	: Turbulent viscosity (m ² /s)
$\hat{\nu}$: Flow variable of Spalart-Allmaras turbulence model (m ² /s)

CHAPTER 1

INTRODUCTION

1.1. Motivation

Conjugate analyses of fluid flow and thermal response of solid domains which are exposed to external effects of flow fields are critical implementations of aerospace engineering design processes. Previously, absence of computer power motivated engineers to develop successful empirical approximations [1-3] in order to predict the thermal effects of aerodynamic heating on solid materials. These approximations were usually task specific and restricted with the geometries/materials under specific flow conditions. Besides, most of the thermal response problems are not limited to aerodynamic heating due to high temperature gas flows. Phenomena like melting, sublimation, spallation, mechanical erosion, accumulation or internal cracking are also likely to occur in specific engineering applications. The current study aims to develop effective analysis tools for thermal protection system (TPS) materials under reactive flow conditions including the effects of thermochemical erosion/ablation.

Ablative TPS's can be considered in two categories as non-charring and charring materials [4]. Non-charring materials usually erode only from the surface with phenomena like oxidation, melting, sublimation, evaporation or mechanical effects (e.g. Teflon, graphite). On the other hand, charring materials decomposes internally as well as eroding from the surface (e.g. Carbon-phenolic, Ethylene-Propylene-Diene Monomers). The increase of internal temperature with high heat fluxes from the fluid flow causes the production of pyrolysis gasses. These gasses are released to the boundary layer of the flow field.

Current study focuses on the ablation and thermal analysis of carbon based non-charring materials (e.g. graphite, Carbon/carbon composites). This type of materials

are frequently used for the nozzle inserts of Solid Rocket Motors (SRM). Besides, graphitic ablation models provide a basis for charring ablation models suitable for external hypersonic flow implementations. Ablation physics of commonly used TPS materials like phenolic based carbon ablators include the oxidation and sublimation of char residue which is produced with pyrolysis gas release from the material.

Energy transfer mechanisms on the ablating front of a non-charring material are given in Figure 1.1. Convective heating from the fluid side increases the wall temperature and the surface recession begins due to heterogeneous surface reactions. Ablation products are blown into the boundary layer. Injection of these products effects the species concentration distribution inside the boundary layer. Also, species concentration gradients result in the diffusion between the boundary layer and the ablating wall. Radiative heat transfer between the hot fluid gases and the surface is experienced. An energy balance relation which includes these phenomena should be satisfied for both aerothermodynamics and material response models. Besides, mass balance should also be considered on the ablating surface.

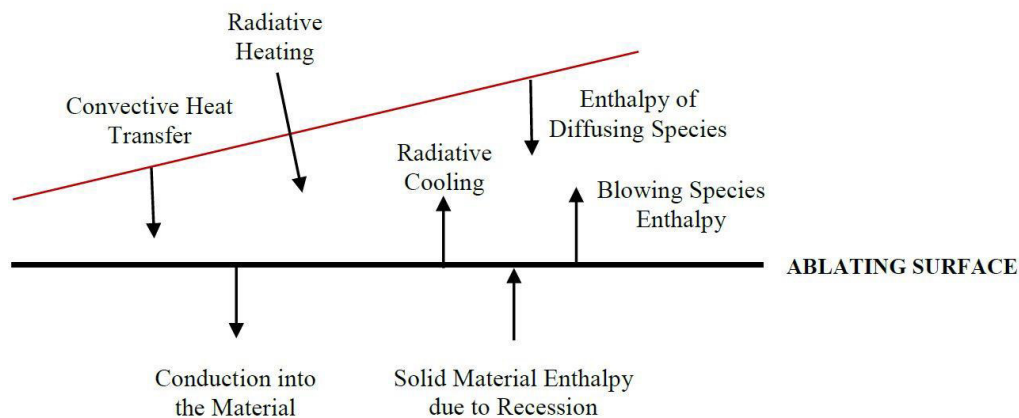


Figure 1.1. Energy Transfer Mechanism on Ablating Wall

Two critical implementation areas are selected for the modeling of the thermochemical response of graphitic surfaces. These are mainly ablation under hypersonic air flow conditions and erosion of nozzle throats inside the SRM's

Internal walls of SRM's are exposed to wild flow field environments. The high temperature shear flow over the wall results in high heat flux values and thermal stresses on the bodies of the motors. The usage of ablative TPS materials is a common application for the structural integrity. Although ablative materials cause the change of the internal contours of the designs, they are successful in terms of removing the high enthalpy from the body to be protected. Materials composed of pure carbon like graphite and Carbon/carbon composites are two widespread choices for the nozzle throats. The dominant reasons of the recession of these materials are the heterogeneous oxidation reactions with molecules like H_2O and CO_2 . Infinite reaction rate assumption is usually a reasonable approach for motors with high total temperature combustion chambers (i.e. aluminized propellants). In these cases, the recession rates are limited with the diffusion rates of the reactants and the equilibrium composition of wall species can be imposed to the surface. Oxidation can only proceed if the reactants can reach to the ablative wall with the diffusion phenomenon. On the other hand, reaction rates can be lower than or comparable with the diffusion rates for relatively low total temperature flows. These cases result in reaction rate controlled recession rates or mixed limitation of chemical kinetics and diffusion. Previously Kuo and Keswani [5] developed an aerothermochemical model for C/C composite nozzle throats. They have assumed a two-layer flow. These layers were mainly a viscous boundary layer and a 1-D inviscid core flow. Mixed limitation of the recession rates is implemented including first order finite rate oxidation reactions. Borie et al [6] also assumed a two-layer flow and included the both limitation effects on the recession rate calculations. They have used a laser beam test system in order to reveal the kinetic characteristics of C/C material and they have provided this information to their numerical model. In 2008, Thakre and Yang [7] have published the results of their coupled modeling study. They have used Favre-averaged flow equations and assumed

a 1-D steady state conduction with finite rate surface thermochemistry. Bianchi et al [8] also assumed 1-D in-depth conduction in their state of the art coupled study. They have initially validated their numerical results using wall equilibrium assumption and then extended their work to a finite rate surface thermochemistry model [9]. Coupled thermal response modeling studies on the nozzle throats and insulations are not limited to pure carbon materials. Turchi [10] has developed a steady state coupled analysis tool for charring carbon based and silica based materials. Cross and Boyd [11] also published their study on conjugate and multi-dimensional ablation analysis of charring materials in 2019. They have used LeMANS [12] and MOPAR-MD [13] codes for flow field and material response analyses, respectively.

Another implementation area of insulation with ablative TPS's is the atmospheric re-entry. In space missions, during re-entry, vehicles reach to hypersonic speeds and the noses of the vehicles face with highly energetic gasses. The temperature levels of the attacking gasses may reach to values of decomposition or even ionization of gas species [14]. Removal of the high temperature material with ablation acts as coolant on the vehicle surface and injected ablation products changes the thermal properties of the boundary layer. In 1993, Keenan has performed coupled analyses of hypersonic flow field and polycrystalline graphite ablation for re-entry missions [15]. In his study, thermal and chemical non-equilibrium effects are included in the simulations and the ablation of graphite material is limited with the heterogeneous oxidation reactions. Kuntz et al. have developed an iterative coupling procedure and performed simulation studies for graphite ablation under atmospheric re-entry conditions [16]. The numerical tools SACCARA [17] and COYOTE II [18] are used for flow field and material response calculations. Surface equilibrium tables which are prepared using ACE [19] program have been used in their study. In 2004, the ablation rate measurement results of the arc-jet tests which are performed in NASA Ames Research center [20] are used for the comparisons with the computational results of the GIANTS code [21] coupled with ablation boundary conditions [22]. In this numerical study, Chen and Milos compared the accuracies of two different finite rate surface reaction

models with the surface equilibrium assumption [22]. Bianchi et al. [23] integrated a full Navier-Stokes solver with a 1-D conduction model and used equilibrium assumption on the ablating graphite surface. They have validated the calculated mass blowing rate results with similar experiment data which are used by Chen and Milos [20]. Another coupled model have been developed by Martin and Boyd [24] using LeMANS [12] and MOPAR [25] codes. Graphite ablation simulation results have been verified using trajectory points of IRV-2 vehicle [16]. Effects of the movement of the ablating front are also included in their modeling study using the algorithm offered by Zhang et al [26].

During the design processes, the accurate prediction of the total material removal due to ablation is an important requirement in order to reduce the usage of total insulation mass. Besides, foreknowledge of heat flux to the wall and the temperature distribution inside the materials is critical in terms of satisfying the structural limits of the designs. Development of an accurate and consistent ablation and thermal analysis tool is a beneficial strategy for reducing the number of expensive tests and design iterations.

1.2. Scope of the Thesis Study

In this thesis study, two different analysis tools are developed for graphitic ablation for internal flow conditions inside SRM nozzles and external flow conditions around hypersonic nose-tips. Initially, a decoupled method is used for modeling purposes. The boundary layer edge properties which are extracted from the flow field solution results are used as the boundary condition of ablation analysis. In this method, it is assumed that the flow field is not affected by the ablation phenomenon. In the decoupled analysis, accurate resolution of momentum and thermal boundary layer profiles is not a strict requirement since well-defined heat transfer coefficient approximations are selected from the literature [2, 3]. On the other hand, these approximations are developed for certain geometries and flow conditions (e. g. blunt nose-tips for hypersonic flows) as previously stated. Thus, a strongly coupled modeling strategy is developed in order to avoid geometric restrictions in the analyses.

Aerothermodynamics analysis and thermal response calculation tools are integrated via sharing the information on the eroding wall. Ablation products are injected inside the flow field. The calculations are carried on until the ablation boundary condition and convergence of solution is satisfied for both fluid and solid sides. Flow charts of decoupled and coupled analyses are given in Figure 1.2

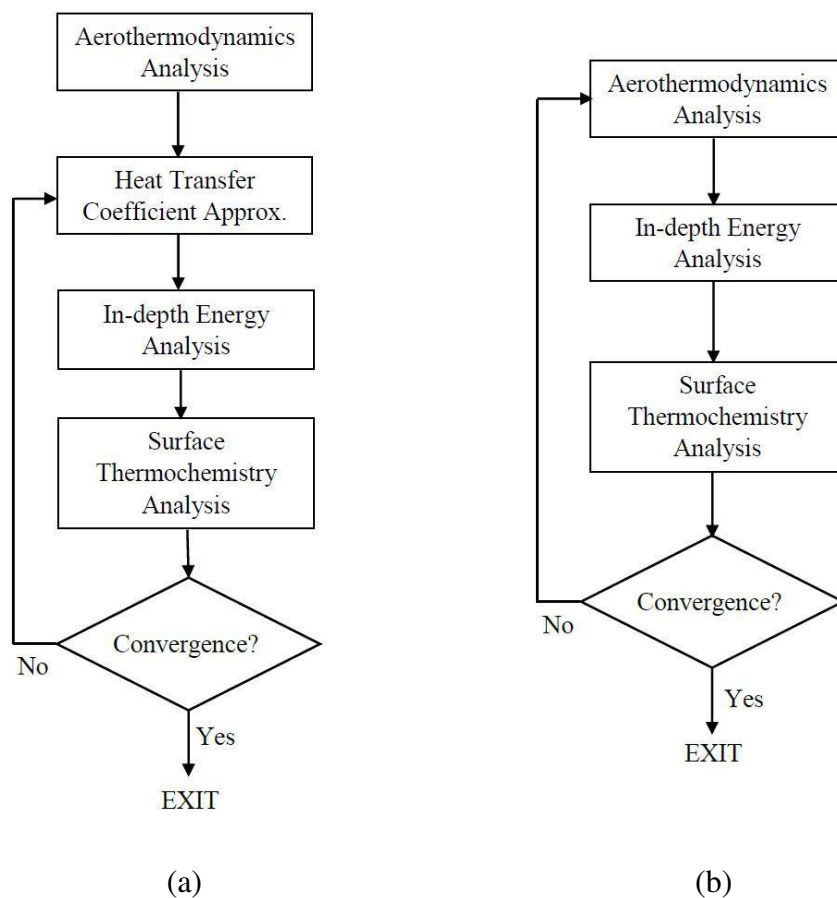


Figure 1.2. Flow Charts of (a) Decoupled (b) Coupled Analysis Tools

In surface thermochemistry calculations, usage of interpolation tables is a common approach for graphite-in-air ablation problem [27]. These tables are usually prepared

before the analysis and helpful for species concentration calculations on the ablating wall. In this study, the usage of interpolation tables is not preferred for graphite in air problems. An equilibrium surface thermochemistry analysis model is developed and included in the coupling of solid and fluid domain solutions. The aim of this implementation is to avoid the interpolation errors and to reduce the time required for preprocess of analysis studies. Equilibrium assumption is usually valid for steady-state ablation of graphite in air problem since the temperature behind the shock is relatively high in hypersonic flow conditions. On the other hand, this assumption may not be valid for SRM nozzles especially for non-aluminized propellant combustion chambers with low total temperature values. Thus, both equilibrium and finite rate thermochemistry approaches are implemented and the results of these methods have been compared for SRM nozzle applications.

A structured and multi-species finite volume model is developed for flow field analysis. Domain is assumed to be axisymmetric. Godunov type flux calculation methods HLL [28] and HLLC [29] are used for the evaluation of convective fluxes and explicit local time stepping is used for convergence. A linear system solver is developed in order to handle the finite rate reaction equations. Three different turbulence models have been included which are mainly algebraic Baldwin-Lomax [30], one equation Baldwin-Barth [31] and one equation Spalart-Allmaras [32] models. Also, an axisymmetric heat conduction code is developed for materials with variable thermal properties. Conduction coefficients of C/C materials usually change with the direction as well as the temperature. Thus, possible anisotropy of the materials has also been considered in the current study.

CHAPTER 2

MODELING APPROACH

2.1. Aerothermodynamics Analysis

An in-house axisymmetric Navier-Stokes solver is developed for flow field analyses. Flow equations are used in conservative variable form and a density based approach is used. The generalized form of the equations is given below in equation (2.1). The equations include convective and viscous flux terms; convective and viscous axisymmetric source terms and chemical source terms.

$$\frac{\partial W}{\partial t} + \frac{\partial F(W)}{\partial z} + \frac{\partial G(W)}{\partial r} - \frac{\partial F_v(W)}{\partial z} - \frac{\partial G_v(W)}{\partial r} + H + H_v - S = 0 \quad (2.1)$$

Below in equation (2.2) conservative variable vector and convective flux vectors are shown. The terms of the vectors belong to continuity, z and r momentum, energy and species continuity equations. A Godunov type approximate Riemann method is used for the evaluation of the convective fluxes.

$$W = \begin{bmatrix} \rho \\ \rho u \\ \rho v \\ \rho e_t \\ \rho_1 \\ \vdots \\ \rho_{k-1} \end{bmatrix} \quad F = \begin{bmatrix} \rho u \\ \rho u u + p \\ \rho u v \\ (\rho e_t + p)u \\ \rho_1 u \\ \vdots \\ \rho_{k-1} u \end{bmatrix} \quad G = \begin{bmatrix} \rho v \\ \rho u v \\ \rho v v + p \\ (\rho e_t + p)v \\ \rho_1 v \\ \vdots \\ \rho_{k-1} v \end{bmatrix} \quad (2.2)$$

In equation (2.3), viscous flux vectors are given in axial and radial coordinates. Diffusion flux terms due to species mass fraction gradients inside the flow field are also included. These gradients are generated inside the flow field due to gas phase reactions and heterogeneous surface reactions. Accurate modeling of diffusion terms is critical in terms of blowing rate estimations since they are effective on both energy

and mass balance of an ablating surface. Convective and viscous axisymmetric source term and species source term vectors are given below in equation (2.4). The usage of axisymmetric source terms is helpful in terms of defining a simple switch for a 2-D flow solver.

$$\hat{F}_v = \begin{bmatrix} 0 \\ \tau_{zz} \\ \tau_{zr} \\ \tau_{zz}u + \tau_{zr}v + q_z + \sum J_{z,i}h_i \\ J_{z,1} \\ \vdots \\ J_{z,N-1} \end{bmatrix} \quad \hat{G}_v = \begin{bmatrix} 0 \\ \tau_{zr} \\ \tau_{rr} \\ \tau_{zr}u + \tau_{rr}v + q_r + \sum J_{r,i}h_i \\ J_{r,1} \\ \vdots \\ J_{r,N-1} \end{bmatrix} \quad (2.3)$$

$$H = 1/r \begin{bmatrix} \rho v \\ \rho uv \\ \rho v^2 \\ (\rho e_t + p)v \\ \rho_1 v \\ \vdots \\ \rho_{k-1} v \end{bmatrix} \quad H_v = 1/r \begin{bmatrix} 0 \\ \tau_{zr} \\ \tau_{rr} + \tau_{\theta\theta} \\ u\tau_{zr} + v\tau_{rr} + q_r \\ 0 \\ \vdots \\ 0 \end{bmatrix} \quad S = \begin{bmatrix} 0 \\ 0 \\ 0 \\ 0 \\ \dot{w}_1 \\ \vdots \\ \dot{w}_{k-1} \end{bmatrix} \quad (2.4)$$

Total energy is defined as shown in equation (2.5) and the shear stress terms are evaluated using Stokes hypothesis as in equation (2.6). Conduction coefficients are calculated assuming that the Prandtl number is equal to 0.72 and 0.9 for laminar and turbulent flows, respectively.

$$e_t = h - \frac{p}{\rho} + 0.5(u^2 + v^2) \quad (2.5)$$

$$\begin{aligned} \tau_{zz} &= \mu \left(\frac{4}{3} \frac{\partial u}{\partial z} - \frac{2}{3} \frac{\partial v}{\partial r} \right), & \tau_{zr} &= \mu \left(\frac{\partial u}{\partial r} + \frac{\partial v}{\partial z} \right) \\ \tau_{rr} &= \mu \left(\frac{4}{3} \frac{\partial v}{\partial r} - \frac{2}{3} \frac{\partial u}{\partial z} \right), & \tau_{\theta\theta} &= -\frac{2}{3} \mu \left(\frac{\partial u}{\partial z} + \frac{\partial v}{\partial r} \right) + \frac{4}{3} \mu \frac{v}{r} \end{aligned} \quad (2.6)$$

Fourier's rule is implemented for the calculation of heat flux terms. The temperature derivatives are evaluated on the cell edges such as all other gradients included in this modeling study.

$$k = \frac{\mu C_p}{Pr} \quad (2.7)$$

$$q_z = -k \frac{\partial T}{\partial z} \quad q_r = -k \frac{\partial T}{\partial r} \quad (2.8)$$

2.1.1. Discretization of Flow Equations

For flow field analyses, finite volume approach is used and the equations are integrated over the control volumes as shown below in equation (2.9).

$$\frac{\partial W}{\partial t} = -\frac{1}{V} \left[\oint_{\partial V} [(F - F_v)i + (G - G_v)j] \cdot dA - \int_V (H + H_v - S) dV \right] \quad (2.9)$$

Explicit Euler integration is implemented with local time stepping for the temporal discretization. The discrete form of the equations is adapted from Blazek [33] and modified for axisymmetric flow fields with structured grids. In equation (2.10), ΔA_m and \vec{n}_m are the area and the unit normal vector of the m^{th} cell edge, respectively.

$$\begin{aligned} \frac{W^{n+1} - W^n}{\Delta t} = & -\frac{1}{V} \left[\sum_{m=1}^4 [(F - F_v)_m i + (G - G_v)_m j] \cdot \vec{n}_m \Delta A_m \right. \\ & \left. - (H + H_v - S)V \right] \end{aligned} \quad (2.10)$$

Local time steps are decided with Courant-Frederichs-Lewy (CFL) condition as given in equation (2.11).

$$\Delta t = \frac{CFL \cdot V}{A_z(|u| + a) + A_r(|v| + a)} \quad (2.11)$$

where a is the speed of sound and A_z and A_r are the projected areas of the cell on the axial and radial axes, respectively.

2.1.2. Convective Flux Calculation

In the aerothermodynamics analysis, HLL (Harten, Lax and van Leer) [28] and HLLC (Harten, Lax and van Leer - Contact) [29] methods are implemented for the evaluation of Godunov fluxes. HLLC is an approximate Riemann solver which is based on HLL method. Cell fluxes on the edges are calculated as follows with HLL solver.

$$\hat{F}_e^{HLL} = \begin{cases} F_{e,0} & \text{if } 0 \leq S_{e,0} \\ \frac{S_{e,1}F_{e,0} - S_{e,0}F_{e,1} + S_{e,0}S_{e,1}(W_{e,1} - W_{e,0})}{S_{e,1} - S_{e,0}} & \text{if } S_{e,0} \leq 0 \leq S_{e,1} \\ F_{e,1} & \text{if } 0 \geq S_{e,1} \end{cases} \quad (2.12)$$

where $S_{e,0}$ and $S_{e,1}$ are left and right running waves and $W_{e,0}$ and $W_{e,1}$ are left and right state variables, respectively. The HLL method separates the states with two waves and this approach has tendency to result in diffusive distributions of flow variables in shear flows. On the other hand, missing intermediate wave is included in the HLLC approach for more accurate calculations. The wave structure and the state variables for the direct calculation of the flux terms are shown below in Figure 2.1. Inclusion of the middle wave results in two intermediate states for Riemann problem solution.

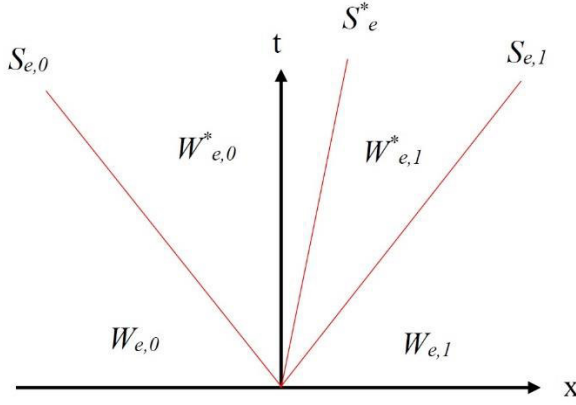


Figure 2.1. Wave and State Structure of HLLC Solver (adapted from [29])

The fluxes on the edges of finite volume cells are calculated as given below in equation (2.13).

$$\hat{F}_e^{HLLC} = \begin{cases} F_{e,0} & \text{if } 0 \leq S_{e,0} \\ F_{e,0}^* = F_{e,0} + S_{e,0}(W_{e,0}^* - W_{e,0}) & \text{if } S_{e,0} \leq 0 \leq S_e^* \\ F_{e,1}^* = F_{e,1} + S_{e,1}(W_{e,1}^* - W_{e,1}) & \text{if } S_e^* \leq 0 \leq S_{e,1} \\ F_{e,1} & \text{if } 0 \geq S_{e,1} \end{cases} \quad (2.13)$$

The intermediate states are evaluated with the relations below where S_e^* is the middle wave speed. The subscript m stands for 0 and 1 for left and right variables, respectively. The state variables for the species continuity equations are also included to equation (2.14) since the flux calculation approach is used for a multispecies and reactive flow solver.

$$W_{e,m}^* = \rho_m \left(\frac{S_{e,m} - u_m}{S_{e,m} - S_e^*} \right) \begin{bmatrix} 1 \\ S_e^* \\ v_m \\ e_{t,m} + (S_e^* - u_m) \left(S_e^* + \frac{p_m}{\rho_m(S_{e,m} - u_m)} \right) \\ \rho_{1,m}/\rho_m \\ \vdots \\ \rho_{k-1,m}/\rho_m \end{bmatrix} \quad (2.14)$$

S_e^* is calculated using left and right running wave speeds.

$$S_e^* = \frac{p_{e,1} - p_{e,0} + \rho_{e,0}u_{e,0}(S_{e,0} - u_{e,0}) - \rho_{e,1}u_{e,1}(S_{e,1} - u_{e,1})}{\rho_{e,0}(S_{e,0} - u_{e,0}) - \rho_{e,1}(S_{e,1} - u_{e,1})} \quad (2.15)$$

Direct calculation approach proposed by Davis [34] can be used for the wave speeds as follows.

$$\hat{S}_{e,0} = \hat{u} - d, \quad \hat{S}_{e,1} = \hat{u} + d \quad (2.16)$$

$$d^2 = \frac{\sqrt{\rho_{e,0}}a_{e,0}^2 + \sqrt{\rho_{e,1}}a_{e,1}^2}{\sqrt{\rho_{e,0}} + \sqrt{\rho_{e,1}}} + \frac{1}{2} \frac{\sqrt{\rho_{e,0}}\sqrt{\rho_{e,1}}}{(\sqrt{\rho_{e,0}} + \sqrt{\rho_{e,1}})^2} \quad (2.17)$$

where \hat{u} stands for Roe averaged speed normal to the edge of the finite volume cell and can be computed using equation (2.18).

$$\hat{u} = \frac{\sqrt{\rho_{e,0}}u_{e,0} + \sqrt{\rho_{e,1}}u_{e,1}}{\sqrt{\rho_{e,0}} + \sqrt{\rho_{e,1}}} \quad (2.18)$$

2.1.3. Viscous Flux Calculation

Using the advantage of structured grids, the flow variable gradient terms of viscous fluxes are calculated with the grid transformation metrics. Assuming that all the cell edges of the computational domain are unity in length, the differential relations between computational and physical coordinates can be written as follows [35]:

$$\begin{bmatrix} d\xi \\ d\eta \end{bmatrix} = \begin{bmatrix} \xi_z & \xi_r \\ \eta_z & \eta_r \end{bmatrix} \begin{bmatrix} dz \\ dr \end{bmatrix} \quad (2.19)$$

$$\begin{bmatrix} dz \\ dr \end{bmatrix} = \begin{bmatrix} z_\xi & z_\eta \\ r_\xi & r_\eta \end{bmatrix} \begin{bmatrix} d\xi \\ d\eta \end{bmatrix} \quad (2.20)$$

Using the relations (2.19) and (2.20), the derivatives of the coordinates of two different domains with respect to each other can be written as given below. The Jacobian term J is the ratio of areas in physical domain and computational domain. Thus, it is equal to physical area since all the edge lengths of the finite volume cells are set to unity in the computational domain.

$$\begin{bmatrix} \xi_z & \xi_r \\ \eta_z & \eta_r \end{bmatrix} = \begin{bmatrix} z_\xi & z_\eta \\ r_\xi & r_\eta \end{bmatrix}^{-1} \quad (2.21)$$

where

$$\begin{aligned} \xi_z &= Jr_\eta \\ \xi_r &= -Jz_\eta \\ \eta_z &= -Jr_\xi \\ \eta_r &= Jz_\xi \\ J &= \frac{1}{z_\xi r_\eta - r_\xi z_\eta} \end{aligned} \quad (2.22)$$

Assuming C is one of the flow variables, chain rule can be applied for the evaluation of derivatives using the grid transformation metrics.

$$\frac{\partial C}{\partial z} = \xi_z \frac{\partial C}{\partial \xi} + \eta_z \frac{\partial C}{\partial \eta} \quad (2.23)$$

$$\frac{\partial C}{\partial r} = \xi_r \frac{\partial C}{\partial \xi} + \eta_r \frac{\partial C}{\partial \eta} \quad (2.24)$$

Flow variable derivatives are calculated on the cell edges using virtual control volumes as shown in Figure 2.2. Gradient terms are not reconstructed but directly evaluated on the cell edges in order to avoid odd-even decoupling problem [33].

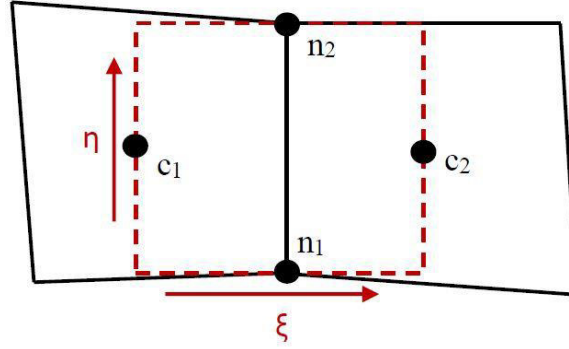


Figure 2.2. Computation of Derivative Terms on the Cell Edges

2.1.4. Turbulence Closure

2.1.4.1. Baldwin-Lomax Turbulence Model

Baldwin-Lomax [30] is a zero equation algebraic turbulence model and assumes a two layer flow for the computation of the turbulent viscosity. The inner layer viscosity is calculated as given in relation (2.25).

$$\nu_{ti} = (l_{mix})^2 |\Omega| \quad (2.25)$$

where Ω is the magnitude of the vorticity. The derivatives of the velocity components are computed using the grid transformation metrics as explained in section 2.1.2.

$$\Omega = \sqrt{2W_{ij}W_{ij}} \quad (2.26)$$

$$W_{ij} = \frac{1}{2} \left(\frac{\partial u_i}{\partial x_j} - \frac{\partial u_j}{\partial x_i} \right) \quad (2.27)$$

The mixing length can be evaluated using Van-Driest formulation (2.28). κ and A_0^+ are the model constants and y is the closest normal distance from the wall.

$$l_{mix} = \kappa y \left[1 - \exp \left(-\frac{y^+}{A_0^+} \right) \right] \quad (2.28)$$

Dimensionless distance y^+ is obtained using the wall shear stress value.

$$\begin{aligned} y^+ &= \frac{yu_*}{\nu} \\ u_* &= \sqrt{\frac{\tau_w}{\rho}} \end{aligned} \quad (2.29)$$

The outer layer turbulent viscosity is defined as given in equation (2.30). F_{kleb} is the Klebanoff's intermittency function. The inner and outer layers of the boundary layer are separated with the point of the maximum value of the turbulent viscosity and where $\nu_{ti} = \nu_{to}$.

$$\nu_{to} = \rho \alpha C_{cp} F_{wake} F_{kleb} \left(y, \frac{y_{max}}{C_{kleb}} \right) \quad (2.30)$$

$$F_{kleb}(y, \delta) = \left[1 + 5.5 \left(\frac{y}{\delta} \right)^6 \right]^{-1} \quad (2.31)$$

Wake function can be computed as shown in equation (2.32). y_{max} is the normal distance between the wall and the point where the mixing length is maximum inside the boundary layer.

$$F_{wake} = \min \left[y_{max} F_{max}, \frac{C_{wk} y_{max} U_{dif}^2}{F_{max}} \right] \quad (2.32)$$

$$F_{max} = \frac{1}{\kappa} \left[\max_y (l_{mix} |\Omega|) \right] \quad (2.33)$$

The closure constants of the model are as given below.

$$\begin{aligned}
\kappa &= 0.4 & \alpha &= 0.0168 & A_0^+ &= 26 \\
C_{cp} &= 1.6 & C_{kleb} &= 0.3 & C_{wk} &= 1
\end{aligned}
\tag{2.34}$$

2.1.4.2. Baldwin-Barth (k-R_T) Turbulence Model

One of the turbulence closure approaches tested in this study is the Baldwin-Barth [31] model. This model is derived from the well-known two equation k- ϵ model and considers the turbulent Reynolds number as the field property. k-R_T is a self-consistent model and there is no requirement for algebraic length scale calculation. Flow variable R_T can be defined as follows:

$$R_T = \frac{k^2}{v\epsilon} \tag{2.35}$$

The model equation for wall bounded flows is given below.

$$\begin{aligned}
\frac{D(vR_T)}{Dt} &= (c_{\epsilon 2}f_2 - c_{\epsilon 1})\sqrt{vR_T P} + \left(v + \frac{v_t}{\sigma_\epsilon}\right)\nabla^2(vR_T) \\
&\quad - \frac{1}{\sigma_\epsilon}(\nabla v_t) \cdot \nabla(vR_T)
\end{aligned}
\tag{2.36}$$

The equation is integrated over control volumes and the advective terms are computed using first order upwinding. The production term is evaluated as shown in equation (2.37).

$$P = \left(\frac{\partial u_i}{\partial x_j} + \frac{\partial u_j}{\partial x_i}\right)\frac{\partial u_i}{\partial x_j} - \frac{2}{3}v_t\left(\frac{\partial u_k}{\partial x_k}\right)^2 \tag{2.37}$$

R_T is set to 0 and 0.5 on the walls and inflow boundaries, respectively. The domain is initialized with the inflow value. The following functions and constants are used for the closure of the turbulence model equation:

$$\begin{aligned}
\frac{1}{\sigma_\varepsilon} &= (c_{\varepsilon 2} - c_{\varepsilon 1}) \frac{\sqrt{c_\mu}}{\kappa^2} \\
v_t &= c_\mu (v R_T) D_1 D_2 \\
D_1 &= 1 - \exp\left(-\frac{y^+}{A^+}\right) \\
D_2 &= 1 - \exp\left(-\frac{y^+}{A_2^+}\right) \\
f_2(y^+) &= \frac{c_{\varepsilon 1}}{c_{\varepsilon 2}} + \left(1 - \frac{c_{\varepsilon 1}}{c_{\varepsilon 2}}\right) \left(\frac{1}{\kappa y^+} + D_1 D_2\right) \left(\sqrt{D_1 D_2} \right. \\
&\quad \left. + \frac{y^+}{\sqrt{D_1 D_2}} \left(\frac{1}{A^+} \exp\left(-\frac{y^+}{A^+}\right) D_2 + \frac{1}{A_2^+} \exp\left(-\frac{y^+}{A_2^+}\right) D_1\right)\right) \\
\kappa &= 0.41 \quad c_{\varepsilon 1} = 1.2 \quad c_{\varepsilon 2} = 2.0 \\
c_\mu &= 0.09 \quad A^+ = 26 \quad A_2^+ = 10
\end{aligned} \tag{2.38}$$

2.1.4.3. Spalart-Allmaras Turbulence Model

The transport equation for the turbulence variable \hat{v} is as shown in equation (2.39) for Spalart-Allmaras model [32]. The relation is integrated over control volumes. First order upwinding is implemented for the advective terms and the derivative terms are evaluated as explained in section 2.1.2. The left hand side of the equation is the total derivative term. The terms on the right hand side are production, dissipation and diffusion, respectively.

$$\begin{aligned}
\frac{D\hat{v}}{Dt} &= c_{b1}(1 - f_{t2})\hat{S}\hat{v} - \left[c_{w1}f_w - \frac{c_{b1}}{\kappa^2}f_{t2}\right]\left(\frac{\hat{v}}{d}\right)^2 \\
&\quad + \frac{1}{\sigma}[\nabla \cdot ((v + \hat{v})\nabla \hat{v}) + c_{b2}(\nabla \hat{v})^2]
\end{aligned} \tag{2.39}$$

The eddy viscosity is defined as follows.

$$\begin{aligned}
\mu_t &= \rho \hat{v} f_{v1} \\
f_{v1} &= \frac{X^3}{X^3 + c_{v1}^3} \\
X &= \frac{\hat{v}}{v}
\end{aligned} \tag{2.40}$$

\hat{S} is the modified vorticity and the Ω is calculated using the similar relations given in the explanation of the Baldwin-Lomax turbulence model.

$$\begin{aligned}
\hat{S} &= \Omega + \frac{\hat{v}}{\kappa^2 d^2} f_{v2} \\
f_{v2} &= 1 - \frac{X}{1 + X f_{v1}}
\end{aligned} \tag{2.41}$$

Closure functions and constants are as listed below.

$$\begin{aligned}
f_{t2} &= c_{t3} \exp(-c_{t4} X^2) \\
f_w &= g \left[\frac{1 + c_{w3}^6}{g^6 + c_{w3}^6} \right] \\
g &= r + c_{w2} (r^6 - r) \\
r &= \min \left[\frac{\hat{v}}{\hat{S} \kappa^2 d^2}, 10 \right] \\
c_{w1} &= \frac{c_{b1}}{\kappa^2} + \frac{1 + c_{b2}}{\sigma}
\end{aligned} \tag{2.42}$$

$$\begin{aligned}
c_{b1} &= 0.1355 \quad \sigma = 2/3 \quad c_{b2} = 0.622 \quad \kappa = 0.41 \quad c_{w2} = 0.3 \quad c_{w3} = 2.0 \\
c_{v1} &= 7.1 \quad c_{t3} = 1.2 \quad c_{t4} = 0.5
\end{aligned}$$

2.1.5. Thermodynamic Model

4th order polynomials and NASA Glenn [36] coefficients are used for the calculation of specific heat, enthalpy and entropy of the gas species. Since the conservative variable form of Navier-Stokes equations are used for the aerothermodynamics

analyses, temperature itself is not included as a variable in the energy equation. Thus the temperature is updated from the enthalpy of the gas mixture using Newton's method at each iteration of the flow field solution.

$$\frac{C_p(T)}{R} = a_1 T^{-2} + a_2 T^{-1} + a_3 + a_4 T + a_5 T^2 + a_6 T^3 + a_7 T^4 \quad (2.43)$$

$$\begin{aligned} \frac{H(T)}{RT} = & -\frac{a_1 T^{-2}}{2} - a_2 T^{-1} + a_3 \ln T + a_4 T + \frac{a_5 T^2}{2} + \frac{a_6 T^3}{3} \\ & + \frac{a_7 T^4}{4} + b_2 \end{aligned} \quad (2.44)$$

$$\begin{aligned} \frac{S(T)}{R} = & -\frac{a_1 T^{-2}}{2} + a_2 T^{-1} + a_3 \ln T + a_4 T + a_5 \frac{T^2}{2} + a_6 \frac{T^3}{3} \\ & + a_7 \frac{T^4}{4} + b_2 \end{aligned} \quad (2.45)$$

2.1.6. Flow Thermochemistry Calculation Method

Following Arrhenius type of relation is used for the calculation of forward reaction rate coefficients where A_f is the pre-exponential factor, β_f is the temperature exponent and E_f is the activation energy.

$$k_f = A_f T^{\beta_f} \exp\left(-E_f/RT\right) \quad (2.46)$$

Backward reaction rate coefficients are calculated using equilibrium constant K_r as shown below in equation (2.47).

$$k_b = \frac{k_f}{K_r} \quad (2.47)$$

Equilibrium constants of reactions are evaluated using the change of Gibbs free energy. Entropy and enthalpy values of reactant and product species are calculated via NASA Glenn polynomials [36] given in section 2.1.5.

$$K_r = \exp\left(\frac{\Delta S_r}{R} - \frac{\Delta H_r}{RT}\right) \quad (2.48)$$

The molar change rate of the i^{th} species due to the reaction r can be calculated using relation (2.49) where v'_{ir} and v''_{ir} are the stoichiometric coefficients of reactants and products, respectively and C_{jr} is the molar fraction of the j^{th} species in reaction r .

$$R_{ir} = (v''_{ir} - v'_{ir}) \left(k_f \prod_{j=1}^N C_{jr}^{v'_{ir}} - k_b \prod_{j=1}^N C_{jr}^{v''_{ir}} \right) \quad (2.49)$$

Since the reaction rates of high speed compressible flow problems may yield high temporal gradients of species mole fractions, the reaction rate values are set as the implicit unknowns of the Arrhenius type relations as follows.

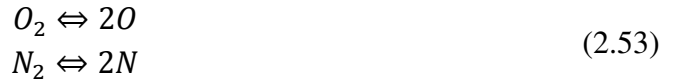
$$\sum_{r=1}^{r=RXN} R_{ir}^{n+1} - \frac{C_i^{n+1} - C_i^n}{\Delta t} = 0 \quad (2.50)$$

Combining the reaction rate definition (2.49) with the relation (2.50), results in the equation system of the form given in (2.51). The system is linearized with Newton's method which is given in equation (2.52) via setting the left hand side as the residual.

$$\sum_{r=1}^{r=RXN} (v''_{ir} - v'_{ir}) \left(k_f \prod_{j=1}^N (C_{jr}^{n+1})^{v'_{ir}} - k_b \prod_{j=1}^N (C_{jr}^{n+1})^{v''_{ir}} \right) - \frac{C_i^{n+1} - C_i^n}{\Delta t} = 0 \quad (2.51)$$

$$\left[-\frac{\partial R}{\partial W} \right] \Delta W = R \quad (2.52)$$

The size of the mass matrix of the linear system is $N \times N$ where N is equal to the number of the species included in the flow field analysis. As an example, equation set of the following artificial 2 step mechanism can be set as the residual vector of the system as shown in equation (2.54).



$$\begin{aligned} (0 - 1) \left(k_{f,1} (C_{O_2}^{n+1})^1 - k_{b,1} (C_O^{n+1})^2 \right) - \frac{C_{O_2}^{n+1} - C_{O_2}^n}{\Delta t} &= R_1, \quad \text{for } O_2 \\ (0 - 1) \left(k_{f,2} (C_{N_2}^{n+1})^1 - k_{b,2} (C_N^{n+1})^2 \right) - \frac{C_{N_2}^{n+1} - C_{N_2}^n}{\Delta t} &= R_2, \quad \text{for } N_2 \\ (2 - 0) \left(k_{f,2} (C_{N_2}^{n+1})^1 - k_{b,2} (C_N^{n+1})^2 \right) - \frac{C_N^{n+1} - C_N^n}{\Delta t} &= R_3, \quad \text{for } N \\ (2 - 0) \left(k_{f,1} (C_{O_2}^{n+1})^1 - k_{b,1} (C_O^{n+1})^2 \right) - \frac{C_O^{n+1} - C_O^n}{\Delta t} &= R_4, \quad \text{for } O \end{aligned} \quad (2.54)$$

It is possible to obtain the mass matrix of the example system via differentiating the residual equations and the linear system can be written as follows.

$$\begin{aligned}
& \begin{bmatrix} k_{f,1} + 1/\Delta t & 0 & 0 & -2k_{b,1}C_o \\ 0 & k_{f,2} + 1/\Delta t & -2k_{b,2}C_N & 0 \\ 0 & -2k_{f,2} & 4k_{b,2}C_N + 1/\Delta t & 0 \\ -2k_{f,1} & 0 & 0 & 4k_{b,1}C_N + 1/\Delta t \end{bmatrix} \begin{bmatrix} \Delta C_{O_2} \\ \Delta C_{N_2} \\ \Delta C_N \\ \Delta C_o \end{bmatrix} \\
& = \begin{bmatrix} R_1 \\ R_2 \\ R_3 \\ R_4 \end{bmatrix} \quad (2.55)
\end{aligned}$$

Linear systems are solved using the LU decomposition. Computed implicit mole fractions are used for the calculation of the reaction rates using equation (2.49). The chemical source terms of the Navier-Stokes problem are obtained from these reaction rate values.

2.1.7. Calculation of Mixture Viscosity and Species Diffusion Terms

Both of the Sutherland and Wilke [37] rules are included in the flow field analysis tool for the evaluation of laminar viscosity values. In Sutherland formulation, dynamic viscosity is the function of temperature only and the mass fraction of gas species are not considered as shown in the relation below:

$$\mu = \mu_{ref} \left(\frac{T}{T_{ref}} \right)^{0.66} \frac{T_{ref} + S}{T + S} \quad (2.56)$$

where μ_{ref} and T_{ref} are the reference viscosity and temperature respectively and S is the empirical constant.

For the implementation of Wilke rule, viscosity values of single species are calculated using the relation offered by Svehla [38]. In the relation (2.57); M_{wk} is the molecular weight of the species, σ_k is the collision diameter and $\Omega^{(2,2)*}$ is the reduced collision integral.

$$\mu_k = \frac{26.693 \sqrt{M_{wk} T}}{\sigma_k^2 \Omega^{(2,2)*}} \times 10^{-7} \quad (2.57)$$

The mixture viscosity is evaluated by using semi-empirical Wilke rule as follows.

$$\mu = \sum_{k=1}^N \frac{X_k \mu_k}{\sum_{j=1}^N X_j \phi_{kj}} \quad (2.58)$$

$$\phi_{kj} = \frac{1}{\sqrt{8}} \left(1 + \frac{M_{wk}}{M_{wj}} \right)^{-0.5} \left(1 + \left(\frac{\mu_k}{\mu_j} \right)^{0.5} \left(\frac{M_{wj}}{M_{wk}} \right)^{0.25} \right)^2$$

Equal diffusion coefficients are assumed for the species. Contributions of both laminar and turbulent diffusion phenomena are considered. Laminar coefficient is calculated with unity Lewis number assumption and Schmidt number is set to 0.9 for the evaluation of turbulent coefficient.

$$D = D_l + D_t \quad (2.59)$$

$$D_l = \frac{Le k}{\rho C_p} \quad (2.60)$$

$$D_t = \frac{\mu_t}{\rho Sc} \quad (2.61)$$

Diffusion flux terms are obtained using modified Fick's law.

$$J_{zi} = -\rho D \frac{\partial y_i}{\partial z} + \partial y_i \sum_{j=1}^N \rho D \frac{\partial y_j}{\partial z} \quad (2.62)$$

$$J_{ri} = -\rho D \frac{\partial y_i}{\partial r} + \partial y_i \sum_{j=1}^N \rho D \frac{\partial y_j}{\partial r} \quad (2.63)$$

2.2. Ablation Modeling

2.2.1. In-depth Energy Analysis

Inside the ablative materials, the following integral form of the heat conduction equation is solved.

$$\oint_{\partial V} \dot{q}'' \cdot dA - \oint_{\partial V} \rho e v_r \cdot dA - \frac{d}{dt} \int_V \rho e dV = 0 \quad (2.64)$$

The area vector is evaluated for axisymmetric geometries as in relation (2.65). Heat flux terms in radial and axial coordinates are modeled considering the possible anisotropy of the ablative material.

$$dA = 2\pi r \begin{bmatrix} dr \\ -dz \end{bmatrix} \quad (2.65)$$

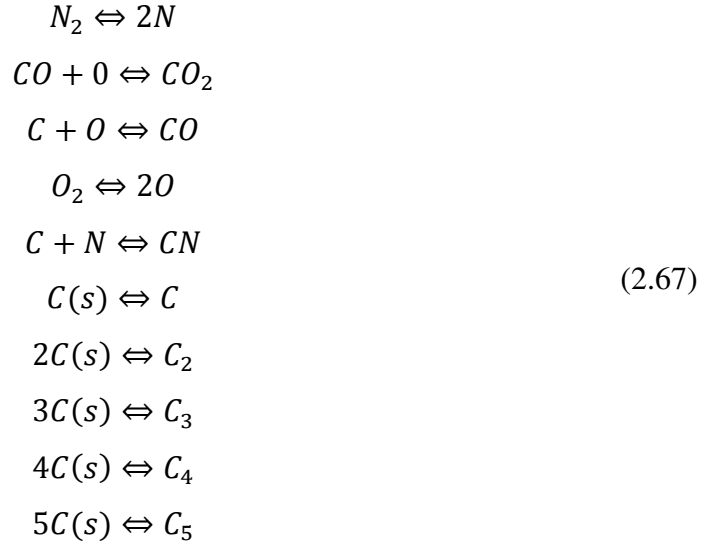
$$\dot{q}'' = \begin{bmatrix} k_{zz} & k_{zr} \\ k_{rz} & k_{rr} \end{bmatrix} \begin{bmatrix} \partial T / \partial z \\ \partial T / \partial r \end{bmatrix} \quad (2.66)$$

The second term in the heat conduction equation (2.64) is a Landau-like advection [39, 40] due to the recession of the surface. Advection velocity is set to be the recession velocity on the ablating wall and 0 on the back wall. Inside the solid domain, this term is assumed to be inversely proportional with the normal distance from the ablating wall.

2.2.2. Surface Thermochemistry Analysis

2.2.2.1. Graphite in Air

For ablation of graphite in air, nitridation, oxidation, combination/decomposition and sublimation reactions are considered [41, 42]. Wall temperature is obtained from the solid conduction solution and pressure is obtained from the aerothermodynamics analysis for the calculation of wall species mass fractions.



Twelve chemical species are included for the analysis. Equilibrium constant of each reaction can be defined as a function of partial pressures and stoichiometric coefficients of the species of the equilibrium system as shown in equation (2.68).

$$K_r = p_j^{v_j} p_i^{-v_i} \tag{2.68}$$

Besides, it is possible to evaluate the equilibrium constant as a function of wall temperature and empirical constants a and b [41, 42].

$$\log_{10} K_r = a - \frac{b}{T_w} \tag{2.69}$$

Combining the equations (2.68) and (2.69) provides a relation in the form below.

$$10^a 10^{-b/T_w} - p_j^{v_j} p_i^{-v_i} = 0 \tag{2.70}$$

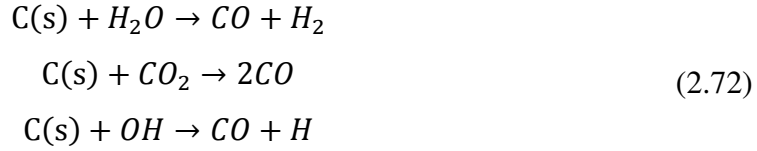
Also, the summation of the partial pressures of the gas species is equal to the boundary layer pressure provided by the aerothermodynamics analysis.

$$p_w - \sum_i^N p_i = 0 \quad (2.71)$$

Including the equations obtained from the equilibrium system and the summation of the partial pressures, there are eleven equations for twelve unknown partial pressures. In the graphite in air ablation problem, only C atoms are released to the boundary layer. Thus the ratio of N atoms to the O atoms is conserved during the process. System is closed using this property as the twelfth equation and the system is solved using Newton iterations.

2.2.2.2. Graphite in SRM

In SRM nozzle inserts, the static pressure is usually relatively high and sublimation of carbon is not an expected phenomenon. The main mechanism of the erosion is oxidation and the surface chemical reactions can be reduced to the finite rate mechanism given below [7, 43, 44].



Mass removal rate due to each of the heterogeneous reactions can be calculated using Arrhenius type of relation.

$$\dot{m}_i = p_i^n A_i T_w^b e^{\left(-\frac{E_i}{RT_w}\right)} \quad (2.73)$$

It is possible to obtain the recession rate from the total solid mass loss as follows.

$$\rho_s \dot{s} = \dot{m} = \dot{m}_{\text{H}_2\text{O}} + \dot{m}_{\text{CO}_2} + \dot{m}_{\text{OH}} \quad (2.74)$$

In case of aluminized solid propellants, working fluid total temperature is relatively high and the mass fraction of the oxidizers is relatively low since the oxygen atoms are held by the solid particles. Thus, reaction rates are fast and the oxidizers are

consumed quickly near the ablating wall. In this case, ablation rate is determined by the rate of gas species diffusion. On the other hand, for low temperature cases (i.e. non-metalized propellants) the ablation is limited by the heterogeneous reaction rates. Usage of finite rate reactions can be considered as a generalized method for both diffusion and reaction rate limited problems.

An equilibrium approximation can also be implemented for diffusion limited ablation cases with the assumption of infinitely fast reaction rates. Since sublimation is not likely to occur in SRM nozzle throats, steep changes of the species mass fractions with temperature variation are not expected. Below in Figure 2.3, changes of equilibrium mass fraction distributions with temperature are given for carbon ablation as an example. The results are obtained with Chemical Equilibrium Applications (CEA) code [45] for AP/HTPB propellant [9] at 30 bar constant pressure. One can realize that the mass fraction of C_3 begins to increase after 3500 K due to the sublimation and the mass fraction of the species are almost constant up to this point. Although this sublimation point is comparable with the recovery temperature of a non-reactive wall for most of the SRM nozzles, it is still far from the temperature levels of an ablating wall. Thus, previously prepared equilibrium tables for species mass fractions are less prone to interpolation errors for SRM nozzle problems.

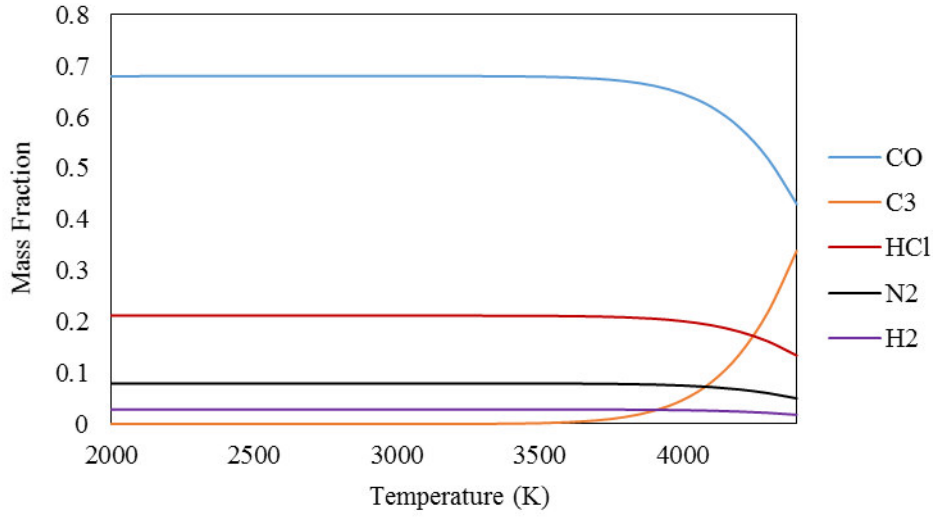


Figure 2.3. Variation of Species Mass Fractions with Wall Temperature (30 Bar)

Species mass fractions are obtained from previously prepared tables via interpolation for the ablation calculations with equilibrium assumption. Mass fraction values are tabulated with respect to wall temperature and pressure using CEA code [45]. An example table given below shows the equilibrium wall compositions for a 15% aluminized AP/HTPB propellant [46] at 2800 K wall temperature and between 0.5 and 25 bar boundary layer pressures.

Table 2.1. An Example Interpolation Table for Graphite Ablation (T=2800 K)

Pressure (Bar)	0.5	5.0	10.0	15.0	20.0	25.0
Al₂O₃	0.2527	0.2527	0.2527	0.2527	0.2527	0.2527
CN	0.0003	0.0001	0.0001	0.0001	0.0001	0.0001
CO	0.4074	0.4074	0.4074	0.4074	0.4074	0.4074
HCL	0.2166	0.2166	0.2167	0.2167	0.2167	0.2167
H₂	0.0326	0.0326	0.0326	0.0326	0.0326	0.0326
N₂	0.0900	0.0901	0.0902	0.0902	0.0902	0.0902

2.2.3. Ablation Boundary Condition

2.2.3.1. Boundary Condition for Decoupled Analysis

In the decoupled ablation calculations, Stanton type heat transfer coefficients are used. Initially, flow field analysis is completed with adiabatic wall boundary condition. The boundary layer edge properties which are obtained with aerothermodynamics analysis are used for heat and mass balance calculations of the ablation problem. It is assumed that the edge of the boundary layer is far enough from the reactive wall, thus the edge properties are not affected by the ablation phenomenon.

The unblown heat transfer coefficient is approximated using well-known Bartz correlation [3] for rocket motor nozzles.

$$\rho_e u_e St_0 = \frac{0.026}{D_*^{0.2}} \left(\frac{\mu}{Pr^{0.6}} \right) \left(\frac{p_c}{C^*} \right)^{0.8} \left(\frac{D_*}{r_c} \right)^{0.1} \left(\frac{A_*}{A} \right) \sigma \quad (2.75)$$
$$\sigma = \left[0.5 \frac{T_w}{T_c} \left(1 + \frac{\gamma - 1}{2} M^2 \right) + 0.5 \right]^{\frac{w}{5} - 0.8} \left(1 + \frac{\gamma - 1}{2} M^2 \right)^{-0.12}$$

In the correlation (2.75); ρ_e and u_e are the edge density and velocity, D_* and A_* are the throat diameter and area, C^* is the characteristic velocity, r_c is the radius of curvature of the throat and p_c is the combustion chamber pressure. A reduction of unblown coefficient is expected due to erosion. Blowing correction is implemented to the approximation as follows.

$$St = St_0 \frac{\ln(1 + 2\lambda B')}{2\lambda B'} \quad (2.76)$$

B' is the dimensionless mass blowing rate parameter and it is defined as the ratio of the mass blowing rate to the mass transfer coefficient.

$$B' = \frac{\dot{m}}{\rho_e u_e C_m} \quad (2.77)$$

Mass transfer coefficient is calculated with constant Lewis number assumption as shown below.

$$C_m = StLe^{2/3} \quad (2.78)$$

Mass balance between the boundary layer edge and the wall can be satisfied using the equation (2.79). The terms in the relation are mass diffusion from the boundary layer edge to the wall, source of gas species due heterogeneous surface reactions and the blowing due to ablation, respectively.

$$\rho_e u_e C_m (y_{e,i} - y_{w,i}) + \dot{w}_{wi} - \dot{m} y_{w,i} = 0 \quad (2.79)$$

If finite rate surface reactions are used, it is possible to calculate the mass blowing rate, \dot{m} , and the gas species source terms, \dot{w}_{wi} , using wall temperature and pressure. Rearranging the mass balance equation, mass fractions of the gas species can be obtained as follows [6].

$$y_{wi} = \frac{y_{ei} + \frac{\dot{w}_{wi}}{\rho_e u_e C_m}}{1 + \frac{\dot{m}}{\rho_e u_e C_m}} \quad (2.80)$$

One should note that, B' is used as a dummy variable in the current study for both finite rate and equilibrium calculations. For the equilibrium model with the decoupled approach, previously prepared lookup tables are used for the SRM nozzle throat erosion problem but, wall species mass fractions are tabulated rather than the B' value. Besides, different than the mass balance implementation of the finite rate calculations, initially, wall composition is obtained and then the mass blowing rate is calculated. The following elemental basis equation is used for the ablation analyses if wall equilibrium is assumed.

$$\rho_e u_e C_m (y_{ek} - y_{wk}) - \dot{m} y_{wk} + \dot{m} y_{sk} = 0 \quad (2.81)$$

where the first term is the mass diffusion from the boundary layer edge to the wall, second term is the mass leaving the wall due to blowing and the last term is the solid mass entering the control surface due to recession. The subscripts e, w, and s stand for edge, wall and solid, respectively. For a pure graphite or C/C material, y_{sk} is equal to 1 for C atom and equal to 0 for N and O atoms. The mass blowing rate can be calculated rearranging the relation (2.81) for C atom.

$$\dot{m} = \frac{\rho_e u_e C_m (y_{ek} - y_{wk})}{y_{wk} - 1} \quad (2.82)$$

The total heat flux to the wall is evaluated using the energy balance equation. The energy transfer mechanism shown in Figure 1.1 is implemented on the wall and only the radiative terms are neglected. The left hand side of the relation (2.83) is the heat conduction to the solid domain and the terms on the right hand side are energy transfer due to convection, mass diffusion, surface recession and blowing of the gas species, respectively.

$$\begin{aligned} -k_s \left. \frac{\partial T}{\partial n} \right|_s &= \rho_e u_e St (h_r - h_w)_e \\ &+ \rho_e u_e C_m \sum_{i=1}^N (y_{ei} - y_{wi}) h_{wi} + \dot{m} h_s - \dot{m} h_w \end{aligned} \quad (2.83)$$

The unblown heat transfer for hypersonic external flow conditions is calculated using the convective heating equation offered by Zoby et al [2]. This approximation considers the variation of the geometry via including the local Reynolds number based on the momentum thickness of the boundary layer. h_{aw} is the adiabatic wall enthalpy and obtained from the flow solution with adiabatic wall boundary condition. h_w is the wall enthalpy and a function of the wall temperature which is an unknown property of the ablation problem. Thus the heat transfer rate is updated at each iteration of the solid heating and ablation analyses.

$$\dot{q}_{w,0} = Re_{\theta}^{-1} \left(\frac{\rho^*}{\rho} \right) \left(\frac{\mu^*}{\mu} \right) \rho_e u_e (h_{aw} - h_w) Pr_w^{-0.6} \quad (2.84)$$

The momentum thickness is calculated as follows.

$$\theta = 0.664 \frac{\left(\int_0^s \rho^* \mu^* u_e r^2 ds \right)^{0.5}}{\rho_e u_e r} \quad (2.85)$$

where ρ^* and μ^* are the density and dynamic viscosity of the gas mixture calculated at the reference temperature of Eckert [47]. The ratios of the reference properties to the gas mixture properties are included in the relation in order to account for the effect of compressibility.

$$T^* = 0.5T_w + 0.22T_{aw} + 0.28T_e \quad (2.86)$$

Heat transfer coefficient is calculated using equation (2.87) and blowing correction is implemented. Elemental mass balance relation is used similar to the decoupled boundary condition of the nozzle throat erosion problem.

$$\rho_e u_e St_0 = \frac{\dot{q}_{w,0}}{h_{aw} - h_w} \quad (2.87)$$

Different than the internal flow conditions, outgoing radiation term is highly significant for the ablation problem under hypersonic external flow conditions, thus this term is not neglected in the energy balance calculations.

$$\begin{aligned} -k_s \frac{\partial T}{\partial n} \Big|_s &= \rho_e u_e St (h_r - h_w)_e \\ &+ \rho_e u_e C_m \sum_{i=1}^N (y_{ei} - y_{wi}) h_{wi} + \dot{m} h_s - \dot{m} h_w - \sigma \varepsilon T_w^4 \end{aligned} \quad (2.88)$$

2.2.3.2. Boundary Condition for Coupled Analysis

In the conjugate analyses; surface thermochemistry, aerothermodynamics and in-depth energy equations are solved simultaneously. Energy and mass balances are implemented on the ablating surface for both fluid and solid sides. Ablation products are injected into the boundary layer. In the mass balance equation given below, the first term is the diffusion of gas species from fluid side to the wall, second term is the species source due to heterogeneous reactions and the third term is the blowing due to ablation.

$$J_{wi} + \dot{w}_i - \dot{m}y_i = 0 \quad (2.89)$$

Energy balance equation includes the heat conduction to the solid, convection from fluid to the wall, enthalpy of diffusing gasses, enthalpy of the solid entering the control surface due to recession and the outgoing radiation.

$$-k_s \frac{\partial T}{\partial n} \Big|_s = k_f \frac{\partial T}{\partial n} \Big|_f + \sum_{i=1}^N J_{wi} h_{wi} + \dot{m} h_s - \dot{m} h_w - \sigma \epsilon T_w^4 \quad (2.90)$$

Resolutions of both temperature and species mass fraction gradients are required for an accurate implementation of energy balance. Laminar coefficients are used for the calculation of convective and diffusive terms. Modified Fick's law is utilized for the evaluation of mass diffusion fluxes similar to the flow field analysis.

$$J_{wi} = \rho D \frac{\partial y_{wi}}{\partial n} - y_{wi} \sum_{j=1}^N \rho D \frac{\partial y_{wj}}{\partial r} \quad (2.91)$$

CHAPTER 3

VALIDATION AND VERIFICATION OF SUBMODELS

3.1. Solid Conduction Model

In-depth conduction model is tested using three different problems. Initially, 1-D Teflon ablation is analyzed. It is assumed that the recession begins after reaching a specific wall temperature and remains constant during the melting period. Secondly, a 1-D ablation problem is solved numerically with the assumption of constant and previously known recession velocity. Carbon/carbon material properties are used and the results are compared with the analytical solutions. Finally, the flux calculation method is validated with a simple heat transfer problem on a 2-D plate. A skewed structured mesh is used and the time accurate results are compared with the analytical calculations.

3.1.1. Stefan (Melting) Problem

In this section, 1-D transient Teflon ablation is analyzed. Similar problem with the study of Ruperti et al [48] is selected for the verification. Computational results are compared with the Generalized Integral Transform Technique (GITT) solution results of the reference paper.

In the modeling study, it is assumed that the only source of the ablation is melting and the wall temperature remains constant after reaching the ablation temperature. The aerodynamic heating history is previously known and the total duration of the heating is about 45 seconds with a peak heat flux of about 4500 kW/m^2 . Initial and ablation temperatures are 416 K and 833 K, respectively. Material density is 1922 kg/m^3 and the depth of the ablator is 0.0065 m.

The problem is composed of two parts which are non-ablating and ablating phases. The boundary conditions of the non-ablating part of the problem are as follows.

$$-k \frac{\partial T}{\partial x} = q(t) \quad x = 0 \quad (3.1)$$

$$-k \frac{\partial T}{\partial x} = 0 \quad x = L \quad (3.2)$$

where $x = 0$ is the coordinate of the wall which is exposed to heat flux and $x = L$ is the adiabatic back wall of the material. The boundary conditions switch to the boundary conditions of the ablating part when the melting temperature is reached. The final temperature distribution of the first part of the heating problem is used as the initial condition of the second phase. In the energy balance equation given below, the term in the left hand side is the rejected total enthalpy due to material removal. The first and second terms in the right hand side are the aerodynamic heating and the heat conducted into the material, respectively.

$$\rho h \frac{\partial s}{\partial t} = q(t) + k \frac{\partial T}{\partial x} \quad x = s \quad (3.3)$$

The temperature of the ablating wall is held constant and the adiabatic wall boundary condition is preserved on the back wall. s stands for the instantaneous total recession length and T_{ab} is the ablation temperature.

$$\begin{aligned} T &= T_{ab} \quad x = s \\ -k \frac{\partial T}{\partial x} &= 0 \quad x = L \end{aligned} \quad (3.4)$$

Computational results are obtained with a 51 node grid and $\Delta t = 0.01$ s. Calculated temperature distributions inside the Teflon material are shown in Figure 3.1 for various instants.

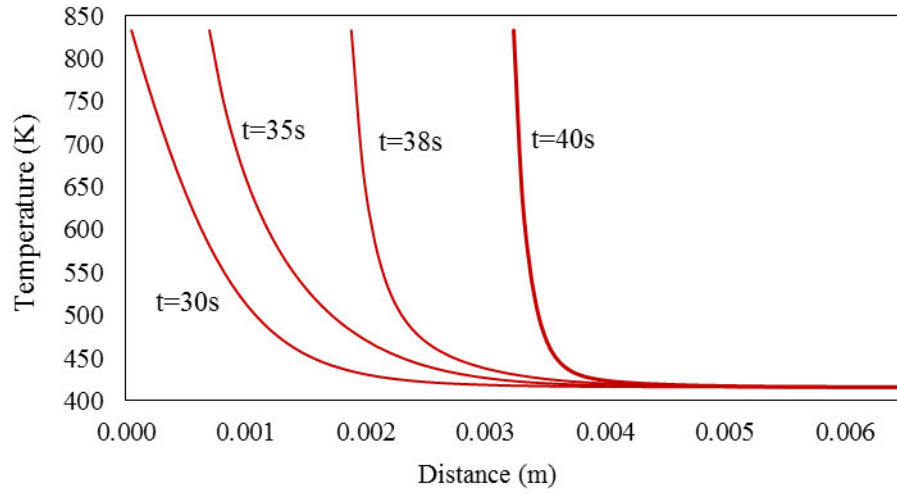


Figure 3.1. Variation of Temperature Distribution inside the Teflon Ablator

Comparison of the current numerical analysis results with the results of the reference study is shown in Figure 3.2 for the time accurate variation of the recession. Ablation begins at about $t = 28.5$ s and the total recession is calculated as 5.82 mm. Comparison shows that, two computations are highly coherent during the whole aerodynamic heating.

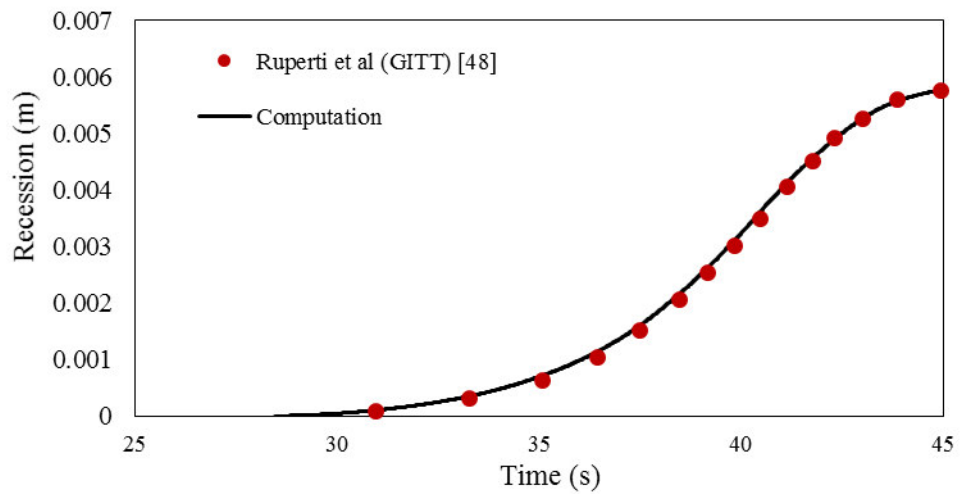


Figure 3.2. Comparison of the Calculated Recession with the Reference Study [48]

3.1.2. 1-D Ablation Problem with Known Recession Velocity

Ablation with previously known recession velocity and constant wall temperature is a common problem for the validation of ablation modeling studies [49, 50] since the analytical solution is available. The problem reduces to a steady state problem for a semi-infinite slab and the temperature distribution can be calculated with the relation below.

$$\frac{T(x) - T_i}{T_{abl} - T_i} = e^{-\frac{ds}{dt} \frac{x}{\alpha}} \quad (3.5)$$

Initial and ablation temperatures of the ablator are assumed to be 200 K and 2000 K, respectively. Initial depth of the domain is set to 0.2 m with a 2×10^{-3} m/s recession velocity. Adiabatic wall boundary condition is used on the back wall since it is not possible to use a semi-infinite domain in the numerical calculations. Computational results are obtained with a 101 node grid and $\Delta t = 0.1$ s. Carbon/carbon composite material properties are used. Calculated wall temperature distributions at $t=30, 50, 75$ s are compared with the analytical results in Figure 3.3.

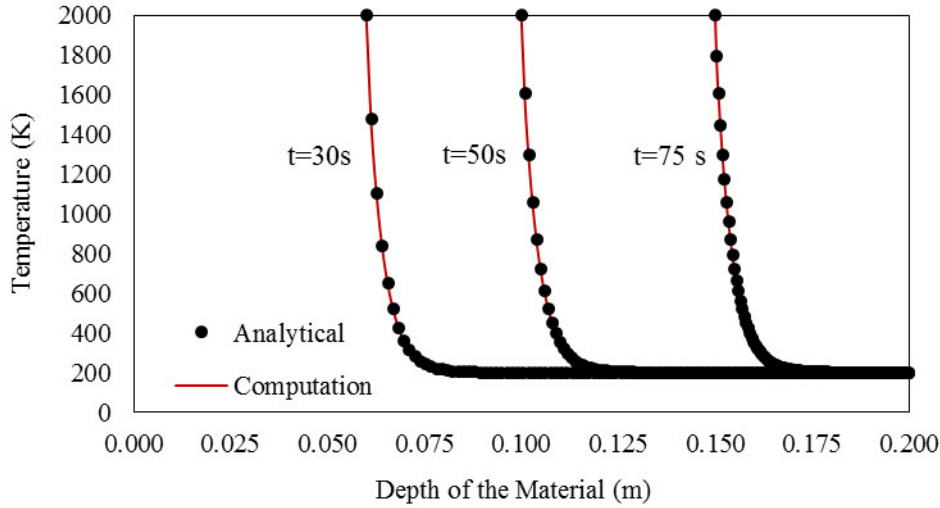


Figure 3.3. Comparison of Calculated Temperature Distributions with the Analytical Solution

3.1.3. 2-D Conduction Problem

In the previous numerical studies which are given in Sections 3.1.1 and 3.1.2, 1-D solid domains have been considered. In this section, accuracy of the 2-D flux calculation method is tested and time accurate temperature distributions are calculated on a square shaped plate. The boundary conditions and the description of the problem is shown in Figure 3.4.

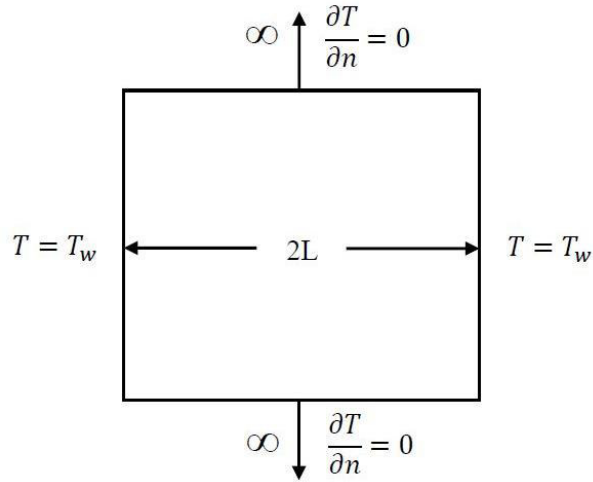


Figure 3.4. Description and the Boundary Conditions of the Validation Problem

The case is 1-D by its nature due to the implemented boundary conditions and the analytical solution of the problem is available [51]. The following dimensionless variables can be defined for temperature, length and time.

$$\theta = \frac{T - T_w}{T_i - T_w}, \quad X = \frac{x}{L}, \quad \tau = \frac{\alpha t}{k} \quad (3.6)$$

The dimensionless temperature distribution on the horizontal line can be calculated analytically using the relations below [51] and no variation of temperature is expected vertically.

$$\begin{aligned}
\theta &= \sum_{n=1}^{\infty} A_n \exp(-\lambda_n^2 \tau) \cos(\lambda_n X) \\
A_n &= \frac{4 \sin(\lambda_n)}{2\lambda_n + \sin(2\lambda_n)} \\
\lambda_n \tan(\lambda_n) &= Bi \\
Bi &= \frac{hL}{k}
\end{aligned} \tag{3.7}$$

where Bi is the Biot number and it is equal to infinity for the current problem since the wall temperature is held constant. A 52x52 structured grid is used for the numerical analysis and it is shown in Figure 3.5. The grid is skewed intentionally in order to check if any spurious results are created due to the flux calculation approach.

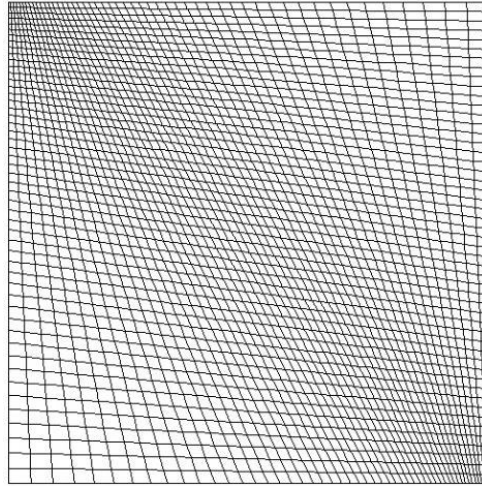


Figure 3.5. 52x52 Structured Grid (intentionally skewed)

Calculated dimensionless temperature contours are shown in Figure 3.6 at $\tau = 0.2, 0.4, 0.6$ and 0.8 . One can realize that no spurious results are generated due to the skewness of the numerical grid. The probable reason of the barely recognizable wiggles on the contour lines is the reconstruction of the data on the nodes for post processing. The comparison of the numerical and analytical results on the horizontal centerline are also

given in Figure 3.7 at $\tau = 0.2, 0.4, 0.6, 0.8$ and 1.0 and highly consistent results are observed.

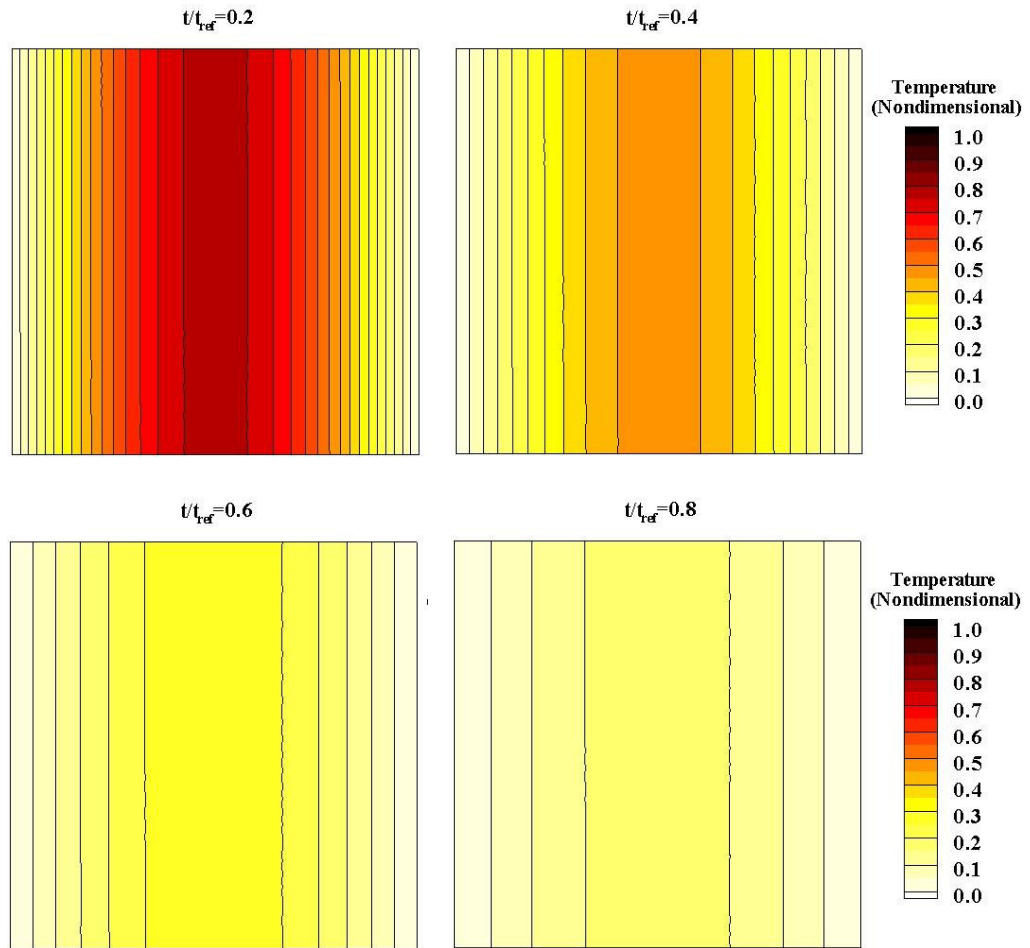


Figure 3.6. Calculated Temperature Distributions $\tau = 0.2, 0.4, 0.6$ and 0.8

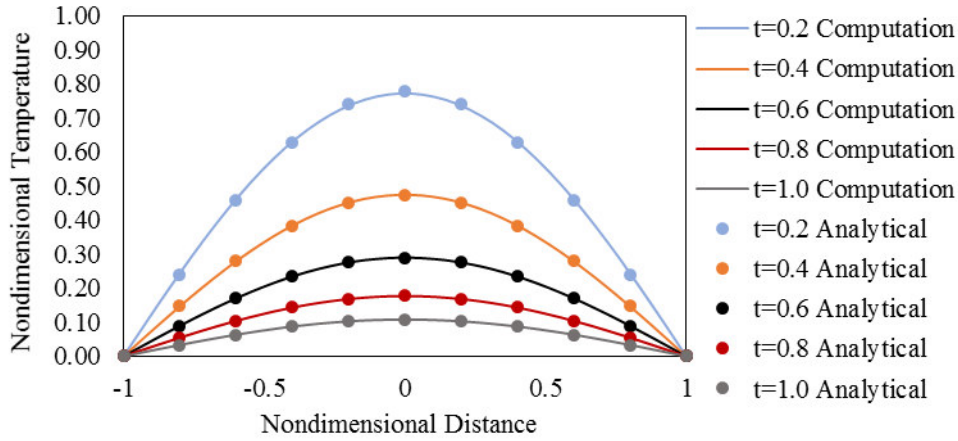


Figure 3.7. Comparison of Numerical and Analytical Results

3.2. Surface Thermochemistry Model

As stated in Section 2.2.3.1, nondimensional blowing rate parameter is not one of the key parameters of the current numerical modeling study. Direct calculation is performed for the wall gas mixture composition for graphite in air problem. In the current verification study, the variation of B' with pressure and temperature is calculated only for the comparisons with the computational results from the literature [50,52,53].

Dividing the terms of the elemental mass balance equation by the mass transfer coefficient provides the relation below which includes only the elemental mass fractions and the B' value.

$$(1 + B')y_{wk} - B'y_{sk} - y_{ek} = 0 \quad (3.8)$$

Assuming that the boundary layer is thick enough and no C atoms exist at the edge of the boundary layer, and the ablative material consists of C atoms only, the elemental mass balance relations can be reduced to the following form.

$$\begin{aligned}
y_{sC} &= 1, & y_{eC} &= 0, & y_{sO} &= 0, & y_{sN} &= 0 \\
(1 + B')y_{wO} - y_{eO} &= 0 \\
(1 + B')y_{wN} - y_{eN} &= 0 \\
(1 + B')y_{wC} - B' &= 0
\end{aligned} \tag{3.9}$$

For graphite ablation in air, total of 10 reactions are utilized for the calculation of partial pressures of the species. Relations in the form given below are used for the evaluation of the equilibrium composition.

$$10^a 10^{-b/T_w} - p_j^{v_j} p_i^{-v_i} = 0 \tag{3.10}$$

Closing the system using the following relations for elemental mass fractions and partial pressures provides complete set of equations for the B' value.

$$\begin{aligned}
y_{wk} &= \frac{M_k}{pM} \sum_{i=1}^N v_{ki} p_i \\
p_w - \sum_i^N p_i &= 0
\end{aligned} \tag{3.11}$$

The requirement for the solution of the equation set is the knowledge of wall temperature, pressure and the boundary layer edge composition. There are seventeen unknowns in the system including twelve partial pressures, three elemental mass fractions, molecular weight of the gas mixture and the B' value. Also there are total of seventeen equations which are already explained.

Figure 3.8 shows the calculated values of blowing rate parameter, B' , as a function of surface temperature and pressure. These values are evaluated for the known values of the boundary layer edge properties. In these calculations, the ratio of the mass fractions of oxygen to nitrogen y_O/y_N is assumed to be 0.307 at the edge of the boundary layer. The figure shows that the calculated values at 102325 Pa are in good agreement with respect to the values in references [50,52,53]. In Figure 3.9, at 101325 Pa boundary

layer edge pressure, the variations of partial pressure for different species are shown with respect to wall temperature. As seen from the figure, the species compositions at the wall surface significantly change with the temperature.

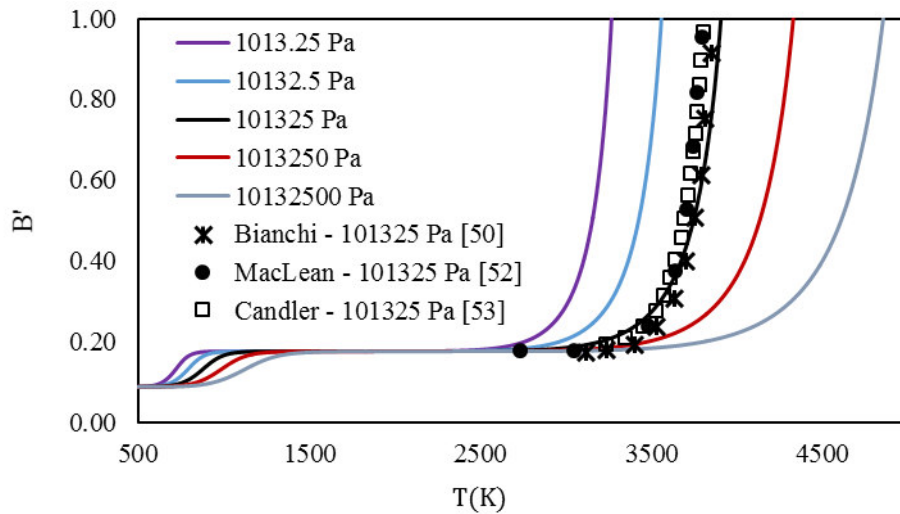


Figure 3.8. Comparison of blowing rate parameters at 101325 Pa with Computational Results from References [50, 52, 53]

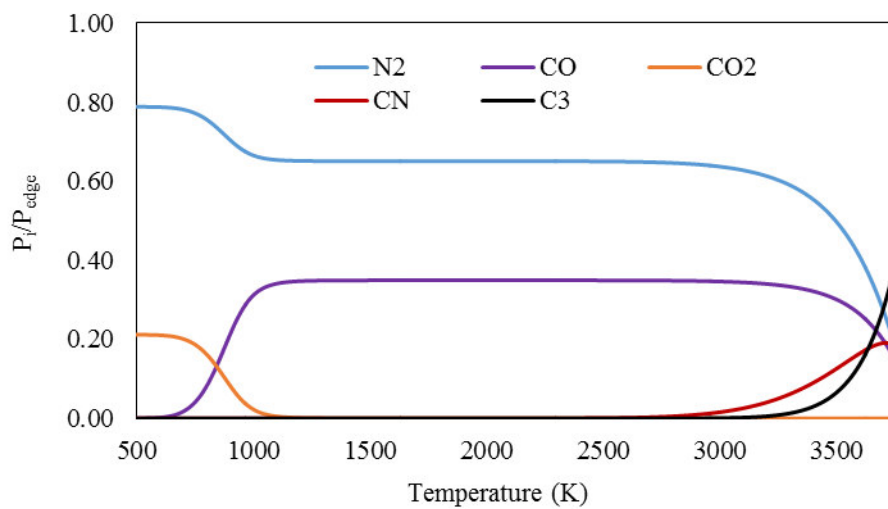


Figure 3.9. Partial pressures of species on ablating wall at 101325 Pa boundary layer edge pressure

Newton's method is implemented for the solution of the equation system. One remarkable property of the Newton's method is that a quadratic convergence can be achieved if a good initialization is provided. In the solutions of strongly nonlinear thermochemistry equations, the effects of initialization on the convergence of Newton's method are studied. In an example problem, the wall temperature and pressure are set to 4000 K and 1 atm, respectively. Iterations start from different initial conditions given in Table 3.1. In the first condition, the values are arbitrarily assigned. In the others, the solutions evaluated at 3900 and 3950 K are utilized as initial conditions. The number of Newton iteration required for the convergence are also given in Table 3.1. Results show that, iteration number can be reduced significantly if the initial and final solutions are close to each other.

Table 3.1. Different initialization cases for single point solution of B'
(Boundary Layer Edge Properties: 4000 K and 1 atm)

Variable	Solution	Init.1	3900 K Init. 2	3950 K Init. 3
y_{wO}	8.2105×10^{-2}	0.1000	0.1191	0.1020
y_{wC}	0.6502	0.1000	0.4925	0.5653
y_{wN}	0.2676	0.1000	0.3883	0.3326
B'	1.8593	0.1000	0.9705	1.3007
M_w	28.9963	30.0000	28.1992	28.523
No of Iterations		71	58	9

3.3. Flow Thermochemistry Model

In the current section, solution method for finite rate chemical equation systems is tested for high temperature air. Since it is not an easy task to test the time accuracy of finite rate reactions, verification study is carried on for the final equilibrium compositions of the reaction sets. Initial mass fractions of air species are set to 0.76 and 0.24 for N_2 and O_2 molecules, respectively. The temperature of the air mixture is held constant at various points and the reactions are marched in time until the residuals

of the mass fractions reach the machine epsilon. Final compositions of the solutions are compared with the equilibrium results of CEA [45].

In the first case, a reaction set with 17 steps is tested. The detailed chemical mechanism is given in Appendix A and forward reaction rate constants can be found in reference [54]. This reaction steps exclude the ionization of the gas species. Thus, the ionized species are also excluded from the CEA calculations. Pressure is set to 1500 Pa for each temperature point. Below in Figure 3.10, comparison of converged results of finite rate reactions and CEA results are compared.

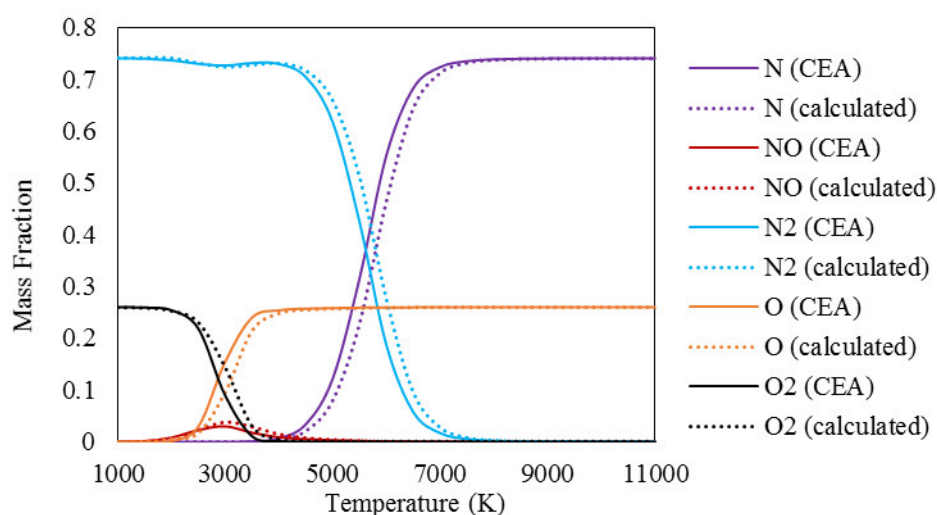


Figure 3.10. Converged Species Mass Fraction Results of Marching Solution with 17 Reactions and Comparison with CEA Equilibrium Results (1500 Pa)

As a second study, reaction set with 49 steps is selected using the similar air composition. Details of the reaction mechanism is also given in Appendix A. Forward reaction rate constants are adapted from the study of Park [55]. Ionization reactions are included in the system and comparison of the converged finite rate solutions with CEA results are given in Figure 3.11.

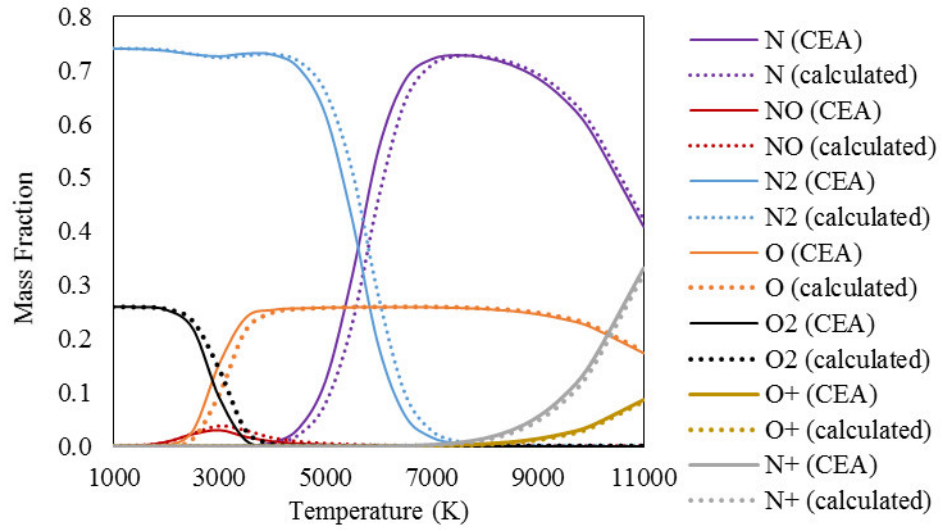


Figure 3.11. Converged Species Mass Fraction Results of Marching Solution with 49 Reactions and Comparison with CEA Equilibrium Results (1500 Pa)

The species mass fraction variations are mostly coherent for two computations. The main difference between the results is observed on the temperature ranges where the decomposition of O_2 and N_2 molecules take place. The probable reasons of the discrepancy are the difference between the calculation methods and the reaction rate constants which are used in the finite rate calculations. In Figure 3.11, a higher consistency is observed in the ionization region than the decomposition of the species.

The variation of the species mass fractions with time is computed at $T=12000$ K and $p=1500$ K as an example marching solution. Initial gas composition which is used for the calculations is given in Table 3.2. The results are shown in Figure 3.12 for the species O, O^+ , N_2 , N and N^+ . The oxygen is totally dissociated in the initial gas mixture. On the other hand, the nitrogen is partially dissociated and the initial mass fraction of the N_2 is 0.6169. The dissociation of the nitrogen molecules is completed at about $t = 0.5 \times 10^{-4}$ s and the production of N^+ begins. The mixture composition becomes almost constant beginning from $t = 2 \times 10^{-4}$ s and the system reaches to equilibrium state.

Table 3.2. *Initial Species Mass Fractions [20] – Air Reactions*

N_2	O_2	NO	N	O
0.6169	0	0.0046	0.1212	0.2573

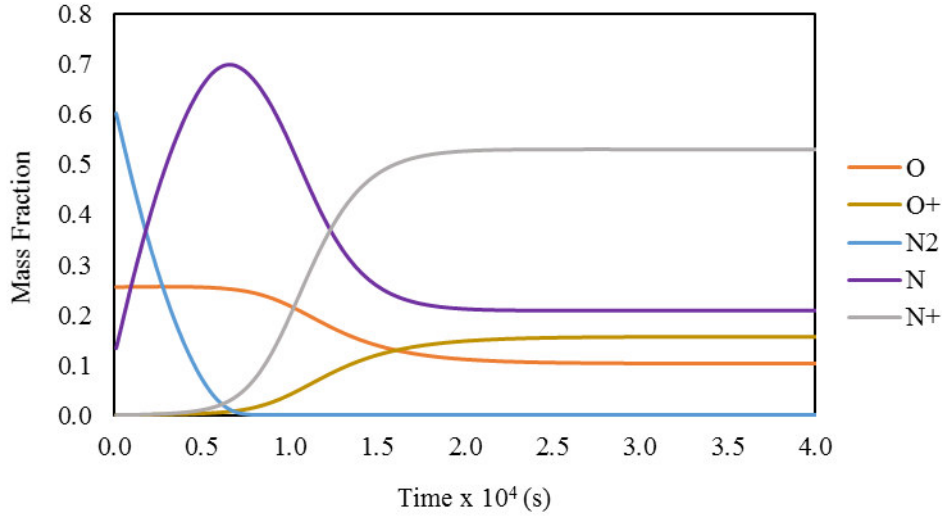


Figure 3.12. Variation of Species Mass Fractions with Time ($T=12000$ K, $p = 1500$ Pa)

The chemical kinetic parameters which are used in the reacting flow solutions of SRM nozzles are also tested. The 16 step reduced mechanism of Schneider et al [56] is used for the computations. The detailed mechanism is given in Appendix A and the initial gas mixture of the current verification study is shown Table 3.3.

Table 3.3. *Initial Species Mass Fractions [56] – SRM Nozzle Reactions*

CO	CO ₂	H ₂	H ₂ O	H	OH	O	O ₂	N ₂	HCl
0.27	0.23	0.01	0.41	0.00	0.01	0.00	0.00	0.01	0.06

The variations of the species mass fractions with temperature are compared with CEA results in Figure 3.13. The pressure is held constant at 50 Bar. The results show that, two computations are highly coherent between the temperature values of 1200 and

3000 K. The expected temperature of the core flow on the throat location of a nozzle is usually between these limits. The discrepancies of the computed mass fractions increase with the decreasing temperature below 1200 K. This lower limit is far from the expected temperature values of the expanded gas mixtures at the nozzle exits. On the other hand, the discrepancy between the species composition calculations above the 3000 K might yield steep changes at the inlet of the nozzle flow analyses results since the inlet boundary conditions are usually obtained from the equilibrium compositions.

As an example, a transient solution at $T=1000$ K and $p = 50$ bar is given in Figure 3.14 for H_2O , CO_2 and CO molecules using the initial gas composition given in Table 3.3.

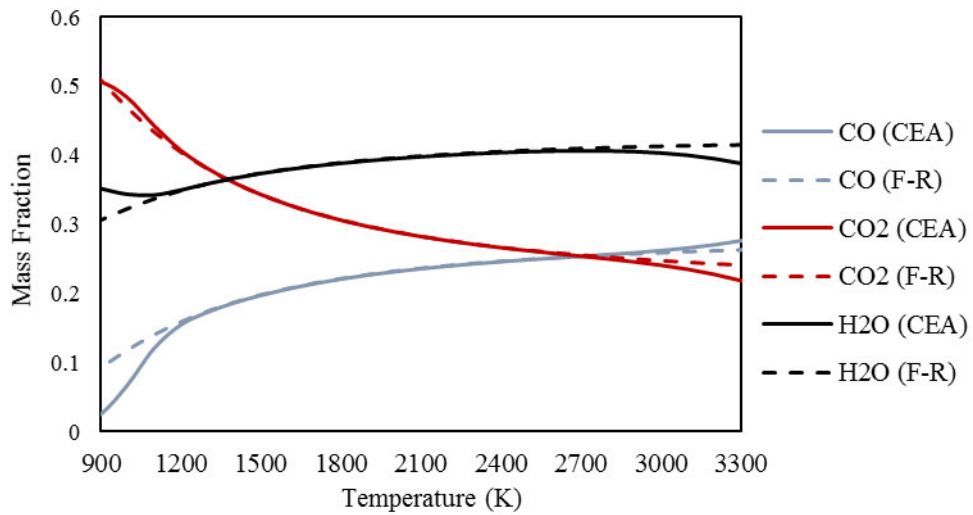


Figure 3.13. Converged Species Mass Fraction Results of Marching Solution with SRM Nozzle Reactions and Comparison with CEA Equilibrium Results (50 Bar)

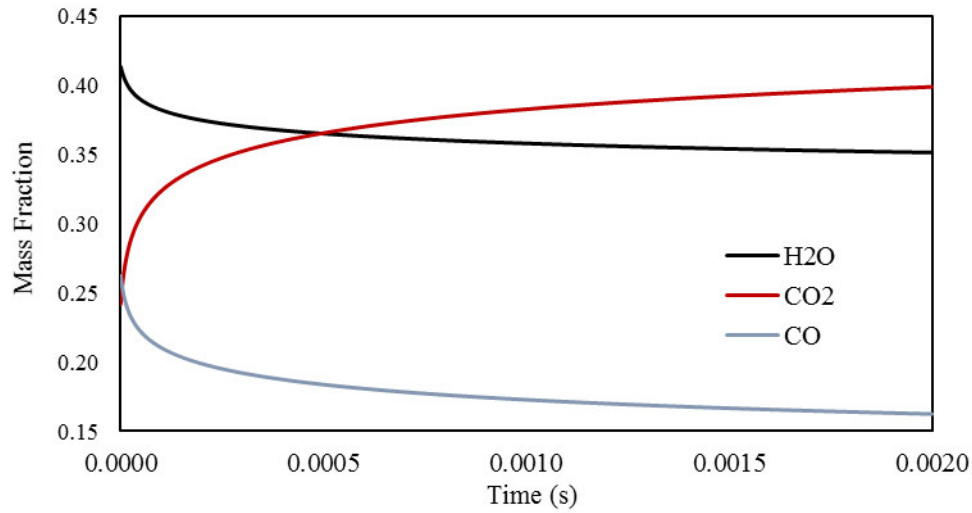


Figure 3.14. Variation of Species Mass Fractions with Time ($T=1000$ K, $p = 50$ Bar)

3.4. Aerothermodynamics Model

Flow around a spherical blunt nose under hypersonic flow conditions is analyzed for the validation of the aerothermodynamics model. The computed shock standoff distance is compared with the experimental results of Lobb [57] as well as the computational results of Yumusak and Eyi [58]. Free stream Mach number for the problem is 7.1 and the sphere has a 1.27 cm (0.5 inch) diameter. Details of the free stream conditions are given in Table 3.4. A viscous and reactive flow solution is conducted using 17 step reaction mechanism [54] and 5 gaseous species which are mainly N_2 , O_2 , NO , O and N . Adiabatic wall boundary condition is implemented on the surface of the sphere.

A grid convergence study is carried on using 60x35, 90x55, 120x70 and 180x110 structured grids. The views of the grids can be seen in Appendix B. The variation of the shock standoff distance with the increasing cell numbers is given Figure 3.15. Convergence of the computational results to the experiment can be clearly seen.

Table 3.4. *Free Stream Conditions of Lobb's Experiment [57]*

T_∞	P_∞	M_∞	N_2	O_2
293 K	664 Pa	7.1	0.763	0.237

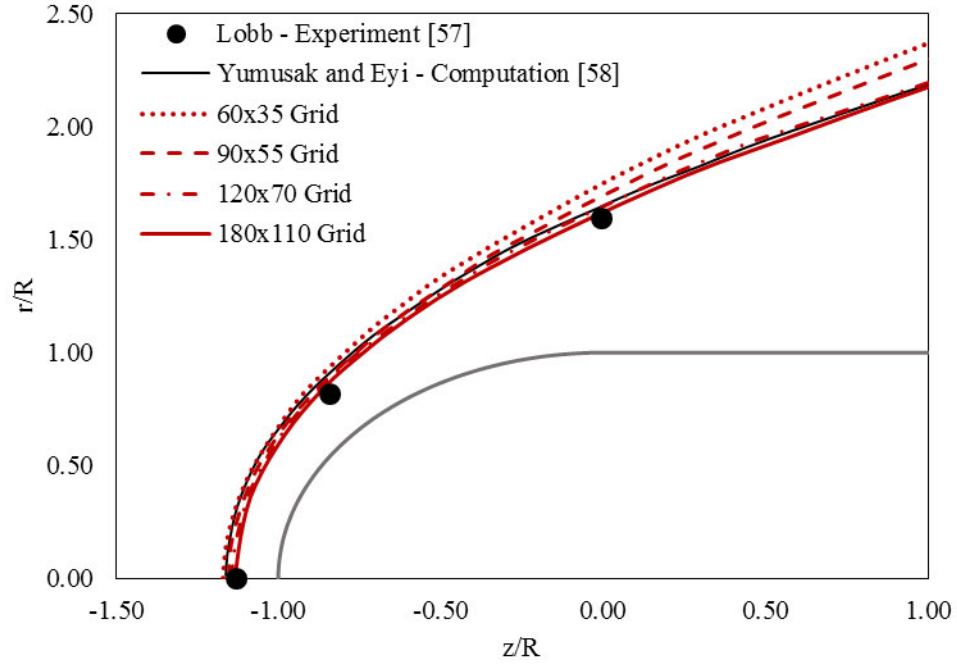


Figure 3.15. Grid Convergence Study and Comparison of Shock Standoff Distances

In Figure 3.16, contours of Mach number, pressure, temperature and density are given. Calculated stagnation temperature is about 2800 K and the pressure is about 46000 Pa.

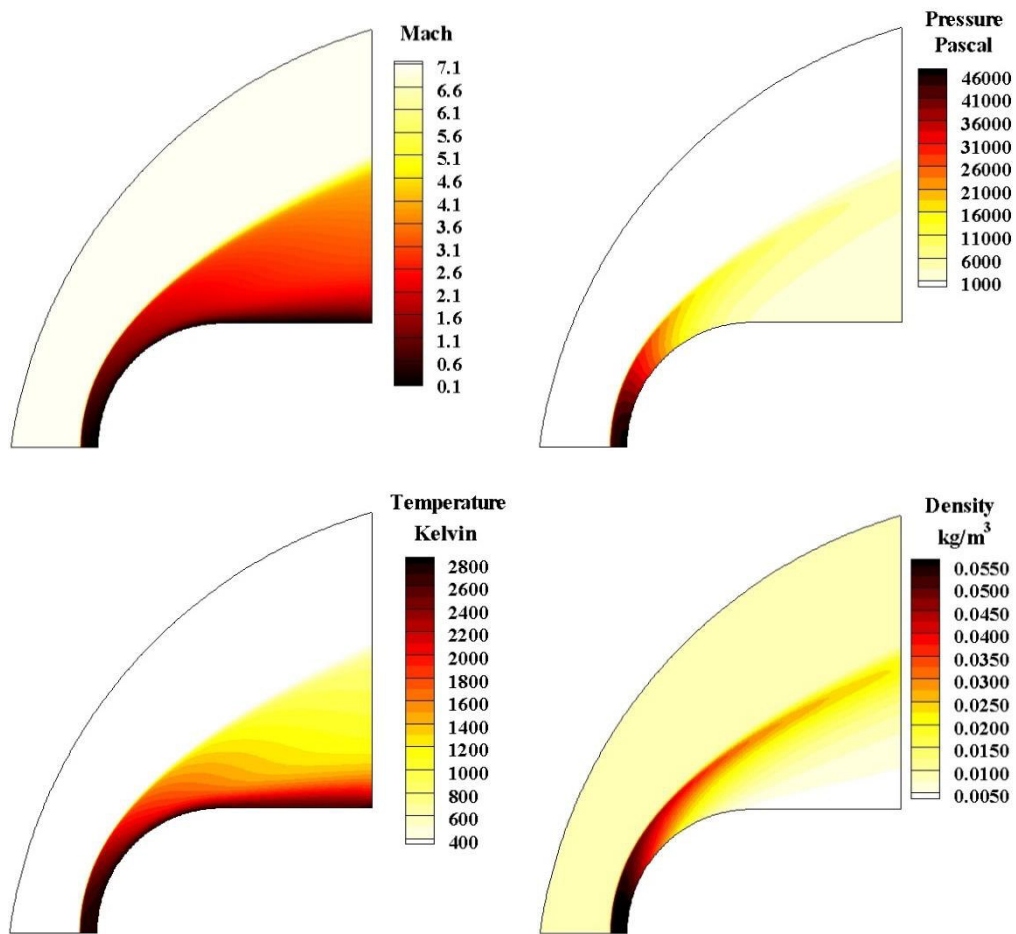


Figure 3.16. Distributions of Mach number, Pressure, Temperature and Density

Temperature distributions of viscous and inviscid solutions are compared in Figure 3.17 for 180x100 grid. Development of the boundary layer results in an increase of the shock standoff distance and the recovery of the temperature near the wall. Thus, a remarkable difference is observed between two analysis results.

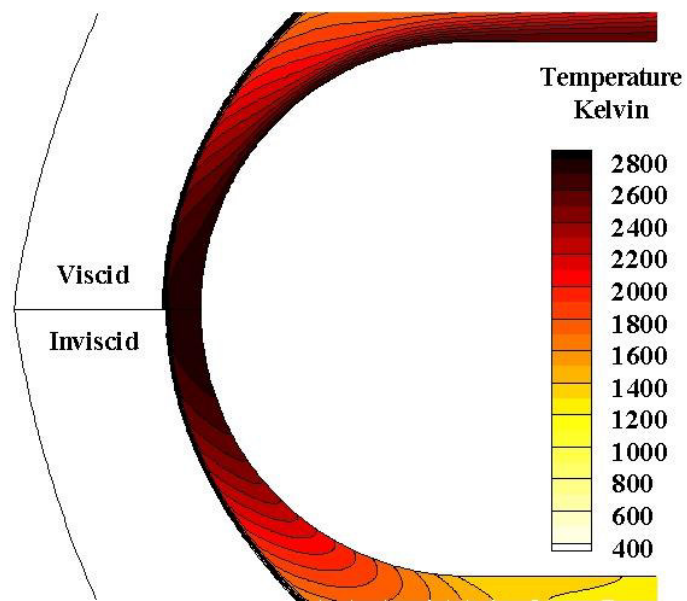


Figure 3.17. Comparison of Temperature Distributions for Viscid and Inviscid Solutions

CHAPTER 4

GRAPHITE IN AIR ABLATION MODELING RESULTS

4.1. Problem Definition and Grid Convergence Study

Initially, a grid convergence study is carried on in order to reveal the effect of the grid size on the flow field solution results. An ablation test case of a graphite specimen which is exposed to arc-jet flow is selected from the literature [20]. The graphite nose-tip has a 1.905 cm radius with a 10° of cone angle and the free stream conditions of the test is given in Table 4.1. Air stream is composed of partially decomposed N_2 , fully decomposed O_2 and small amount of NO molecules. Flow is assumed to be laminar referring to the studies [22, 23] on the similar test case.

Table 4.1. Free Stream Conditions of Arc-Jet Test [20,22,23]

T_∞	V_∞	ρ_∞	N_2	O_2	NO	N	O
1428 K	5354 m/s	0.003 kg/m ³	0.6169	0	0.0046	0.1212	0.2573

In the directions tangent and normal to the wall; 41x21, 81x41, 96x52 and 121x61 structured cells are used and the wall is assumed to be adiabatic for these preliminary flow field analyses. The views of the grids are given in Appendix B. Initially, the computations are carried on with frozen flow assumption and the flow field reactions are activated after 10000 iterations. In Figure 4.1 residual histories of the numerical solutions are given for density, energy and z momentum values. Variations of the velocity magnitude and density are given along the stagnation line in Figure 4.2 (a). Besides, pressure and adiabatic temperature distributions along the wall are shown in Figure 4.2 (b). Decrease of the dependency on the grid size is observed with increasing cell numbers. The highest variation due to the change of the grid size is on the adiabatic wall temperature, since the reduced cell size near the wall results in a better

resolution of the thermal boundary layer. On the other hand, the change in the wall pressure is the lowest since this property remains almost constant in the normal direction to the wall. The results of 96x52 and 121x61 grids are close to each other. 96x52 grid is selected for the rest of the numerical studies in order to decrease the computational cost. Although the number of iterations for the convergence are close to each other for 96x52 and 121x61 cell domains, the computational cost per iteration is about 80 % higher for the finest grid.

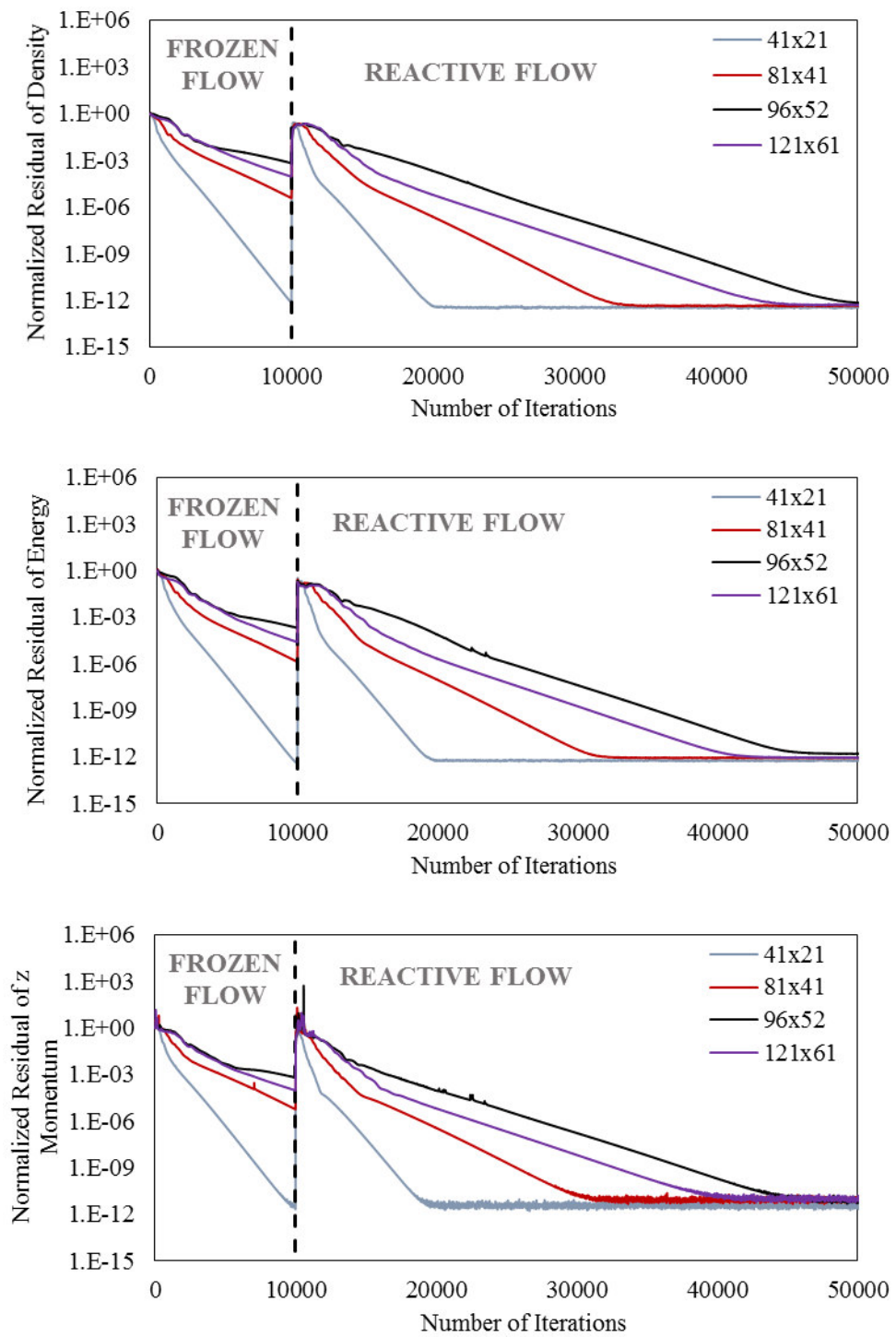
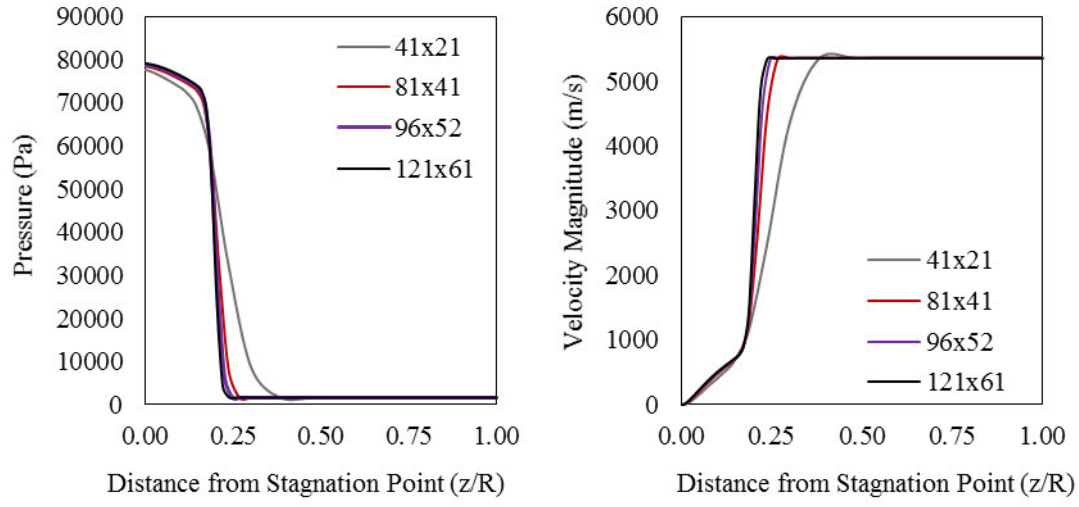
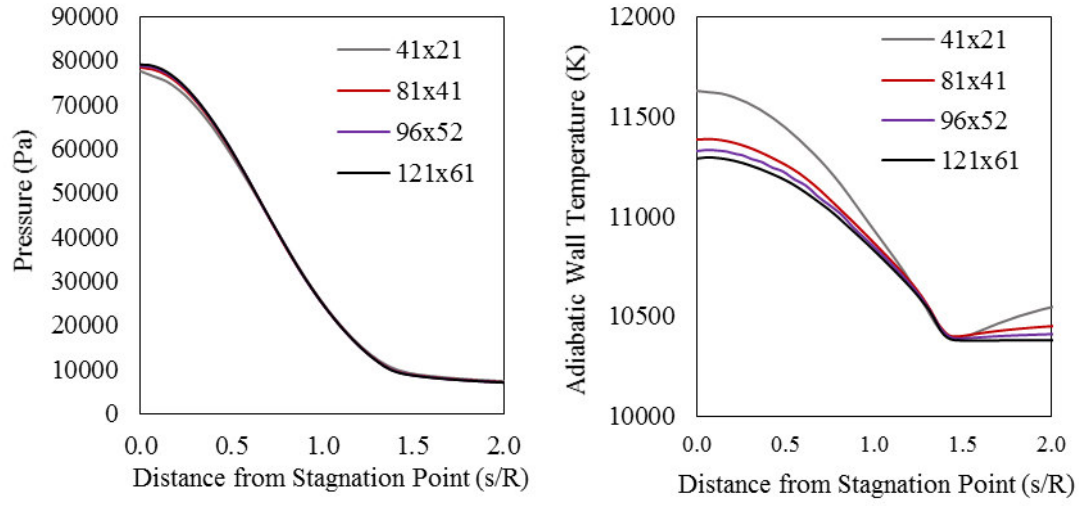


Figure 4.1. Residual Histories for Grid Convergence Study



(a)



(b)

Figure 4.2. Grid Convergence Study - Variation Along (a) Stagnation Line (b) Nose-tip Surface

In Figure 4.3 the contour plots of numerical results with 96x52 grid are shown. The computed stagnation temperature and the pressure are about 12000 K and 80000 Pa, respectively. The highest NO mass fraction is observed near the intersection point of

stagnation and shock lines and N_2 molecules are totally dissociated near the stagnation point.

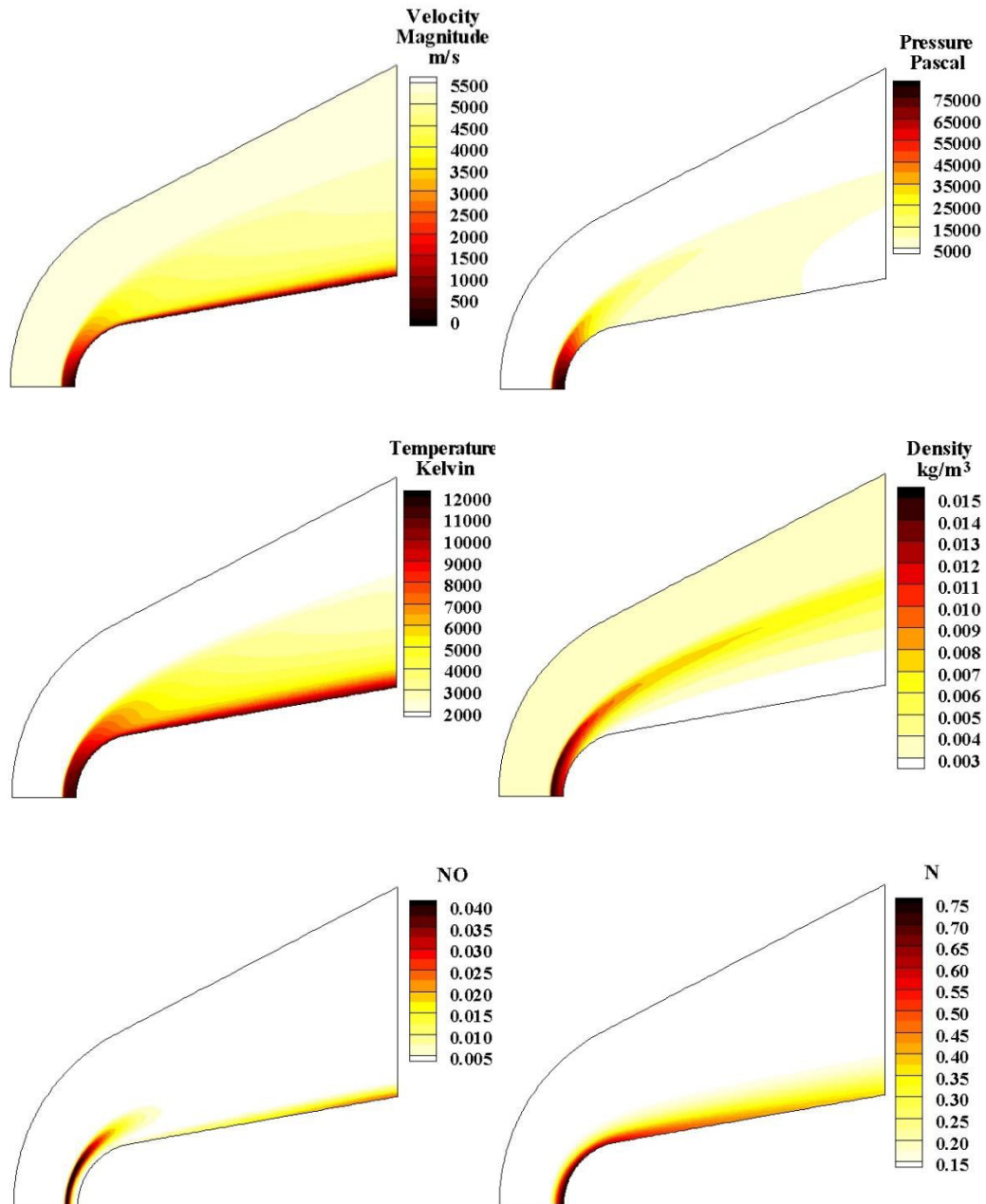


Figure 4.3. Numerical Results Using 96x52 Grid

4.2. Ablation Analysis Results

In this section, the accuracies of the decoupled and coupled models are examined with the test case explained in Section 4.1. The residual histories of the flow field solution of the coupled analysis are shown in Figure 4.4 for density, energy and z momentum. Besides, the residuals for wall temperature and mass blowing rate of the stagnation point are given in Figure 4.5. One can realize that, the history plots are divided in three sections. In the first 5000 iterations the analysis is carried on for frozen flow field with non-reactive wall boundary condition. In the second part the ablation solution is activated without flow field reactions. Finally the gas phase reactions are activated and the calculations are continued until all the normalized residuals reach to the value of 10^{-10} . It takes about 135000 Euler iterations for the convergence of the conjugate computation.

The boundary layer edge properties which are extracted from the aerothermodynamics calculation results of Section 4.1 are used for the decoupled analysis study. In Figure 4.6, the comparison of the computed wall temperature values with experimental and numerical results from literature [20, 23] is given. Computational results adapted from reference [23] belong to a fully coupled analysis study with wall equilibrium assumption. Highly accurate results are obtained near the stagnation point if the coupled approach is used. Although decoupled analysis overestimates the wall temperature, the difference between the experiment and decoupled results is still less than 4 % on the stagnation point. Discrepancy between the experimental and the numerical results increases with the increasing distance from the stagnation point since the equilibrium assumption begins to fail for temperature levels below 2500 K [23].

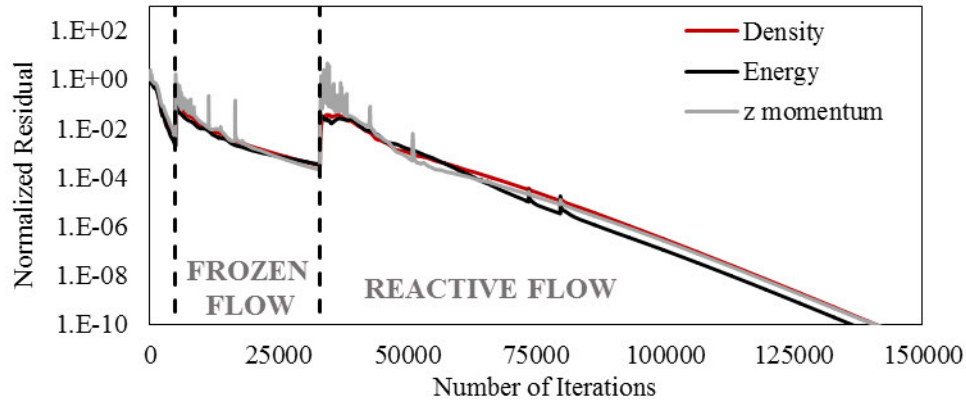


Figure 4.4. Residual Histories inside the Flow Field (Coupled Analysis)

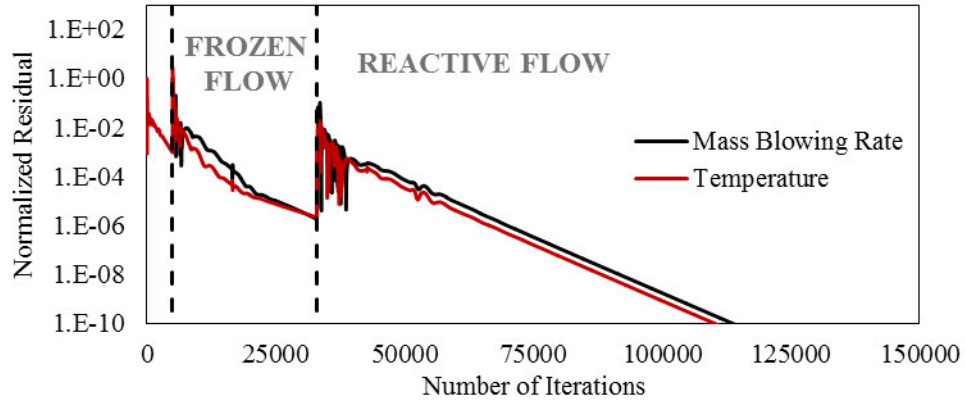


Figure 4.5. Residual Histories of Mass Blowing Rate and Wall Temperature on the Stagnation Point (Coupled Analysis)

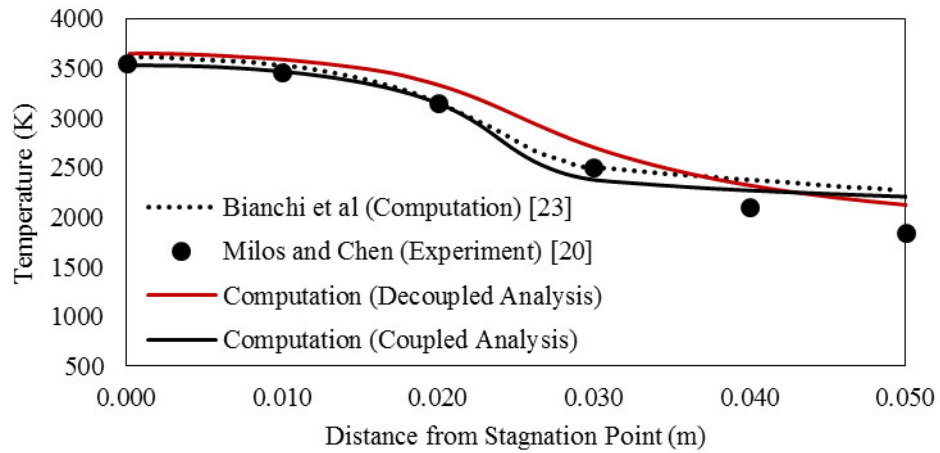


Figure 4.6. Comparison of Calculated Wall Temperature Distributions with References [20, 23]

Comparison of temperature contours inside the solid domain is shown in Figure 4.7. Zero heat flux boundary condition is implemented on the symmetry line and the back wall for the solid conduction problem. Difference in the trends of the computed wall temperature distributions is clearly reflected to the contour shapes.

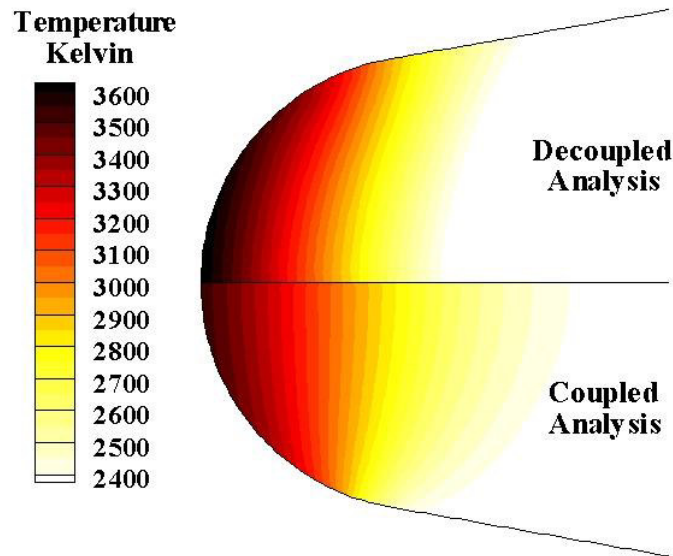


Figure 4.7. Temperature Distributions inside the Solid Domain

In Figure 4.8, computed mass blowing rate values are compared with the measurements [20] and computational results [22, 23] from the literature. In the results of conjugate analysis, 10 % overestimation and 13 % underestimation are observed on the stagnation and 45° angle points of the spherical nose, respectively. If a decoupled calculation is carried on, the mass blowing rate is calculated 25 % and 30 % higher than the measurements on the similar points.

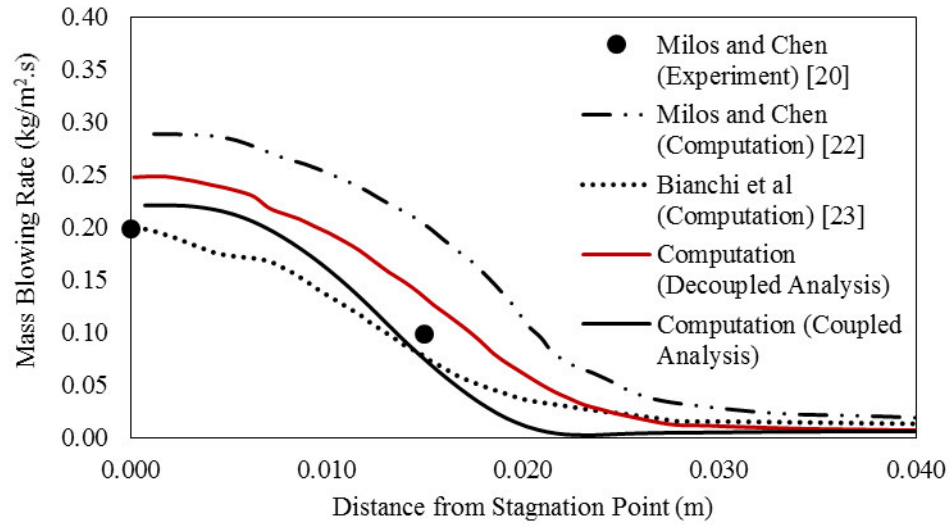


Figure 4.8. Comparison of Calculated Mass Blowing Rate Distributions with References [20, 22, 23]

Close-up views of the temperature contours which are obtained using adiabatic and ablative boundary conditions are compared in Figure 4.9. The thin cool layer of the ablation products around the vehicle nose is clearly distinguishable in the contours of the conjugate analysis. The gas density near the wall is increased due to this cooling effect of ablation and a slight change of the shock stand-off distance is observed.

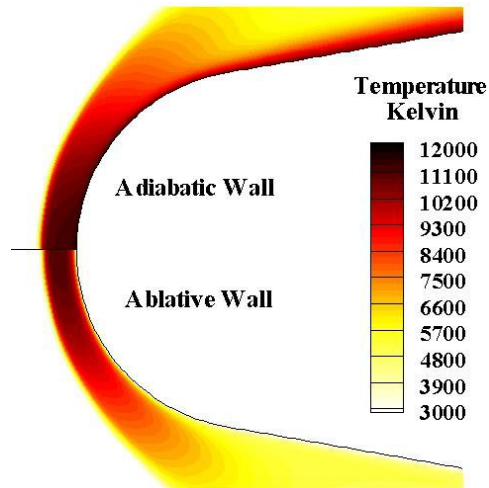


Figure 4.9. Temperature Distributions inside the Flow Field

C_3 and CO are the products of sublimation and oxidation reactions respectively and the mass fraction contours of these two dominant species are given in Figure 4.10. Increase of the sublimation rates is expected with increasing temperature and decreasing pressure. On the other hand, the effect of the temperature is more dominant. The B' curves given in Figure 3.8 can be considered as illustrative examples to this effect. High temperature values result in the steep changes of the B' (nondimensional mass blowing parameter) due to the increase of the sublimation. Thus, the highest C_3 mass fraction is seen near the stagnation point with a maximum value of 0.136 despite the high pressure on this point. Contrary to C_3 , the rate of CO injected to the boundary layer increases with increasing distance from the stagnation point. The mass fraction of CO varies between 0.3 and 0.38 on the ablating wall through streamwise direction.

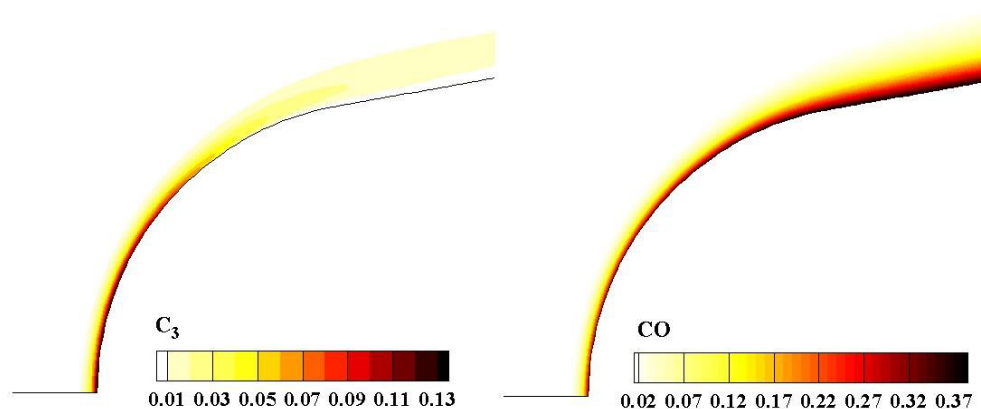


Figure 4.10. Mass Fraction Distributions of C_3 and CO inside the Flow Field (Coupled Analysis)

Figure 4.11 shows the variation of the species mass fractions inside the boundary layer through the stagnation line. Continuous increase of ablation products and severe decrease of O, NO and N are observed while approaching to the wall. On the other hand, N_2 initially decreases and begins to increase again with the decreasing distance from the stagnation point. In the numerical simulations, cooling of the wall causes the N atoms to recombine.

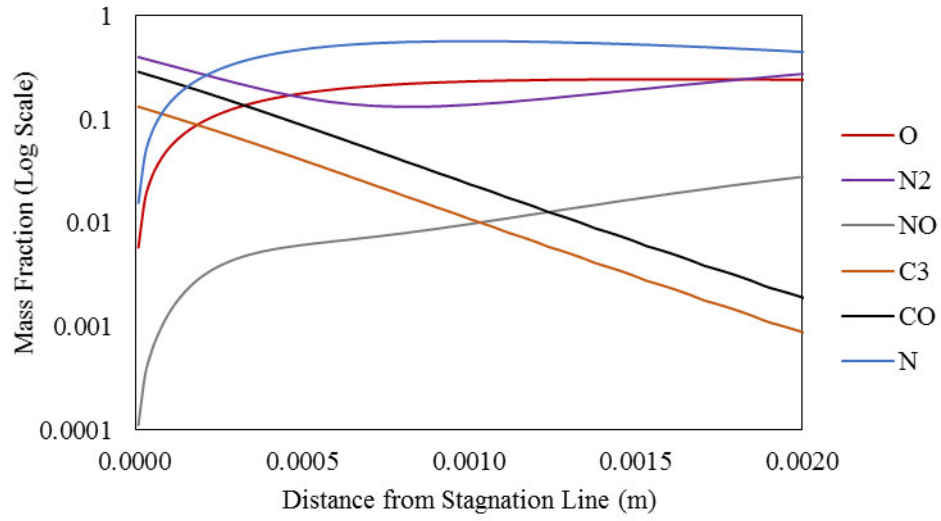


Figure 4.11. Mass Fraction Distributions along the Stagnation Line (Coupled Analysis)

4.3. Ablation Analysis of a Drag Optimized Nose-Tip Geometry

The steady state temperature distributions and ablation behaviors of two nose-tips are compared using both coupled and decoupled analyses. The first geometry is similar to the test specimen used by Milos and Chen [20] and the ablation analysis results of this nose-tip are already presented in the Section 4.2. This shape is named as “nose-tip A” in the rest of the text. In the study of Onay and Eyi [59], a gradient based optimization is conducted using the nose-tip A as the baseline geometry. Adjoint method and Bezier curves are used and the total drag is reduced about 16 % without increasing the stagnation temperature. The optimized geometry has a flat nose followed by two shoulders and a concave curve in between. The views of two geometries are given in Figure 4.12 and the optimized one is named as “nose-tip B”.

The flow field analysis results for nose-tip B are given in Figure 4.13. 96x52 structured cells are used and the view of the grid can be seen in Appendix B. Similar initial cell distance and boundary layer settings are used with the grid of nose-tip A.

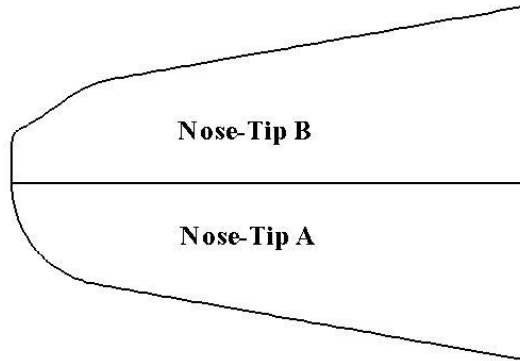


Figure 4.12. Nose-Tip Geometries

Comparison of computed mass blowing rates and wall temperatures are given in Figure 4.14 (a) and (b) using decoupled and coupled approaches, respectively. A peak in the calculated ablation rate is observed on the first shoulder of the nose-tip B following the flat nose. This peak points are almost on the similar locations in the solution results of the both analyses. A similar increase in the mass blowing rate is also seen close to the second shoulder region but the variation is not sharp as the initial one. Maximum mass blowing rates are calculated as $0.29 \text{ kg/m}^2/\text{s}$ using separate solutions of solid and fluid regions and $0.24 \text{ kg/m}^2/\text{s}$ using conjugate analysis of nose-tip B. The peak ablation point is followed by a sudden decrease due to the decrease in the temperature and the temperature variation is steeper in the coupled analysis results. The maximum temperatures are on the stagnation points of the vehicle noses and very close for two geometries in the results of the both analyses. Stagnation temperatures are calculated as about 3500 K and 3640 K in the coupled and decoupled calculation results, respectively. Close-up views of the mass fraction distributions of C_3 and CO are given in Figure 4.15 around the nose-tip B. A severe reduction of C_3 production and increase of CO production are observed after the first shoulder region. Contour plots show that, decrease of the sublimation rate is responsible from the sudden decrease of the mass blowing after the peak point which is shown in Figure 4.14. The transition of the ablation regime from sublimation to oxidation on the surface of nose-tip B is estimated to be much sharper by the conjugate analysis.

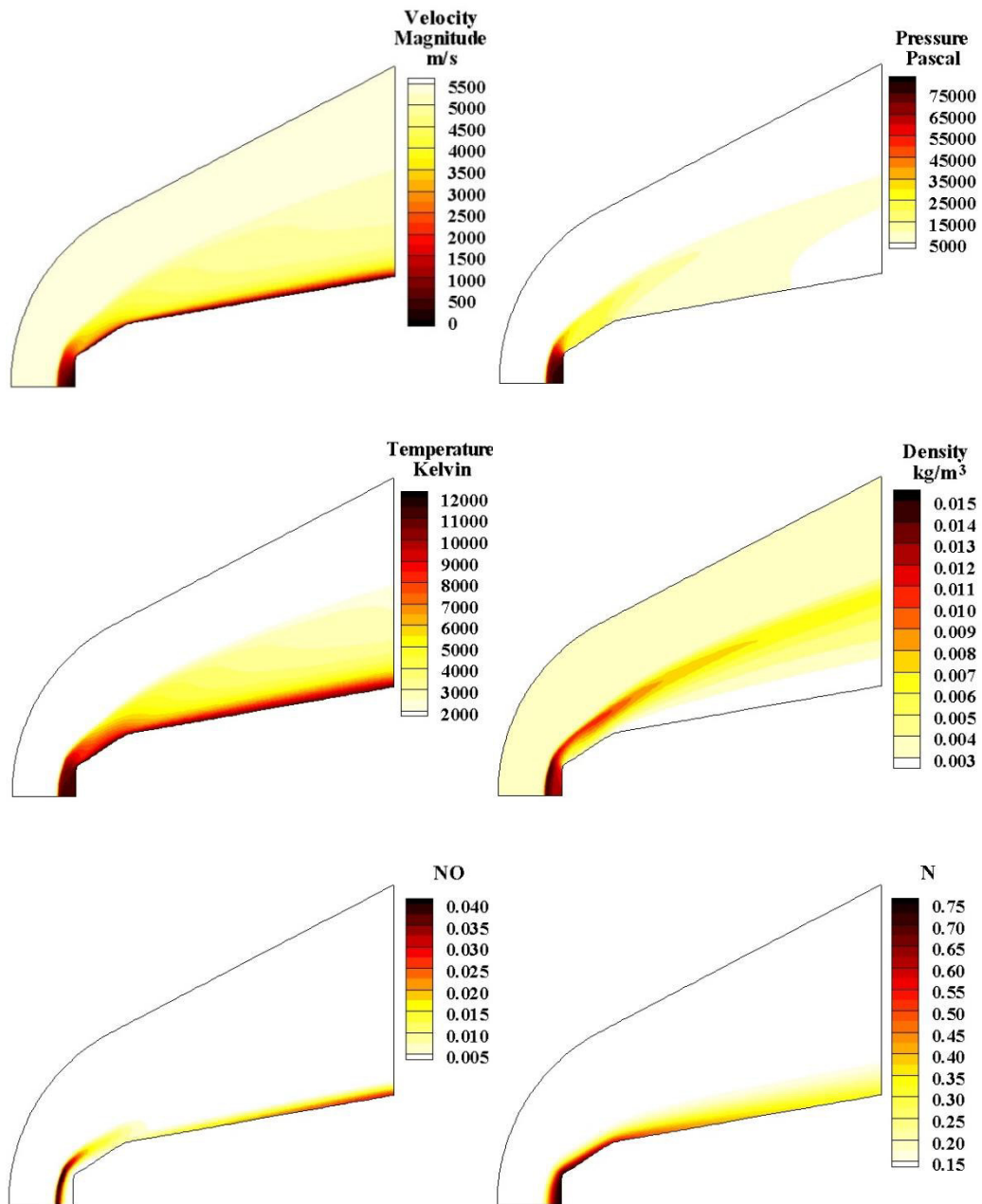
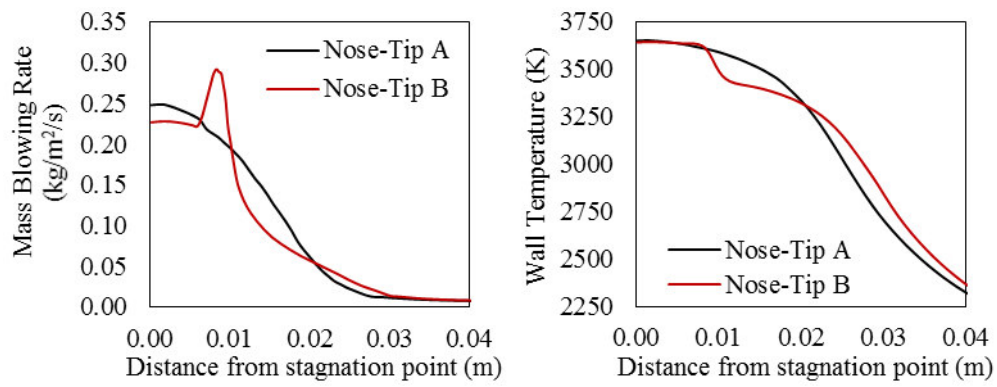


Figure 4.13. Numerical Results Using 96x52 Grid - Nose-Tip B (Adiabatic Wall)



(a)

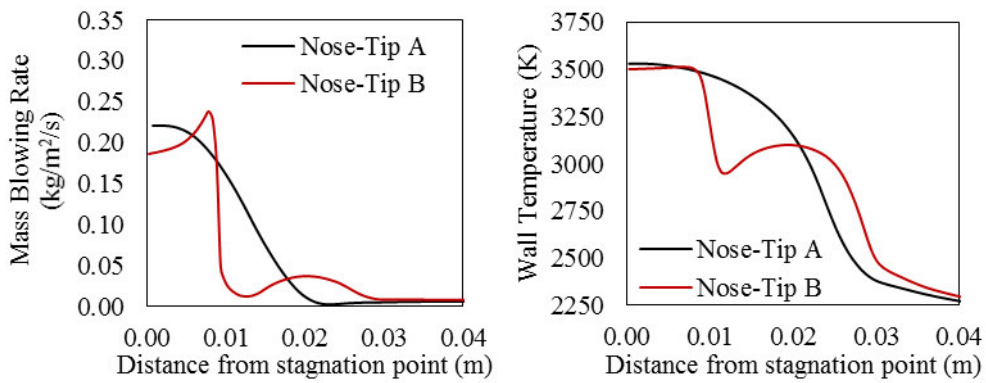


Figure 4.14. Comparison of Mass Blowing Rate and Wall Temperature Distributions - (a) Decoupled Analysis (b) Coupled Analysis

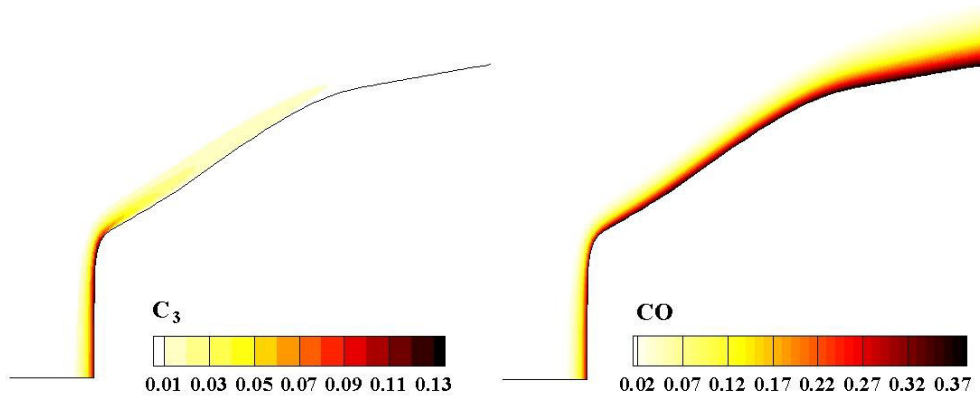


Figure 4.15. Mass Fraction Distributions of C_3 and CO inside the Flow Field - Nose-Tip B (Coupled Analysis)

Temperature and pressure contours around the nose-tips A and B are presented in Figure 4.16. The shock stand-off distance of the nose-tip B is remarkably higher and the cool layer of ablation gasses is relatively thicker after the initial shoulder of the geometry. Besides, a sudden expansion region begins just after this region. These phenomena explain the ablation peak which is followed by the severe decrease on the wall of the nose-tip B. The decrease of the pressure enhances the sublimation rate. By the way, the distance of the hot gas stream from the ablating wall increases beginning from the shoulder due to the concaveness of the geometry. Thus, the increase of the sublimation rate is suppressed by the sharp decrease of the wall temperature. In Figure 4.17; mass blowing rate, wall temperature mass fractions of dominant ablation products, convective heat flux and pressure distributions are given together with the shapes of the nose-tips. These plots show the exact locations of the variations on the ablating geometries. Mass blowing rates are integrated over the surfaces and total mass removal rates are calculated as 1.27×10^{-4} kg/s and 1.06×10^{-4} kg/s for nose tip A and B, respectively.

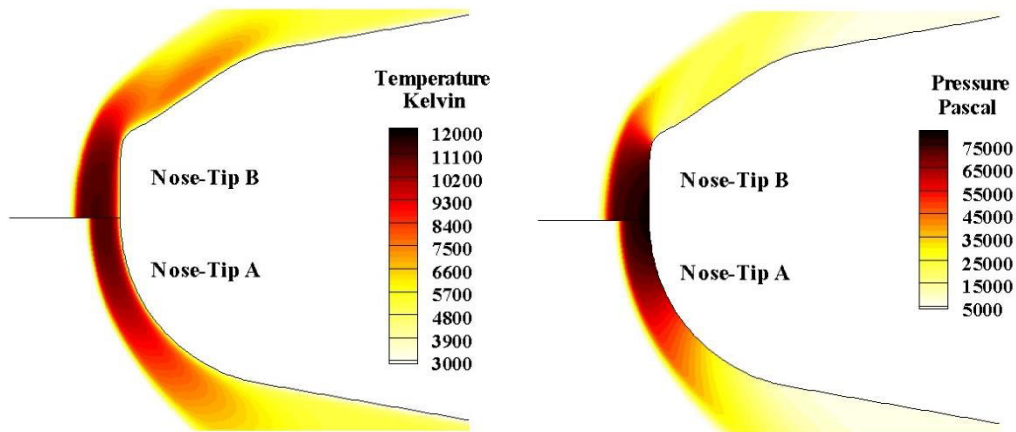


Figure 4.16. Temperature and Pressure Contours Around the Nose-tips A and B

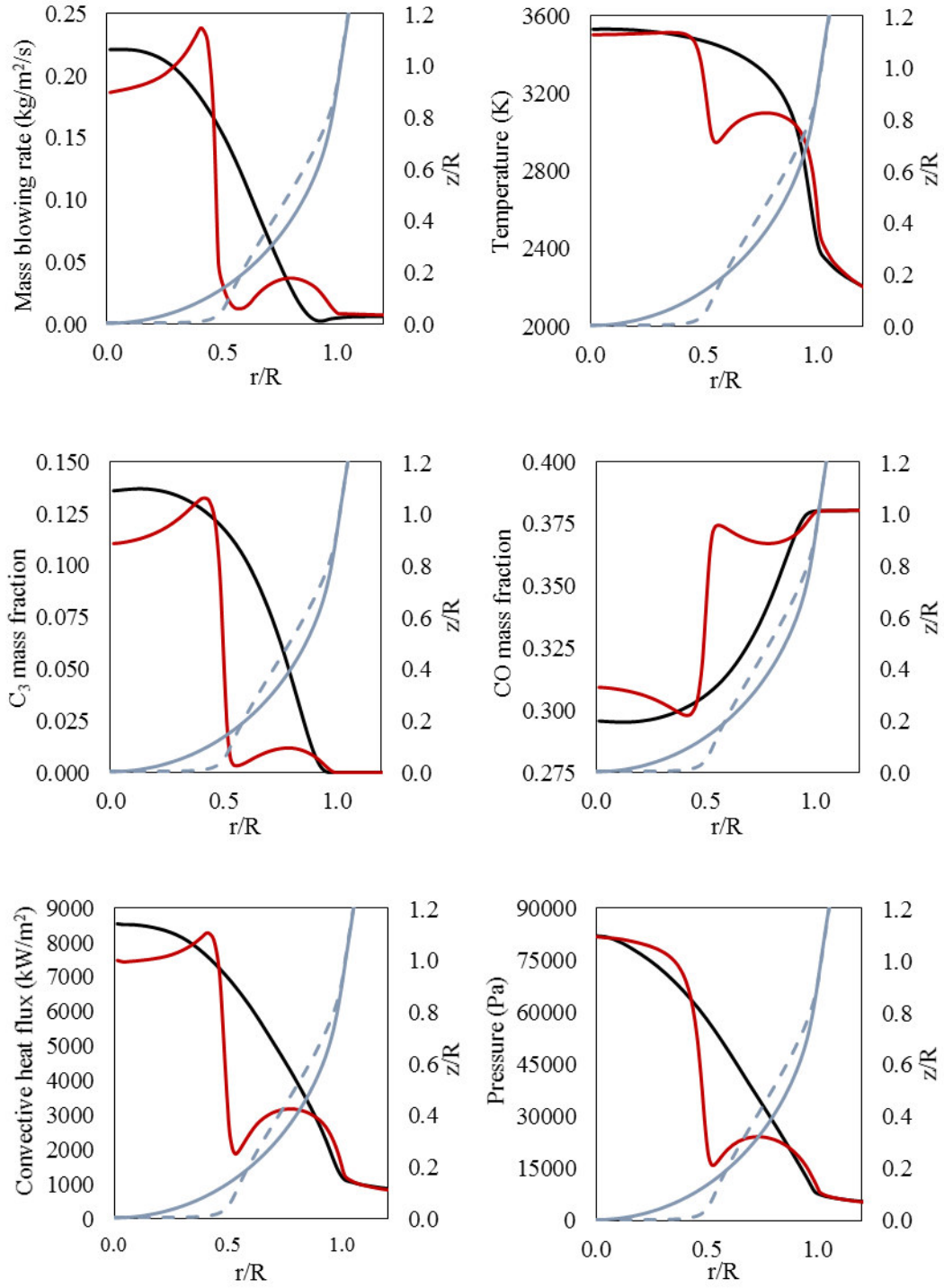


Figure 4.17. Comparison of Ablation Analysis Results (Solid Black Lines: Nose-Tip A Results, Solid Red Lines: Nose-Tip B Results, Solid Grey lines: Geometry of Nose-Tip A, Dashed Grey Lines: Geometry of Nose-Tip B)

Computed temperature contours inside the solid domains of the two nose-tips are compared in Figure 4.18. The effect of the surface temperature decrease after the sharp shoulder can be observed on the contours of Nose-tip B which are obtained with conjugate analysis. This detail does not exist in the results of decoupled calculations since the effects of the ablation inside the boundary layer are not resolved. Using the boundary layer edge properties without a detailed boundary layer analysis is prone to lumped results and negligence of the effects of the geometrical variations.

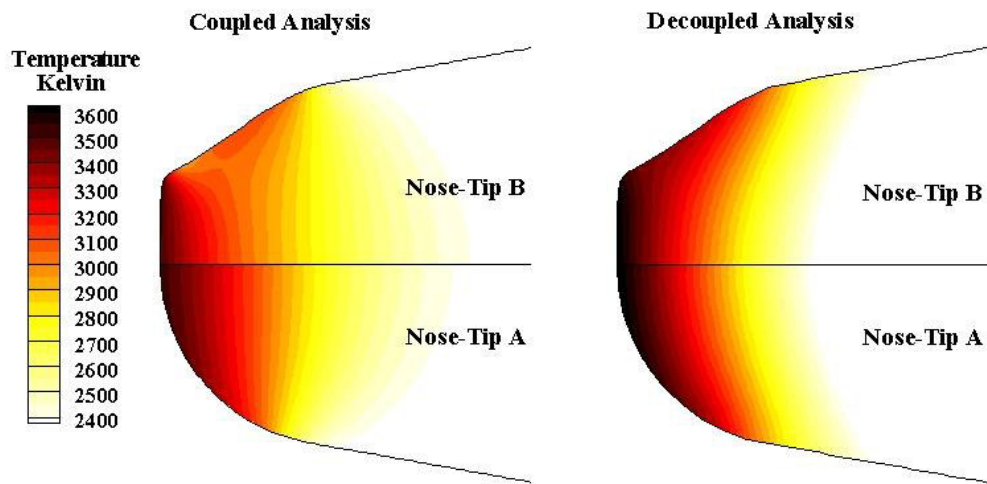


Figure 4.18. Comparison of Temperature Distributions inside the Solid Domains

4.4. Discussions on External Flow Solution Results

In Chapter 4, success of the fully coupled and decoupled analysis models are tested for a graphite specimen which is exposed to energetic arc-jet gas stream. Also, models are used for the ablation analysis of a drag optimized nose-tip with an unconventional geometry.

Higher accuracy is obtained in ablation rate and wall temperature computations using the conjugate approach. On the other hand, decoupled analysis model is a fast tool and the accuracy level of the results are acceptable for purposes like preliminary design

studies. The heat transfer coefficient approximation which is used in the decoupled analysis considers the effect of geometrical variations. But, the analysis results of the drag optimized geometry show that, using a coefficient approximation is not enough for detailed resolution of ablation and wall temperature distributions for steep geometrical variations. Detailed analysis inside the boundary layer with coupled analysis is more effective in terms of understanding the ablation behaviors of nose-tips. It is possible to increase the accuracy of the decoupled analysis tool via optimizing the approximation coefficients with the help of experiments. On the other hand, such a tuning study will not be helpful in terms of avoiding lumped results over the geometrical variations.

CHAPTER 5

EROSION MODELING RESULTS FOR SRM NOZZLE THROATS

5.1. Comparison of Equilibrium and Finite Rate Models using Decoupled Analysis

In the current validation study, the experiments which are conducted by Geisler [46] are selected for the comparison of the recession rate measurements with the numerical results. Previously, these experiment results are also used by Thakre and Yang [7] and Bianchi et al [8, 9] in order to test their numerical models. The length of the nozzle insert of the test motor is 30 cm and the throat radius is 2.54 cm. In the firing tests, 5 different AP/HTPB propellants are used with 15%, 18%, 21%, 24% and 27% aluminum contents. 3 of these firings are selected in the current study and the nozzle inlet conditions are given in Table 5.1. Increased aluminum content, decreases the mass fractions of the oxidizers CO_2 and H_2O while increasing the mixture temperature as seen in the table.

Table 5.1. Nozzle Inlet Conditions of the Test Cases [46]

Al %	y_{CO}	y_{CO_2}	y_{HCl}	y_{H_2}	$y_{\text{H}_2\text{O}}$	y_{N_2}	$y_{\text{Al}_2\text{O}_3}$	$P \times 10^{-5}$ (Pa)	T (K)
15	0.175	0.04	0.24	0.02	0.145	0.1	0.28	69	3580
21	0.2	0.015	0.195	0.02	0.07	0.1	0.4	69	3715
27	0.2	0.005	0.19	0.02	0.025	0.1	0.46	69	3745

Axisymmetric CFD analyses are conducted assuming that the mixture inside the flow field is in single phase and frozen. Adiabatic wall boundary condition is implemented. CFD analyses are performed once for each of the propellants and similar boundary layer edge results are used for the ablation analyses with wall equilibrium and finite

rate assumptions. Temperature, Mach, density and pressure contours of the flow field solution are given in Figure 5.1 for 15 % aluminized case as example.

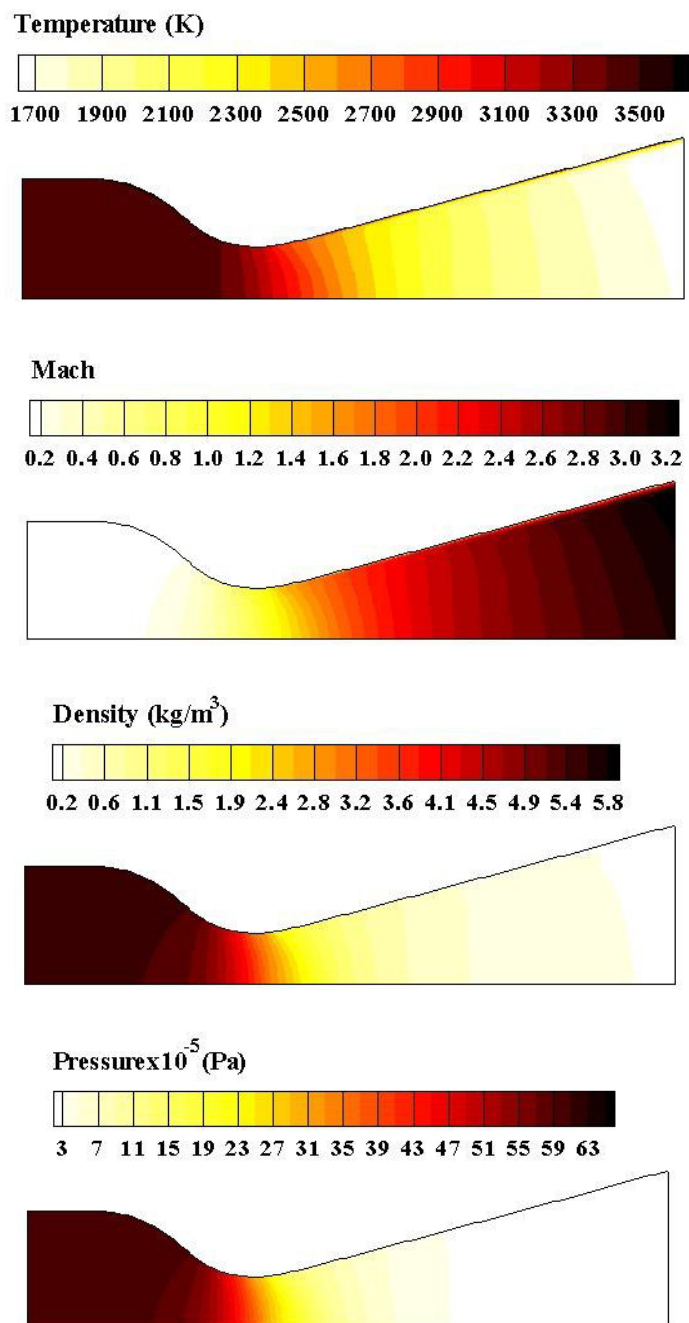


Figure 5.1. Numerical Results for 15 % Aluminized Propellant (Adiabatic Wall, Frozen Flow)

In Figure 5.2, erosion rate distributions through the graphite wall are given together with the measurements on the throat location. Besides, computed throat temperatures and erosion rates are compared in Table 5.2. The highest difference between the calculated recession rates for wall equilibrium and finite rate methods is seen for 15 % aluminized propellant case. The measurement is 0.353 mm/s and the computational error is 11 % for the equilibrium method. In this approach, surface reaction rates are assumed to be fast enough and the erosion rate is controlled by the diffusion of reactants from boundary layer to the eroding wall. The discrepancy shows that, the ablation is not totally controlled by the diffusion and the reaction rates have a partial effect on the phenomenon for the 15 % aluminized nozzle inlet condition. The numerical error is less than or in the order of 10 % for the rest of the calculations and the recession rate results of equilibrium and finite rate computations are highly coherent with each other for the 27 % aluminized propellant.

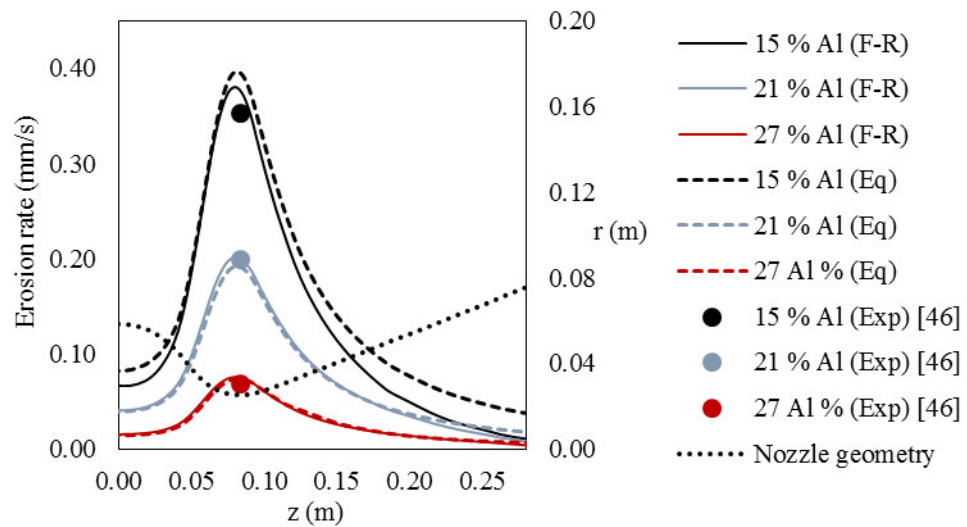


Figure 5.2. Comparison of Computed Erosion Rate Values with Experiment from [46] (Decoupled Analysis)

Table 5.2. Computed Temperature and Erosion Rate Values on the Throat

Method	15 % Al		21 % Al		27 % Al	
	T (K)	\dot{s} (mm/s)	T (K)	\dot{s} (mm/s)	T (K)	\dot{s} (mm/s)
F-R	2734	0.375	3147	0.202	3391	0.075
Eq	2738	0.393	3183	0.189	3430	0.074

Decoupled analysis method with wall equilibrium assumption is not an appropriate approach for transient heating problems. On the throat point, equilibrium state may not be reached until the end of the firings if the nozzle inlet temperature is low and/or firing durations are relatively short. In the early stages of the firings, the wall temperatures are too low for the initiation of heterogeneous reactions and the assumption of infinitely fast surface reaction rates would yield an overestimation of recession rates with decreased wall temperatures due to excessive material removal. On the other hand, reaction rate controlled time periods of the erosion phenomenon can be resolved using the finite rate model. In Figure 5.3 and Figure 5.4, time variations of calculated recession rates and total recessions are given for the throat point. It takes about 4 and 1.25 s for the recession rate values to reach the steady state for 21 % and 27 % Al propellants, respectively. On the other hand, variation of the computed value continues even at the end of 10 s of firing duration for 15 % Al propellant.

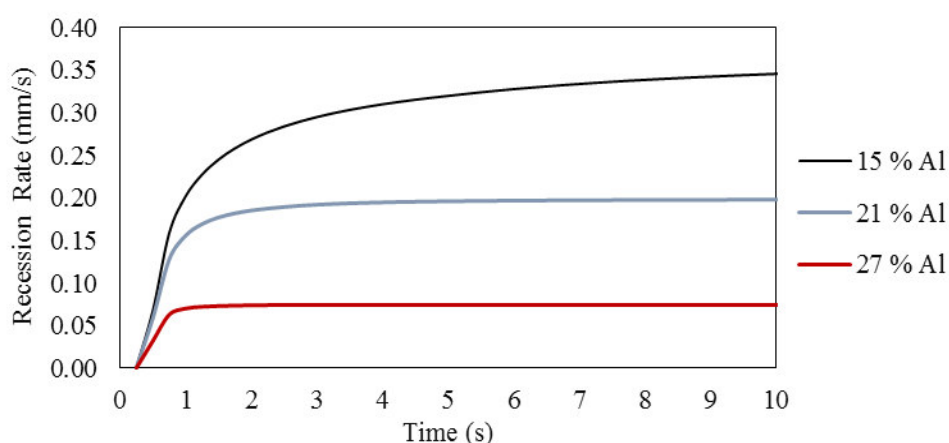


Figure 5.3. Variation of Erosion Rate with Time (Finite Rate, Decoupled Analysis)

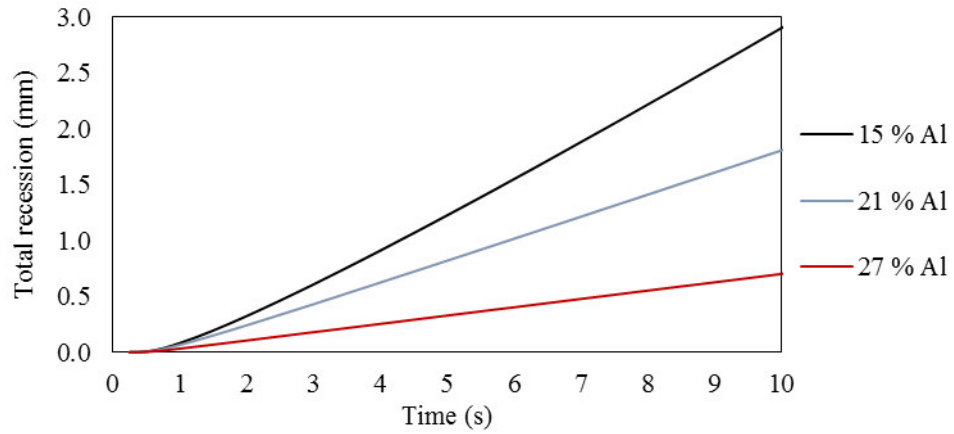


Figure 5.4. Variation of Total Recession with Time (Finite Rate, Decoupled Analysis)

The contours of temperature inside the graphite domain are given in Figure 5.5 for 15 % aluminized propellant at various instants. The maximum temperature is seen on the throat location during the solid heating since the approximated heat transfer coefficient is inversely proportional with the cross section diameter in the correlation of Bartz [3].

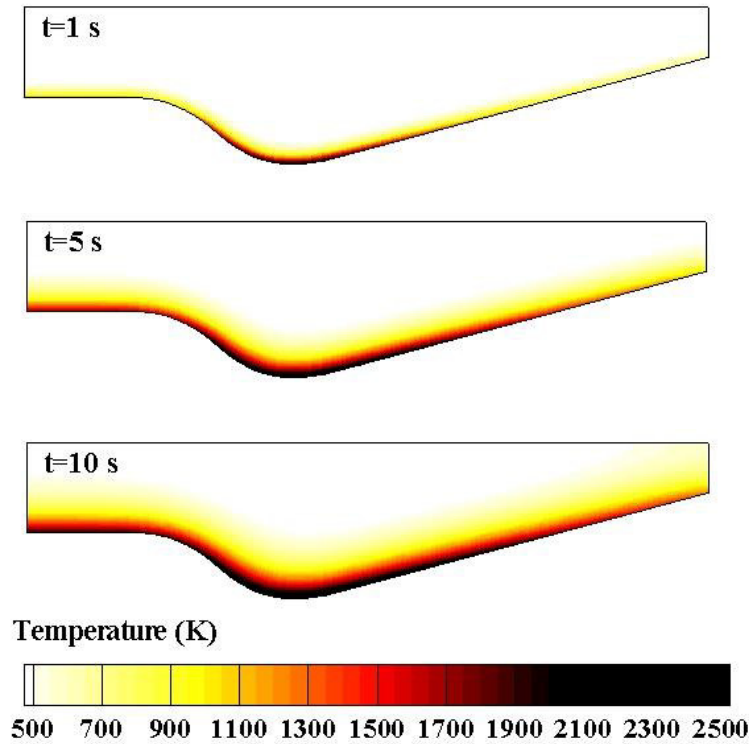


Figure 5.5. Temperature Contours inside the Solid Domain at $t = 1, 5$ and 10 s for 15 % Aluminized Propellant (Finite Rate Surface Thermochemistry, Decoupled Analysis)

5.2. Time Accuracy Check for the Decoupled Model

A transient analysis is conducted for the throat erosion of a short firing duration test motor. The decoupled analysis method is used in order to decrease the computational cost. In the early stages of the firings, the recession rate has a variation in time and the recession of the throats are usually not linear. Besides, during the wall heating before reaching the steady state, it is not expected for the gas composition to be in equilibrium state since the temperature levels are relatively low. Thus, finite rate surface thermochemistry approach is used for the analysis.

The post-firing measurement results of two tests are used for the comparisons. Test motor of ROKETSAN is used for the experiments with similar metallized propellants under same environmental conditions. Total recessions on the final narrowest points

are measured as 0.275 and 0.290 mm. The firing durations are about 2 s. The view of the simplified model which is used for the numerical analysis is shown in Figure 5.6. The solid region of the model consists of two different materials which are stainless steel and pure graphite. Variable thermal properties are used for both of the materials. The ablation rate is set to 0 on the walls of the stainless steel during the material heating analysis. Radiative and convective cooling boundary conditions are used on the outer walls of the nozzle casing. Heat transfer coefficient and surface emissivity are assumed to be 5 W/m^2 and 1, respectively. The ambient temperature is set to 294 K. 165x50 and 130x60 structured grids are used for fluid and solid sides and the view of the grids are given in Appendix B.

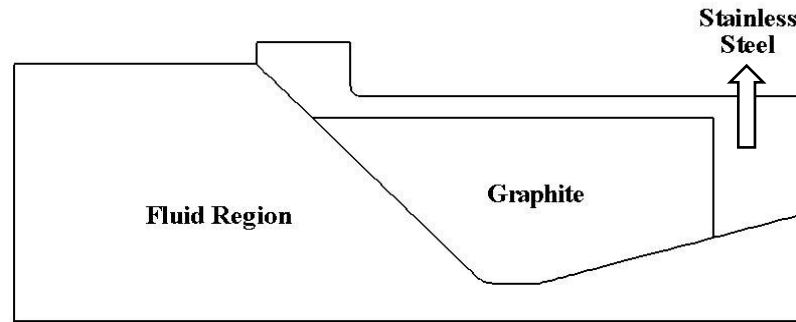


Figure 5.6. View of the Simplified Model of the Test Motor

In Figure 5.7, the variation of the temperature contours inside solid domain is shown at $t=0.5, 1, 1.5$ and 2 s. Also calculated wall temperature distributions are given in Figure 5.8. The maximum wall temperature is computed as 2550 K at the end of the firing. The maximum value takes place near the inlet of the flat throat of the nozzle. After this peak point, the wall temperature begins to decrease and increases again while approaching to the diverging section. At the inlet of the supersonic region, the wall temperature reaches to a local maximum value of 2510 K.

The variation of computed recession rate distributions is shown in Figure 5.9. The increase of the ablation is relatively slow at the converging section since the wall temperature values are not high enough for the increase of the surface reaction rates.

The steady state condition is not reached through the graphite wall. Similar to the temperature distribution, the maximum erosion rate is observed at the throat inlet with a value of 0.294 mm/s at $t = 2$ s. The local maximum value at the inlet of the diverging section is equal to 0.28 mm/s and the minimum value between these two peak points is calculated as 0.265 mm/s. Referring to the ablation profile on the horizontal region of the eroding wall, the final narrowest point of the nozzle is expected in between these two peak points where the local minimum value is observed. The throat shape will not be flat anymore since the corner points will be trimmed due to high ablation rates on the geometrical junction points.

The comparison of the calculated total erosion rate distributions and the post-firing measurements are given in Figure 5.10. Computed total recession of the expected narrowest point is computed as 0.32 mm. The difference of the numerical result with the measurements is 16 % and 10 %, respectively.

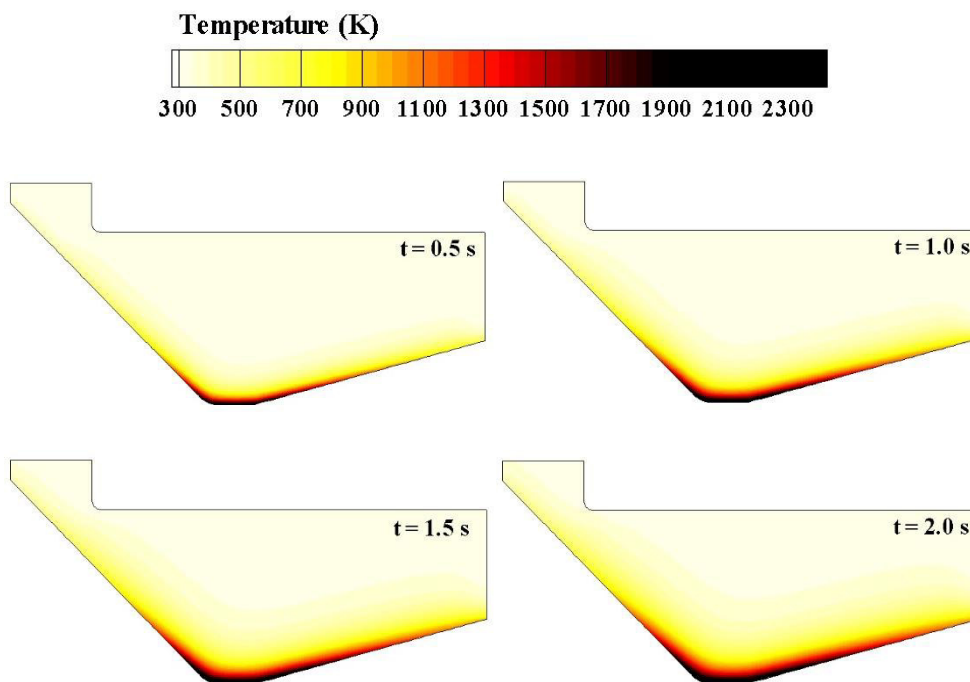


Figure 5.7. Variation of Temperature Contours with Time

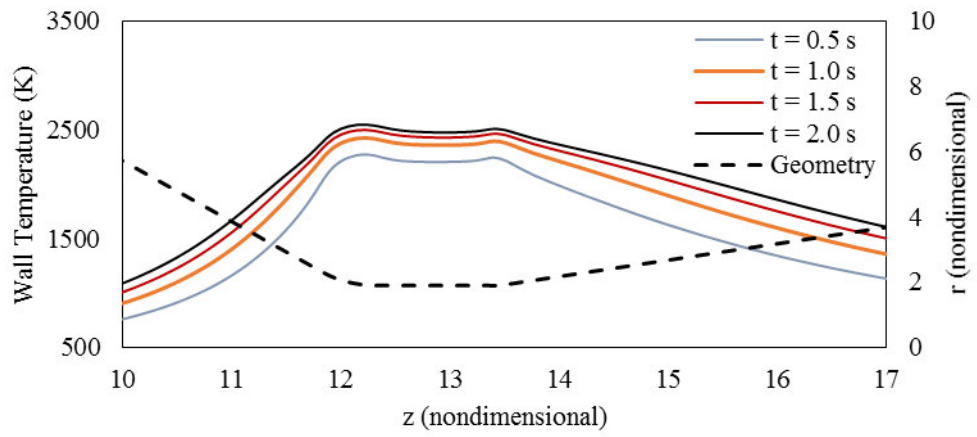


Figure 5.8. Variation of Wall Temperature with Time

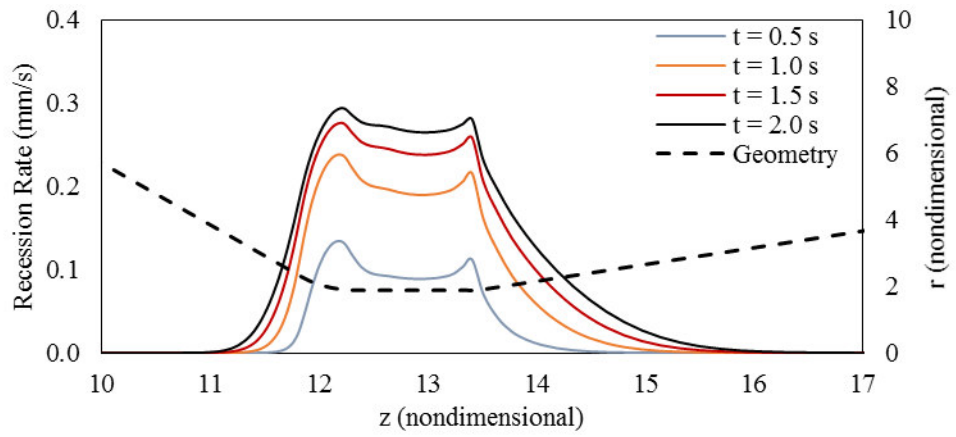


Figure 5.9. Variation of Recession Rate with Time

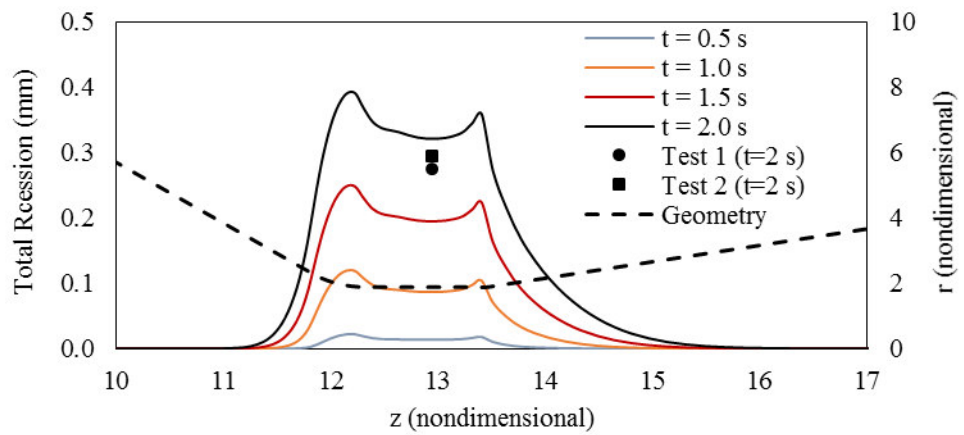


Figure 5.10. Variation of Total Recession with Time and Comparison with Measurement

The solid heating problem which is considered in this section is also analyzed excluding the surface reactions from the numerical solution. In Figure 5.11, the rates of the energy transfer to the solid domain are compared at $t = 2$ s for ablating and nonablating walls. Additionally, the effect of the ablation on the surface temperature can be seen in Figure 5.12. The difference between the distributions of the transferred energy values shows the enthalpy rejection of the material due to ablation. The difference between the maximum points is about 1400 kW/m^2 . Local minimum values of heat transfer rates are observed on the junction points since the difference between the wall and boundary layer edge temperatures are relatively low on these points.

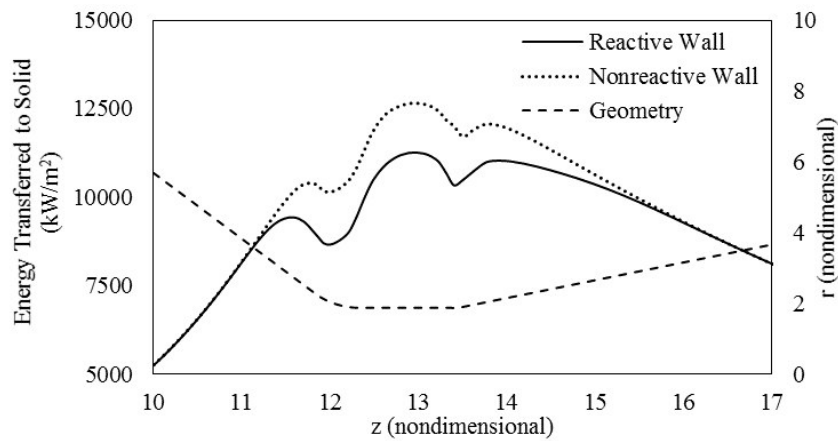


Figure 5.11. Distributions of Energy Transferred to the Solid - Reactive and Nonreactive Walls

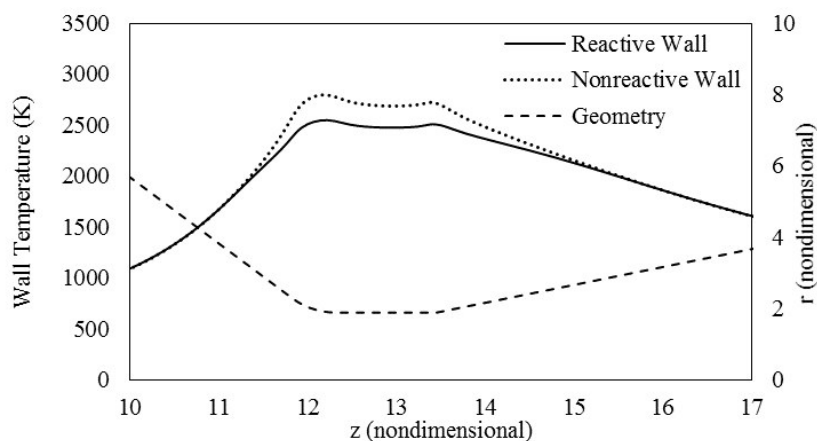


Figure 5.12. Comparison of Wall Temperature Distributions for Reactive and Nonreactive Walls

5.3. Coupled Analysis Results

In the current validation study, coupled model is tested for both metallized and nonmetallized propellants and finite rate surface thermochemistry is used in order to result in a more generalized analysis tool. The firing tests which are conducted by Evans et al. [60] are selected for the comparisons with the numerical results. The nozzle throat diameter is 1.143 cm for the nonmetallized case. The durations of the firing and the optical measurement of the throat enlargement are about 4 and 3.5 s, respectively. According to the optical measurement, the erosion rate reaches to its steady state value of 0.1 mm/s at $t=1.75$ s. The inlet boundary conditions of the nozzle are given in Table 5.3 [7, 60].

Table 5.3. Nozzle Inlet Conditions of the Test Case (Nonmetallized Propellant) [7, 60]

Y_{CO}	Y_{CO_2}	Y_{HCl}	Y_{H_2}	Y_{H_2O}	Y_{N_2}	Y_{OH}	$P \times 10^{-5}$ (Pa)	T (K)
0.11	0.21	0.28	0.01	0.27	0.11	0.01	82.7	3000

The nozzle geometry is reconstructed using the information given in reference [60]. 171x56 and 171x51 structured grids are used for fluid and solid sides, respectively. The views of the grids are shown in Appendix B. Before the coupled computations, the steady state flow field analysis results are obtained with adiabatic wall boundary condition and then the transient heating and ablation of the material is computed using decoupled approach. The temperature contours inside the solid domain are given in Figure 5.13 at $t=1.5$ and 3 s and the flow field solution results for an adiabatic wall are given in Figure 5.14.

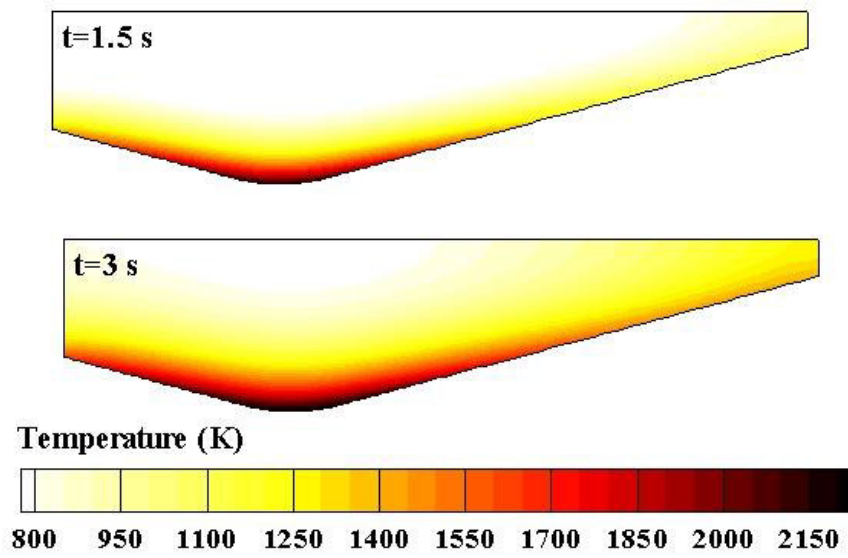


Figure 5.13. Temperature Contours inside the Solid Domain at $t = 1.5$ and 3 s for Nonmetallized Propellant (Finite Rate Surface Thermochemistry, Decoupled Analysis)

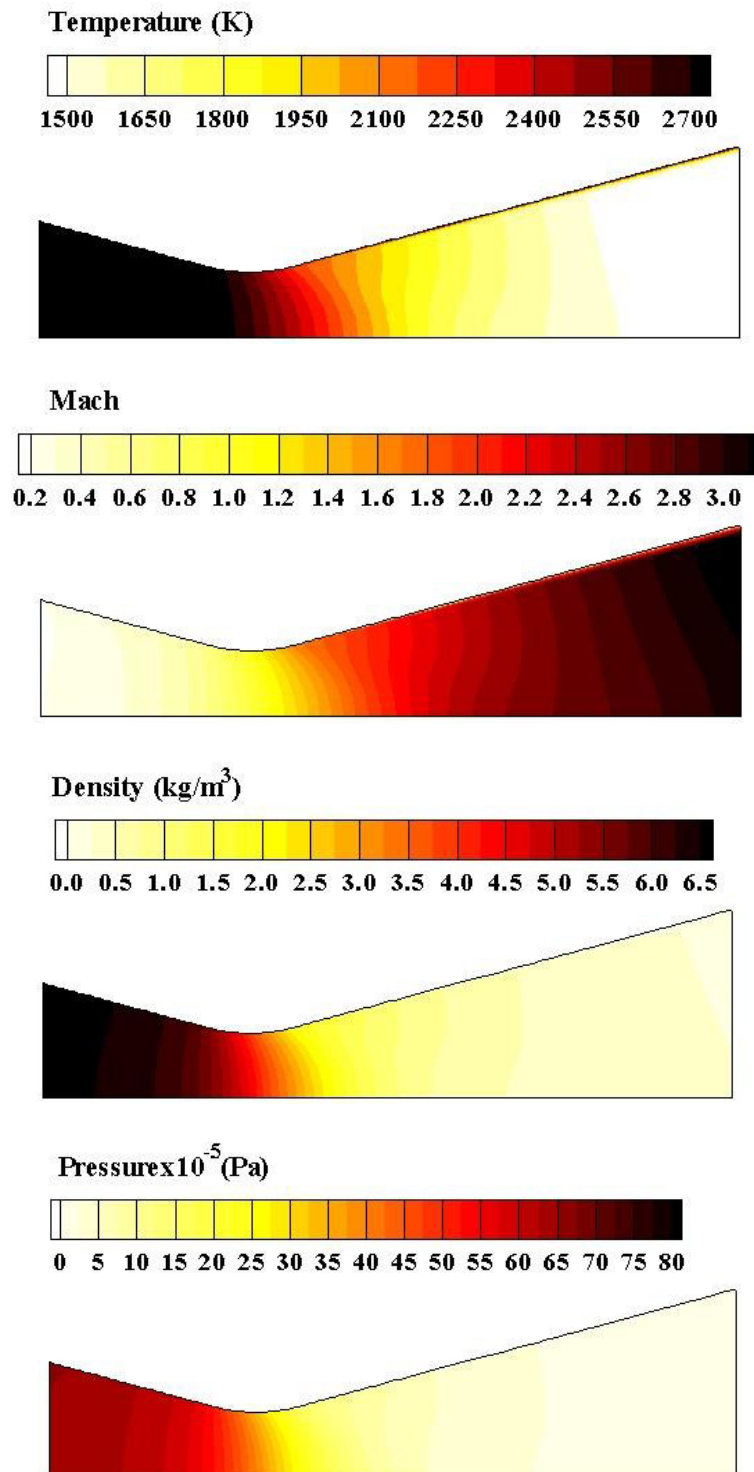


Figure 5.14. Numerical Results Nonmetallized Propellant (Adiabatic Wall, Frozen Flow)

The steady state erosion rate distribution is obtained with fully coupled approach using frozen flow field assumption. The HLLC method is used for the convective flux calculations. Below in Figure 5.15 and Figure 5.16, comparisons of computed erosion rate and wall temperature distributions are given for coupled and decoupled methods. Coupled results are obtained using Spalart-Allmaras turbulence model and Wilke rule. On the throat point, recession rate values are calculated as 0.189 and 0.135 mm/s using decoupled and coupled methods, respectively. The highest erosion rate is calculated on the throat point using the decoupled analysis and about 4.6 mm before the throat using the conjugate analysis. The location of the peak point of the ablation rate is due to the increase of the turbulent viscosity value before the throat in the coupled solution. Increase of the turbulent viscosity results in higher diffusion rates of the oxidizers and the convective heat transfer to the wall. Distribution of turbulent viscosity value inside the nozzle is shown in Figure 5.17.

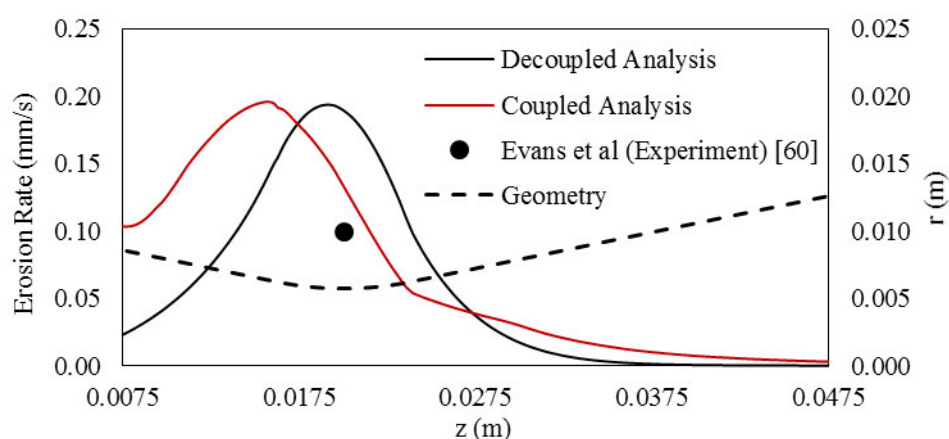


Figure 5.15. Comparison of Calculated Erosion Rate Distributions using Coupled and Decoupled Analyses (Frozen Flow, Spalart-Allmaras Turbulence Model, Nonmetallized Propellant)

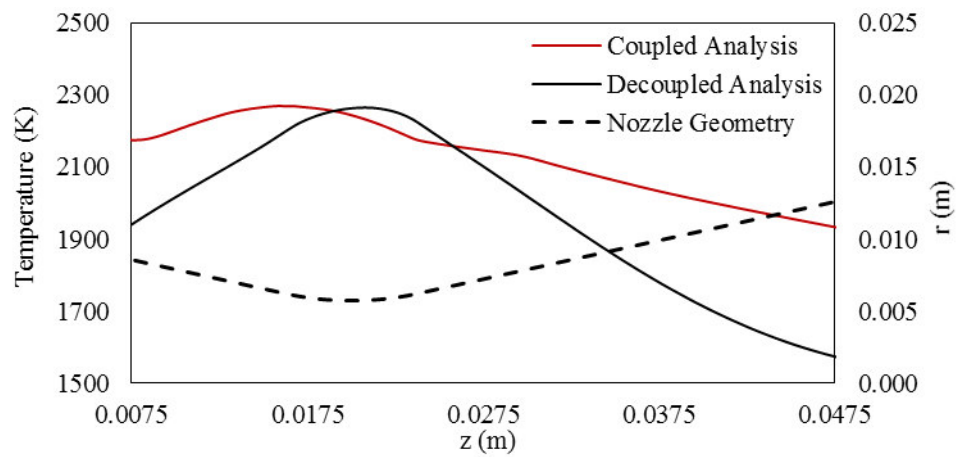


Figure 5.16. Comparison of Calculated Wall Temperature Distributions using Coupled and Decoupled Analysis (Frozen Flow, Spalart-Allmaras Turbulence Model, Nonmetallized Propellant)

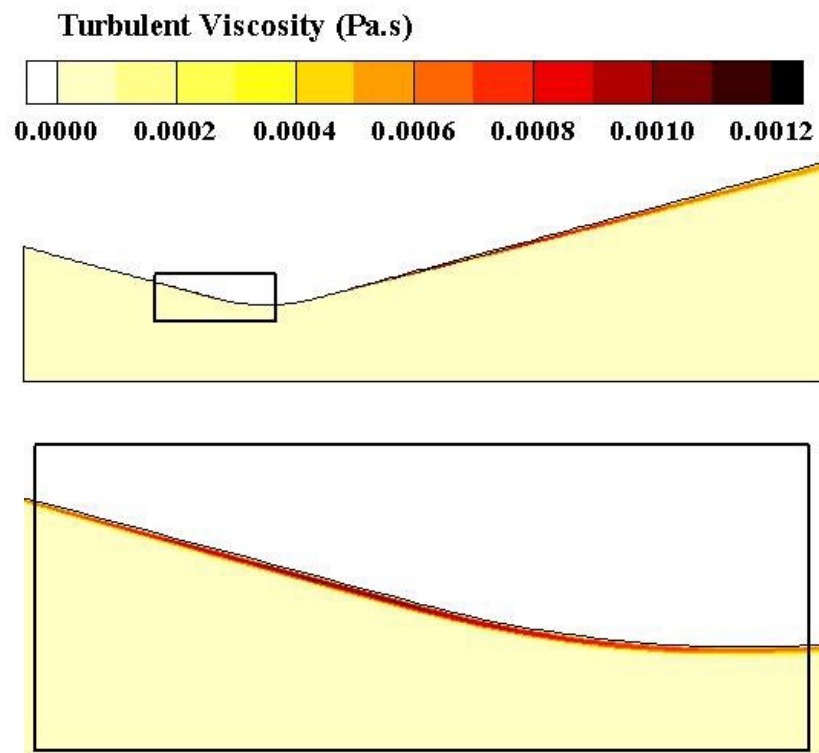


Figure 5.17. Contours of Turbulent Viscosity Ratio (Frozen Flow, Spalart-Allmaras Turbulence Model, Nonmetallized Propellant)

H₂O is the dominant oxidizer of the throat erosion and H₂ and CO are the products of this oxidation reaction. The contours of the temperature and the mass fractions of H₂, CO and H₂O are shown in Figure 5.18. The water vapor is decreased but it is not totally consumed near the wall region since the wall temperature is relatively low. The wall temperature is limited at about 2240 K near the surface due to ablation where the total temperature of the core flow is 3000 K.

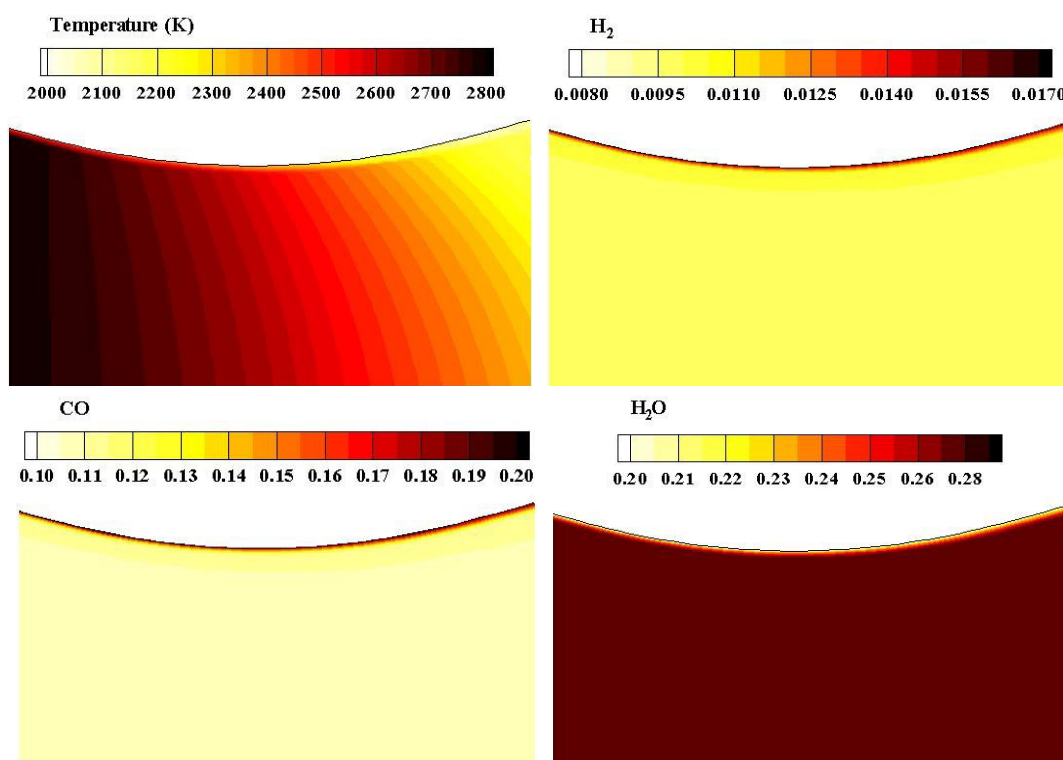


Figure 5.18. Contours of Temperature and H₂, CO and H₂O Mass Fractions near the Throat (Frozen Flow, Spalart-Allmaras Turbulence Model, Nonmetallized Propellant)

Spalart-Allmaras, Baldwin-Lomax and Baldwin-Barth turbulence models are tested using coupled analysis. Total of six computations are carried on via matching the turbulence models with Wilke and Sutherland formulations. Calculated erosion rate values are listed in Table 5.4 for the throat point. The differences of the results for Wilke and Sutherland rules are less than 5% if Baldwin-Lomax or Spalart-Allmaras

models are used. On the other hand, the replacement of the laminar viscosity calculation method has a significant effect on the results of the Baldwin-Barth model. Accordingly, although the numerical result on the throat point seems more accurate with Baldwin-Barth model, this approach results in discontinuous distribution of turbulent viscosity value inside the boundary layer. As an example, the vertical variations of the eddy viscosity values inside the boundary layer are compared in Figure 5.19 at the diverging section. Also close-up views of the eddy viscosity contours inside the boundary layer are shown in Figure 5.20 for solutions with Spalart-Allmaras and Baldwin-Barth models.

The distributions of mass blowing rate and wall temperature values are given for different turbulence models in Figure 5.21 and Figure 5.22. Significant differences between the trends of the results are observed.

Table 5.4. *Comparison of Calculated Erosion Rates on the Throat*

Turbulent Viscosity	Laminar Viscosity	Recession Rate (mm/s)
Baldwin-Lomax	Sutherland	0.141
Baldwin-Barth	Sutherland	0.074
Spalart-Allmaras	Sutherland	0.131
Baldwin-Lomax	Wilke	0.147
Baldwin-Barth	Wilke	0.107
Spalart-Allmaras	Wilke	0.135
Decoupled Analysis		0.189
Experiment		0.100

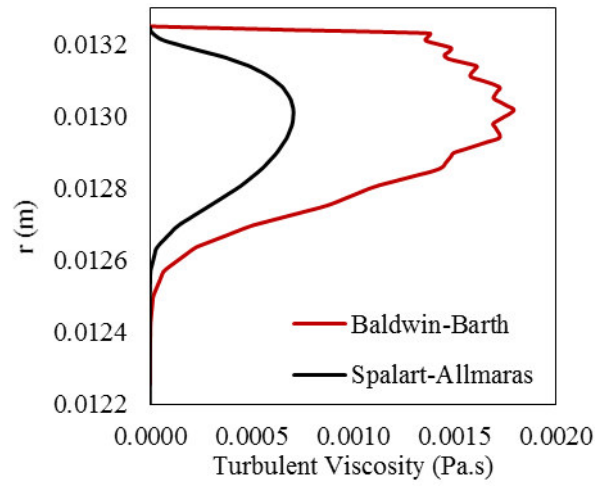


Figure 5.19. Turbulent Viscosity Distributions inside the Boundary Layer (Diverging Section, 0.03 m of Axial Distance from the Throat)

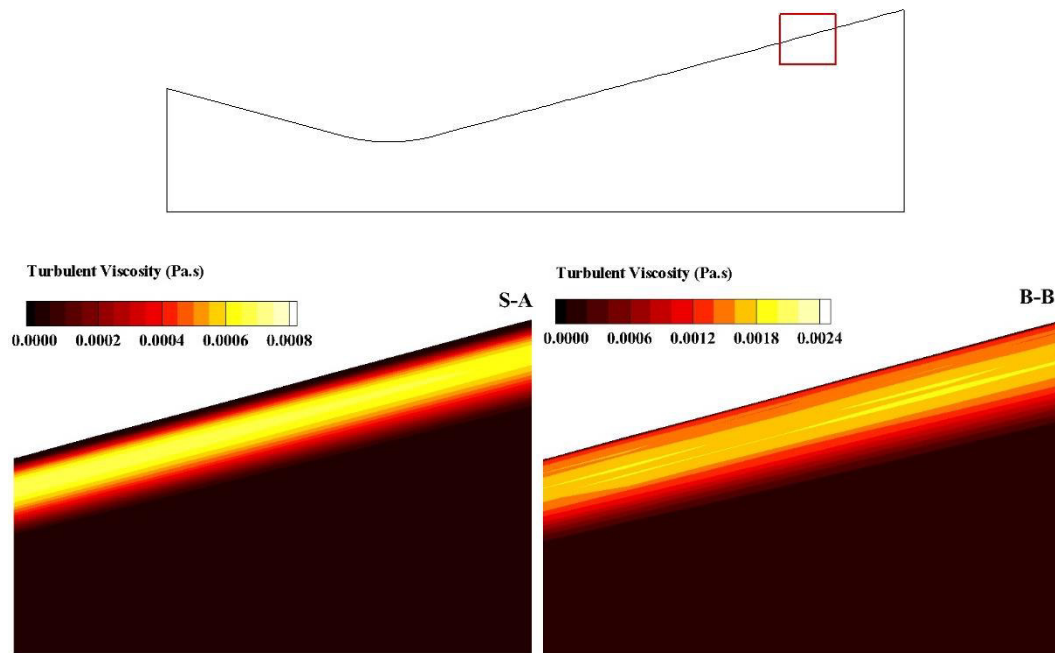


Figure 5.20. Turbulent Viscosity Contours for Spalart-Allmaras and Baldwin-Barth Turbulence Models

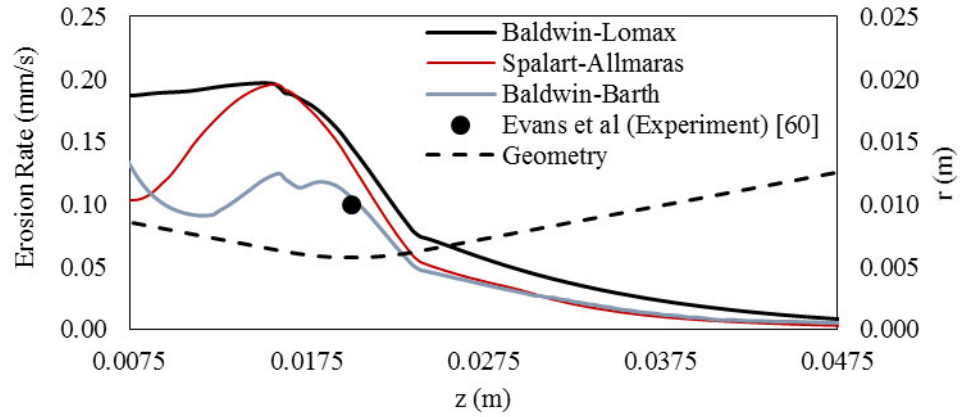


Figure 5.21. Comparison of Calculated Erosion Rate Distributions using Different Turbulence Models (Frozen Flow, Nonmetallized Propellant)

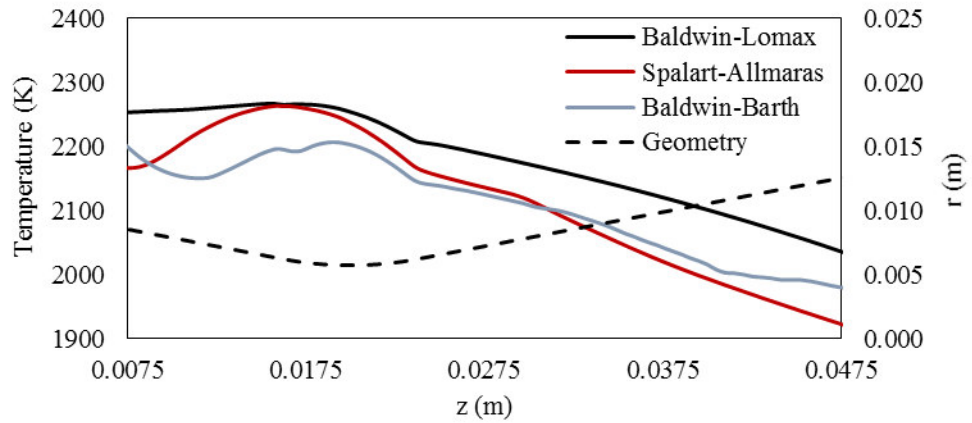


Figure 5.22. Comparison of Calculated Wall Temperature Distributions using Different Turbulence Models (Frozen Flow, Nonmetalized Propellant)

The closure coefficients of turbulence models are usually optimized for nonreactive walls. The ablation computations are sensitive to the turbulence parameters if the ablation phenomenon is relatively slow since the effects of blowing and mass diffusion are comparable near the wall. In order to show the effect of turbulence on the calculation results, distributions of erosion rate and wall temperature are compared for different values of the coefficient c_{b1} which appears in both of the production and

dissipation terms of Spalart-Allmaras model. Computed erosion rate and wall temperature results are compared in Figure 5.23 and Figure 5.24, respectively.

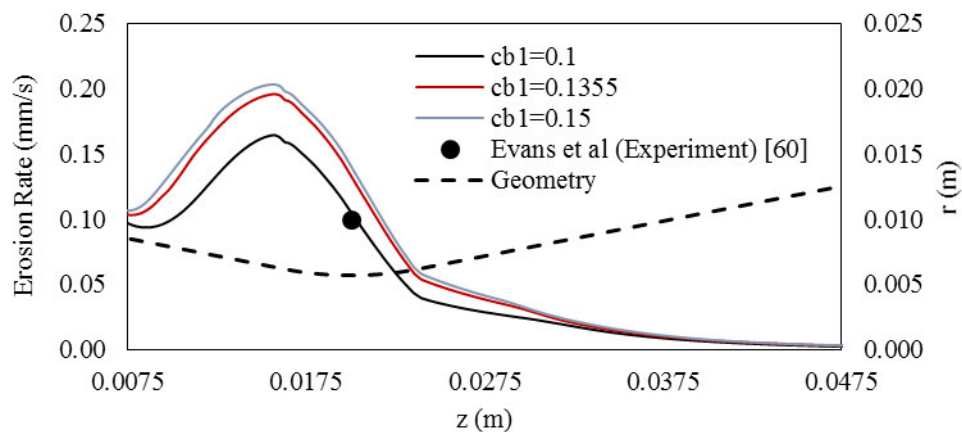


Figure 5.23. Variation of Erosion Rate Distribution with the Closure Coefficient c_{b1}

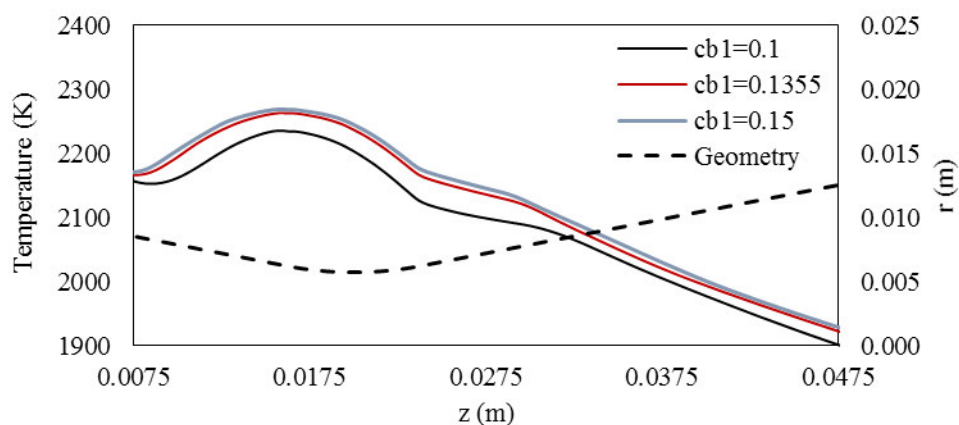


Figure 5.24. Variation of Wall Temperature Distribution with the Closure Coefficient c_{b1}

As previously stated, the internal flow computations are carried on using the HLLC method for the evaluation of convective fluxes. The numerical results for the shear flows parallel to the ablating wall shows that the HLL method is numerically diffusive. If the HLL is used for the coupled analysis, artificial diffusion of mass and energy

results in the increase of the mass fractions of the oxidizers and the temperature values near the wall. The recession rate on the throat point is calculated as 0.58 mm/s using the HLL method which is remarkably different from the measurement. Besides, the wall temperature is computed as 2488 K and 2240 K using the HLLC and HLL methods, respectively. The temperature and CO mass fraction distributions using the HLL and HLLC methods are compared in Figure 5.25.

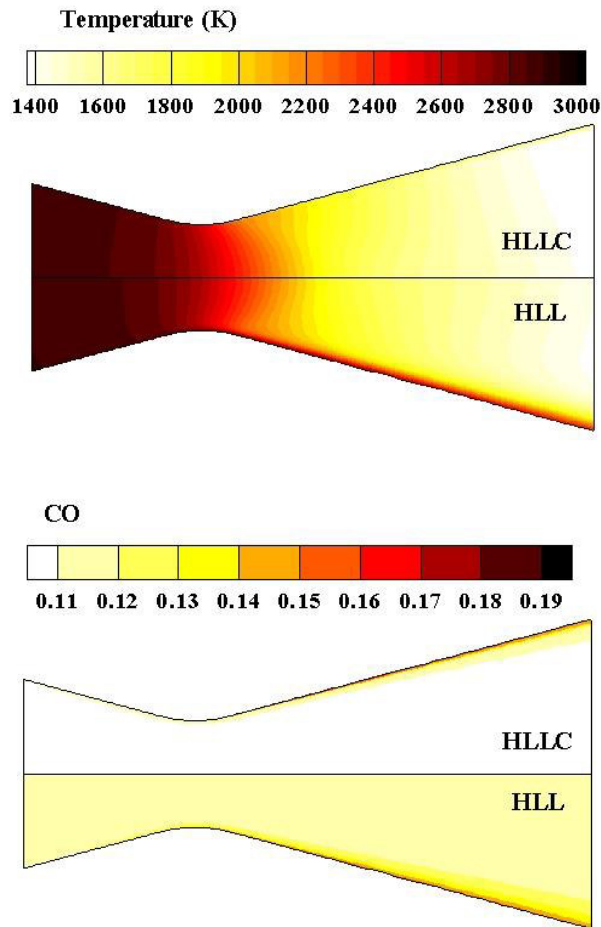


Figure 5.25. Diffusive Behavior of HLL Method for Shear Flow Parallel to the Ablating Wall

One of the firing tests of Evans et al [60] is the erosion rate measurement of a nozzle throat with a diameter of 1.016 cm and 18 % aluminized solid propellant. Firing duration is about 5 s and steady state recession rate of the effective throat is 0.084

mm/s. 191x61 and 191x51 structured grids are used for the fluid and solid domains, respectively and the views of the numerical grids are shown in Appendix B. Nozzle inlet flow conditions are given in Table 5.5. The mass fraction of the oxidizers are relatively low compared to the firing test with nonmetallized propellant. Total temperature of the nozzle inlet is 3500 K and the total pressure is about 77.2 Bar (7.72×10^6 Pa).

Table 5.5. Nozzle Inlet Conditions of the Test Case (Metallized Propellant) [7, 60]

Y_{CO}	Y_{CO_2}	Y_{HCl}	Y_{H_2}	Y_{H_2O}	Y_{N_2}	Y_{OH}	$P \times 10^{-5}$ (Pa)	T (K)
0.25	0.02	0.20	0.03	0.06	0.10	0.00	77.2	3500

Steady state and conjugate analyses are conducted for both frozen and reactive flow conditions and the throat erosion rates are computed as 0.103 and 0.106 mm/s, respectively. Comparisons of the erosion rate and temperature distributions are given in Figure 5.26 and Figure 5.27. In the reactive flow solution results, the wall temperature distribution is shifted about 30 K above the distribution of frozen flow results. The peak points of the erosion rate curves are before the throat point similar to the nonmetallized propellant case.

Comparisons of H_2O , CO_2 and CO distributions for frozen and reactive flows are shown in Figure 5.28. The minimum values of the water vapor and CO_2 are limited to 0.57 and 0.15 in the figures for a clear representation. H_2O mass fraction increases about 5 % in the core flow due to the gas phase reactions. Although the propellant is metallized and the total temperature is relatively high, H_2O is not totally consumed near the throat. The ratio of the water vapor decreases to 0.01 near the throat point and the maximum ratio is 0.063 inside the flow field. CO_2 mass fraction decreases just after the inlet of the nozzle and increases in the boundary layer close to the nozzle exit due to relatively low temperature and pressure values. CO_2 is a reactant of the ablation phenomena and the mass fraction on the throat is computed as 0.015 and 0.013 for frozen and reactive gas phase assumptions, respectively.

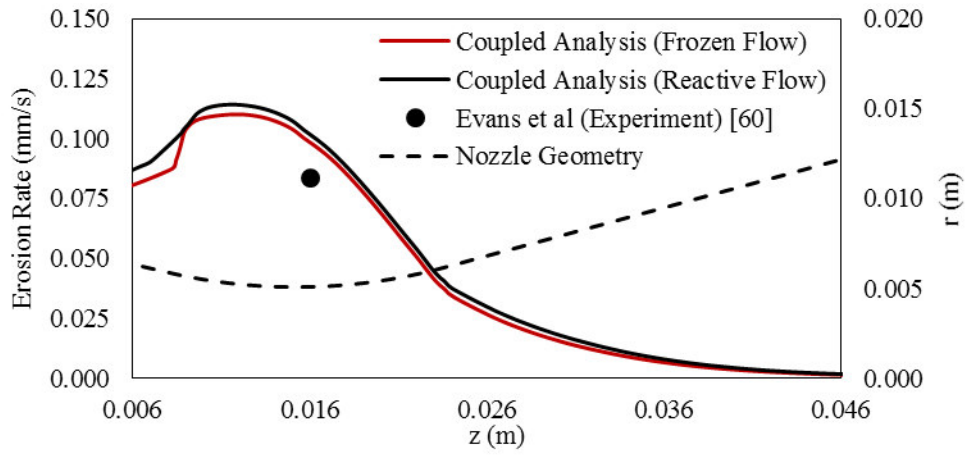


Figure 5.26. Comparison of Calculated Erosion Rate Distributions for Frozen and Reactive Flows (Spalart-Allmaras Turbulence Model, Metallized Propellant)

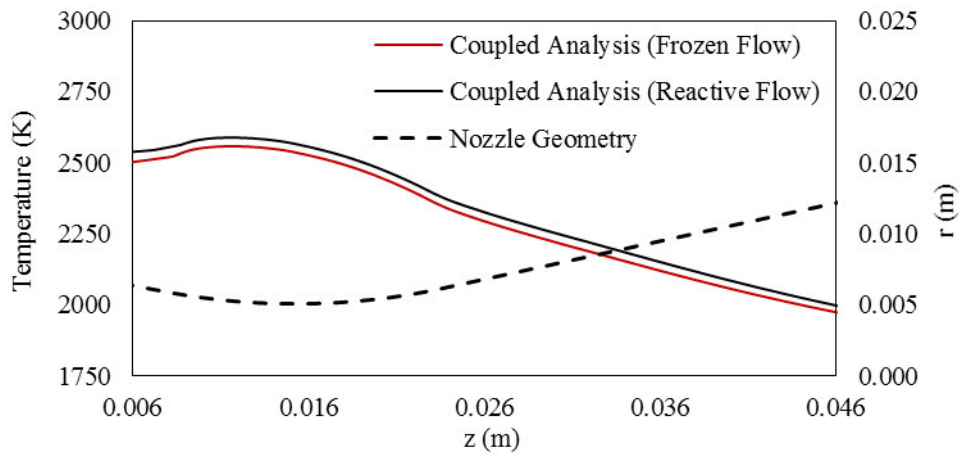


Figure 5.27. Comparison of Calculated Wall Temperature Distributions for Frozen and Reactive Flows (Spalart-Allmaras Turbulence Model, Metallized Propellant)

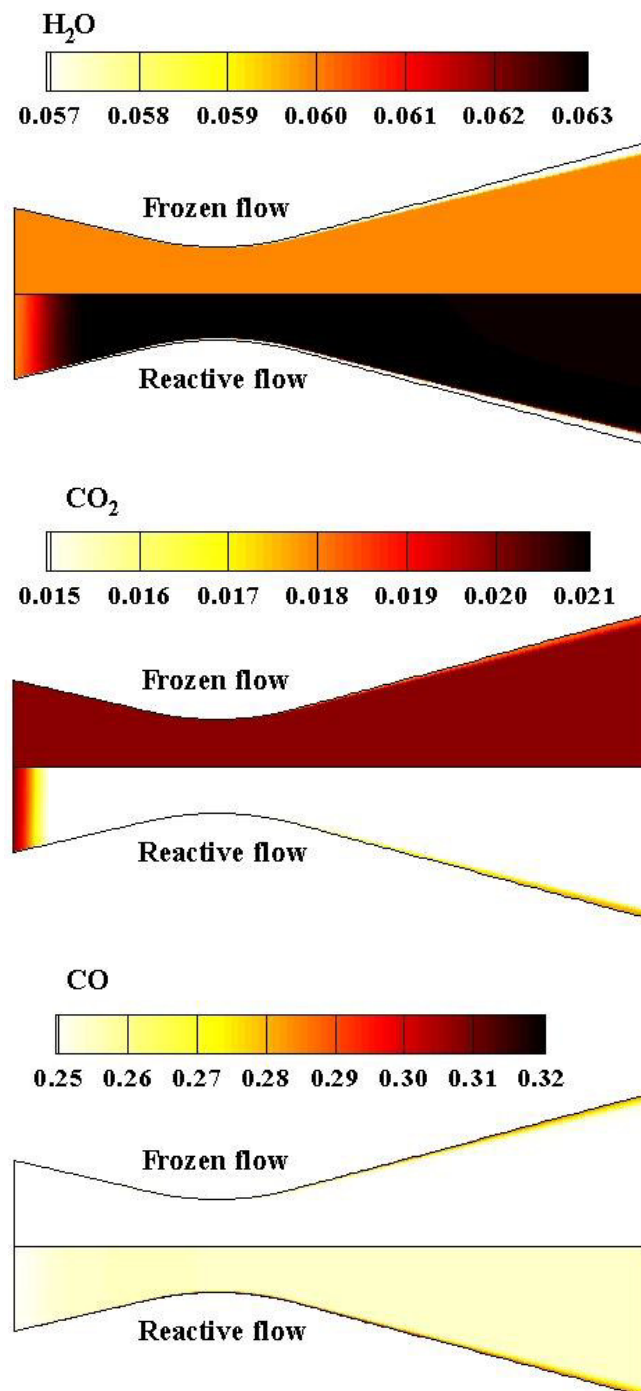


Figure 5.28. Comparison of Species Mass Fractions for Frozen and Reactive Flows (Spalart-Allmaras Turbulence Model, Metallized Propellant)

In Figure 5.29, the steady state temperature contours of fluid and solid domains are shown together with the close-up views near the ablating wall. The cooling effect of the injection of the ablation gases is clearly seen near the throat region. On the diverging section, the wall temperature is slightly higher than the core flow since the temperature is partially recovered near the wall.

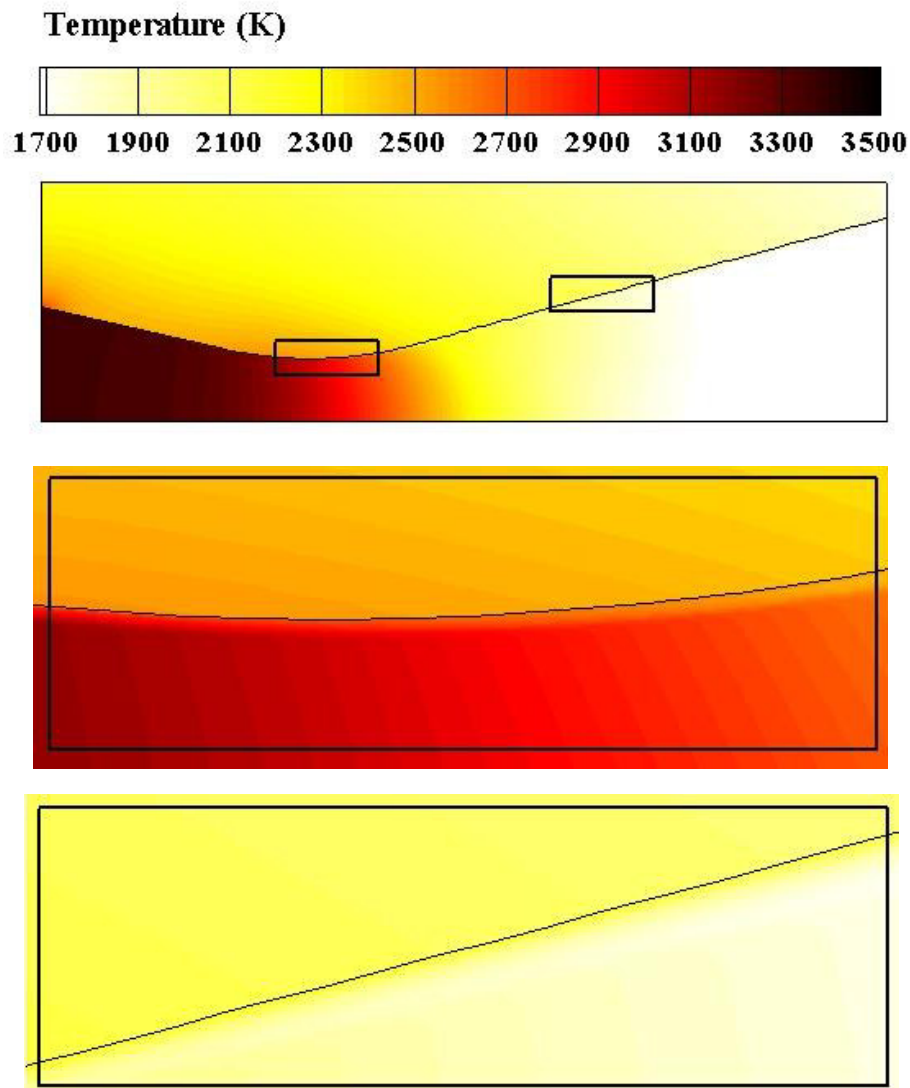


Figure 5.29. Temperature Contours inside the Fluid and Solid Domains (Frozen Flow, Spalart-Allmaras Turbulence Model, Metallized Propellant, Steady State Analysis)

5.4. Discussions on Internal Flow Solution Results

In chapter 5, initially the performance of the decoupled analysis is tested using equilibrium and finite rate approaches on the ablating wall. Then, a transient heating problem of a short firing duration test motor nozzle is solved including the effect of ablation. Finally, coupled analyses are performed for metalized and nonmetalized test motors and the results are compared with measurements and decoupled analysis calculations.

The decoupled analysis tool is a useful model for recession rate calculations since the computational cost is low and the error of the ablation results are usually below 10% for metalized propellants. Besides, using finite rate surface thermochemistry, transient heating analyses can be carried on with realistic computational times. However, the accuracy of the model decreases with decreasing temperatures and recession rates. The accuracy of the ablation results are increased via coupling the solid and fluid side analysis models. Effect of the turbulence on the conjugate analyses are compared. The contributions of the turbulence to the mass diffusion and thermal conductivity on the fluid side have dominant effects on the recession rate calculations. The results show that, the accuracy of the Spalart-Allmaras model is higher than the Baldwin-Lomax model. If Baldwin-Barth model is used for the turbulence closure, the behavior of the analysis tool becomes unpredictable due to stability problems and the discontinuities of the eddy viscosity inside the boundary layer.

In the numerical models of the current study, the geometries of the numerical domains are not changed during the calculations. The effect of the recession is included to the analyses using an advective term in the in-depth energy equation and average total pressure values are used for the inlet boundary conditions. For an eroding nozzle, increase of the radius of curvature on the throat and decrease of the total pressure are expected during the firing. Neglecting the geometrical changes might be one of the reasons of the overestimations in both decoupled and coupled models of the current study.

In their study on fully coupled ablation analysis, Thakre and Yang [7] state that the effects of the core flow chemical reactions are negligible for the recession rate computations. They have used a single step water-gas shift reaction in their model. A similar conclusion can be made referring to the results of the current modeling study with a more detailed gas phase reaction system. The change of the water vapor mass fraction due to chemical reactions is about 5 % and this species is the dominant oxidizer for the graphitic nozzles of SRM's.

CHAPTER 6

CONCLUSION AND FUTURE WORK

6.1. Conclusion

In this thesis, two multidimensional ablation models are developed for graphitic materials which are exposed to attack of reactive and high speed flows. In the first model, a decoupled approach is implemented excluding the effects of the ablation from the flow field solutions. Secondly, a conjugate analysis tool is developed via sharing the information and satisfying the ablation boundary condition on the interface between the solid and fluid domains. For all flow field analyses, Godunov type approximate Riemann solvers are used for the convective flux calculations. Viscous fluxes are computed using grid transformation metrics and three different turbulence models are implemented. The species diffusion terms are included in the Navier-Stokes equations. Models are tested for both external and internal flow conditions. Computational results are compared with the post-firing measurements of the throat diameter.

Wall equilibrium assumption is used for the external flow solutions. An implicit surface thermochemistry solver is developed and integrated with the in-depth and fluid flow analyses. Thus, requirement for the surface thermochemistry tables are eliminated and the preprocessing duration for the analyses are shortened. The results of the ablation computations for graphite in hypersonic flow show that the sublimation rate is highly sensitive to wall temperature variations and highly accurate wall temperature distributions can be achieved with the coupled analysis. Besides, detailed resolution of thermal boundary layer and species gradients using a conjugate approach avoids the lumped calculations of blowing rate distributions.

The decoupled analysis model which is developed for graphite in air problem is a fast and useful tool for preliminary design purposes. Although a slight overestimation of

stagnation wall temperature is observed, it is still possible to tune the mass and heat transfer approximations for future engineering purposes. The optimization of approximation coefficients is not in the scope of the current study but the decoupled model is promising for accurate computations for hypersonic vehicles which have smooth nose-tip curves without sharp and/or concave details.

The models which are developed in this study are also tested for the throats of the SRM nozzle inserts. Accurate results of recession rates are obtained for metallized propellants using the decoupled approach. Besides, if finite rate surface thermochemistry is used, the decoupled analysis tool enables the user to obtain time accurate temperature distributions inside the materials with reasonable computational times. On the other hand, the accuracy of the model decreases for low recession rates and low combustion chamber total temperatures. Using a coupled method with finite rate heterogeneous surface reactions enhances the coherence between the numerical and experimental results. Conjugate analysis results show that, turbulence closure approach has a significant role on the recession rate calculations since it determines the diffusion rates of the reactants from the boundary layer to the wall. Besides, increased turbulent viscosity effects the conduction inside the flow field and increases the rates of the surface reactions.

The ablation results of two different convective flux calculation methods are compared for the nozzle throat erosion problem. Selection of a diffusive method has tendency to yield highly inaccurate results for shear flows parallel to the ablating wall. The HLL solution result which is given in Section 5.3 is a typical example of this situation. This diffusive behavior might not be detectable for stagnating flow problems. On the other hand, replacement of the convective flux calculation method is the only way to handle the ill conditioned behavior in shear flows.

6.2. Future Work

The main focus of this study is the noncharring thermochemical erosion of the thermal protection system materials which are consist of pure carbon atoms. As previously stated, the coke residue of the pyrolysis of some charring materials are mostly composed of carbon atoms. Carbon-phenolic and ethylene-propylene-diene monomers (EPDM) are typical examples of this kind of insulation materials. Thus, the analysis tools which are developed for this thesis have potential for the computations of charring ablation problems via including the production of the pyrolysis gasses. Graphite erosion is a relatively slow phenomenon compared to charring ablation. The main challenge of a slow recession process is the correct modelling of the balance between the diffusive fluxes and the surface chemical kinetics. The effect of the ablating front movement is not included in the numerical models. The numerical grids are not evolved during the computations in order not to cope with stability problems. Rather; the accurate solutions of heterogeneous and homogenous reaction systems are focused together with the gas flow and solid conduction computations. The models for charring materials might require simulations including the effect of time accurate shape changes of the physical domains. One of the future aims is to develop a moving mesh scheme for a fully coupled charring ablation analysis tool.

In the models which are developed in this study, explicit time integration is implemented for both of the flow field and in-depth energy analyses and local time stepping is used for the steady state flow field calculations. The local time step sizes of the finite volume cells are decided referring to the CFL condition. The order of the possible maximum time steps are in the order of 10^{-8} s inside the boundary layer whereas reducing the time steps to the order of 10^{-4} s is usually enough for the solid conduction problem. The computational time for a coupled analysis with a reactive flow solution can reach up to 70 hours. One of the options for the reduction of the computational time is to parallelize the analysis tool. Another option is to replace the time integration scheme with an implicit method. Parallelization of an explicit code is

relatively more practical than changing the time integration scheme. Thus, the parallelization of the coupled analysis tool is one of the oncoming objectives.

Structured numerical grids are used for all of the computations in this study. For relatively simple geometries, production of these type of grids are usually practical and the coding workload is less compared to the unstructured solvers. Nevertheless, preprocessing times and the meshing workloads increase for detailed geometries. In the developed analysis tools, the selected numerical models other than the gradient calculation approach can be easily adapted for computations with unstructured grids and data structures. The replacement of the gradient calculation method is required for the conversion of the codes. It is planned to improve the data structure and the numerical models in order to result in analysis tools which can work with hybrid triangular and quadrilateral unstructured cells.

REFERENCES

- [1] Tauber, M. E., "Review of High-Speed, Convective, Heat-Transfer Computation Methods," NASA-2914, 1989.
- [2] Zoby, E. V., Moss, J. N., and Sutton, K., "Approximate Convective-Heating Equations for Hypersonic Flows," *Journal of Spacecraft*, Vol. 18, No. 1, 1981, pp. 64-70.
- [3] Bartz, D. R., "Heat Transfer from Rapidly Accelerating Flow of Rocket Combustion Cases and from Heated Air," New York Academic Press, Vol. 2, 1965.
- [4] Martin, A., Scalabrin, L., and Boyd, I. D., "High performance modeling of atmospheric re-entry vehicles," *Journal of Physics: Conference Series*, 341(1):012002, 2011.
- [5] Kuo, K. K. and Keswani, S. T., "A Comprehensive Theoretical Model for Carbon-Carbon Composite Recession," *Combustion Science and Technology*, Vol. 42, 1985, pp. 145-164.
- [6] Borie, V., Brulard, H., and Lengelle, G., "Aerothermochemical Analysis of Carbon-Carbon Nozzle Regression in Solid-Propellant Rocket Motors," *Journal of Propulsion and Power*, Vol 4, No 6, 1989, pp. 665-673.
- [7] Thakre, P., and Yang, V., "Chemical Erosion of Carbon-Carbon/Graphite Nozzles in Solid-Propellant Rocket Motors," *Journal of Propulsion and Power*, Vol. 24, No. 4, 2008, pp. 822–833.
- [8] Bianchi, D., Nasuti, F., and Martelli, E., "Coupled Analysis of Flow and Surface Ablation in Carbon–Carbon Rocket Nozzles," Bianchi, D., *Journal of Spacecraft and Rockets*, Vol 46, No 3, 2009, pp. 492-500.
- [9] Bianchi, D., Nasuti, F., and Onofri, M., "Thermochemical Erosion Analysis for Graphite/Carbon–Carbon Rocket Nozzles," *Journal of Propulsion and Power*, Vol. 27, No. 1, 2011, pp. 197-205.
- [10] Turchi, A., "A Gas-Surface Interaction Model for the Numerical Study of Rocket Nozzle Flows over Pyrolyzing Ablative Materials," Ph.D. Thesis, Università degli Studi di Roma "La Sapienza", 2013.
- [11] Cross, P. G., and Boyd, I. D., "Conjugate Analyses of Ablation in Rocket Nozzles," *Journal of Spacecraft and Rockets*, Vol. 56, No. 15, 2019, pp. 1-18.

- [12] Scalabrin, L. C., “Numerical Simulation of Weakly Ionized Hypersonic Flow Over Reentry Capsules,” Ph.D. Thesis, University of Michigan, Ann Arbor, 2007.
- [13] Wiebenga, J., and Boyd, I., “Computation of Multi-Dimensional Material Response Coupled to Hypersonic Flow,” AIAA Paper, 2012-2873, 2012.
- [14] Park, C., Jaffe, R. L., and Partridge, H., “Chemical-Kinetic Parameters of Hyperbolic Earth Entry,” AIAA Paper, 2000-0210, 2000.
- [15] Keenan, J. A., Candler, G. V., “Simulation of Ablation in Earth Atmospheric Entry,” AIAA Paper, 93-2789, 1993.
- [16] Kuntz, D. W., Hassan, B., and Potter, D. L., “Predictions of Ablating Hypersonic Vehicles Using an Iterative Coupled Fluid/Thermal Approach,” Vol. 15, No. 2, 2001, pp 129-139.
- [17] Wong, C. C., Blottner, F. G., Payne, J. L., and Soetrisno, M., “Implementation of a Parallel Algorithm for Thermochemical Nonequilibrium Flow Solutions,” AIAA Paper 95-0152, 1995.
- [18] Gartling, D. K., and Hogan, R. E., “COYOTE II – A Finite Element Computer Program for Nonlinear Heat Conduction Problems, Part I – Theoretical Background,” SAND-94-1173, 1994.
- [19] Powars, C. A., and Kendall, R. M., “User’s Manual – Aerotherm Chemical Equilibrium (ACE) Computer Program,” LEW-11722, 1972.
- [20] Chen, Y. K., Milos, F. S., Reda, D. C., and Stewart, D. A., “Graphite Ablation and Thermal Response Simulation under Arc-Jet Flow Conditions,” AIAA Paper 2003-4042, 2003.
- [21] MacCormack, R. W., “Current Status of Numerical Solutions of the Navier–Stokes Equation,” AIAA Paper 85-0032, 1985.
- [22] Chen, Y. K., Milos, F. S., “Finite-Rate Ablation Boundary Conditions for a Carbon-Phenolic Heat-Shield,” AIAA Paper 2004-2270, 2004.
- [23] Bianchi, D., Nasuti, F., and Martelli E., “Navier–Stokes Simulations of Hypersonic Flows with Coupled Graphite Ablation,” Journal of Spacecraft and Rockets, Vol. 47, No. 4, 2010, pp. 554-562.
- [24] Martin, A., and Boyd, I., D., “Strongly coupled computation of material response and nonequilibrium flow for hypersonic ablation,” AIAA Paper 2009-3597, 2009.

- [25] Martin, A., and Boyd, I. D., "Non-Darcian behavior of pyrolysis gas in a thermal protection system," *Journal of Thermophysics and Heat Transfer*, Vol. 24, No. 1, 2009, pp. 60-68.
- [26] Zhang, H., Reggio, M., Trepanier, J. Y., and Camarero, R., "Discrete form of the GCL for Moving Meshes and its Implementation in CFD Schemes", *Computers & Fluids*, Vol. 22, No. 1, 1993, pp. 9-23.
- [27] Milos, F. S., and Rasky, D. J., "Review of Numerical Procedures for Computational Surface Thermochemistry," *Journal of Thermophysics and Heat Transfer*, Vol. 8, No. 1, 1994, pp. 312–318.
- [28] van Leer, B., Harten, A., and Lax, P. D., "On Upstream Differencing and Godunov-Type Schemes for Hyperbolic Conservation Laws," *SIAM Review*, Vol. 25, No. 1, pp. 35-61, 1983.
- [29] Toro, E. F., "Riemann Solvers and Numerical Methods for Fluid Dynamics", Springer, pp. 115-162, 1997.
- [30] Baldwin, B. S., and Lomax, H., "Thin-Layer Approximation and Algebraic Model for Separated Turbulent Flows," *AIAA Paper 78-257*, 1978.
- [31] Baldwin, B. S., and Barth, T. J., "A One Equation Turbulent Transport Model for High Reynolds Number Wall-Bounded Flows," *NASA/TM-1990-102847*, 1990.
- [32] Spalart, P. R., and Allmaras, S. R., "A One Equation Turbulence Model for Aerodynamic Flows", *AIAA Paper 92-0439*, 1992.
- [33] Blazek, J., "Computational Fluid Dynamics: Principles and Applications", Elsevier, pp. 73-120, 2015.
- [34] Davis, S. F., "Simplified Second-Order Godunov-Type Methods", *SIAM Journal on Scientific and Statistical Computing*, Vol. 9, No. 3, 1988, pp. 445-473.
- [35] Hoffmann, K. A., "Computational Fluid Dynamics – Volume I", *Engineering Education System*, pp. 362-364, 2000.
- [36] McBride, B. J., Zehe, M. J. and Gordon, S., "NASA Glenn Coefficients for Calculating Thermodynamic Properties of Individual Species," *NASA/TP-2002-211556*, 2002.
- [37] Bird, R. B., Stewart W. E. and Lighfoot, E. N., *Transport Phenomena*, Second edition, Wiley, 2002, pp. 26-27.
- [38] Svehla, R. A., "Estimated Viscosities and Thermal Conductivities of Gases at High Temperatures", *NASA-TR-R-132*, 1966.

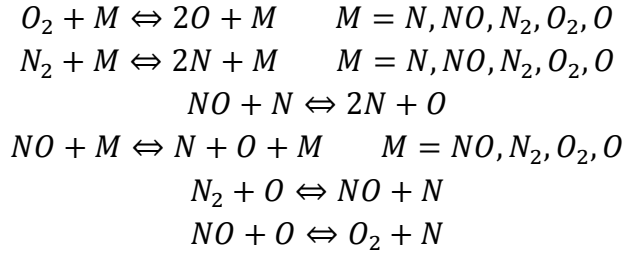
- [39] Landau, H. G., "Heat Conduction in a Melting Solid," *Quarterly of Applied Mathematics*, Vol. 8, No. 1, 1950, pp. 81-94.
- [40] Blackwell, B. F., and Hogan R. E., "One-Dimensional Ablation Using Landau Transformation and Finite Control Volume Procedure," *Journal of Thermophysics and Heat Transfer*, Vol. 8, No. 2, 1994, pp. 282-287.
- [41] Scala, S. M., and Gilbert, L. M. "Sublimation of Graphite at Hypersonic Speeds," *AIAA Journal*, Vol. 3, No. 9, 1965, pp. 1635-1644.
- [42] Baker, R. L., "Graphite Sublimation Chemistry Nonequilibrium Effects," *AIAA Journal*, Vol. 15, No. 10, 1977, pp. 1391-1397.
- [43] Bradley, D., Dixon-Lewis, G., Habik, El-Din, S., and Mushi, E. M., "The Oxidation of Graphite Powder in Flame Reaction Zones," 20th Symposium on Combustion, 1984, pp. 931-940.
- [44] Chelliah, H. K., Makino, A., Kato, I., Araki, N., and Law, C. K., "Modeling of Graphite Oxidation in a Stagnant-Point Flow Field Using Detailed Homogeneous and Semiglobal Heterogeneous Mechanisms with Comparisons to Experiments," *Combustion and Flame*, Vol. 104, No. 4, 1996, pp. 469-480.
- [45] McBride, B. J., and Gordon, S., "Computer Program for Calculation of Complex Chemical Equilibrium Compositions and Applications II. User's Manual and Program Description," NASA RP-1311-P2, 1996.
- [46] Geisler, R. L., "The prediction of graphite rocket nozzle recession rates," CPIA Publication, Vol. 5, 1981, pp. 173-196.
- [47] Eckert, E.R.G., "Survey on Heat Transfer at High Speeds", U.S. Air Force, ARL 189, 1961.
- [48] Ruperti N. J., Cotta R. M., Falkenberg C. V., SU J., "Engineering Analysis of Ablative Thermal Protection for Atmospheric Reentry: Improved Lumped Formulations and Symbolic – Numerical Computation," *Heat Transfer Engineering*, Vol. 25, No. 6, 2010, pp 101-111.
- [49] Amar, A. J., "Modeling of One-Dimensional Ablation with Porous Flow Using Finite Control Volume Procedure," MSc. Thesis, North Carolina State University, 2006.
- [50] Bianchi, D., "Modeling of ablation phenomena in space applications," Ph.D. Thesis, Universita degli Studi di Roma "La Sapienza", 2007.
- [51] Incropera, F. P., Dewitt, D. P., Bergman, T. L., Lavine, A. S., "Fundamentals of Heat and Mass Transfer, John Wiley & Sons, 6. Ed., 2007, pp. 272-274.
- [52] MacLean, M., "An Equilibrium Ablation Boundary Condition for the Data-Parallel Line-Relaxation Code" AIAA Paper 2013-0304, 2013.

- [53] Candler, G. "Nonequilibrium Processes in Hypervelocity Flows: An Analysis of Carbon Ablation Models", AIAA Paper 2012-724, 2012.
- [54] Gupta, R.N., Yos, J. M., Thompson, R.A. and Lee, K., "A Review of Reaction Rates and Thermodynamic and Transport Properties for an 11-Species Air Model for Chemical and Thermal Nonequilibrium Calculations to 30000 K", NASA-RP-1232, 1990.
- [55] Park, C., "Review of Chemical-Kinetic Problems of Future NASA Missions, II: Earth Entries. Journal of Thermophysics and Heat Transfer", No. 7, Vol. 3, 1993, pp. 385-398.
- [56] Schneider, D., Genin, C., Karl, S., Hannemann, V., "A Numerical Model for Nozzle Flow Application under LOX/CH₄ Hot Flow Conditions," AIAA Paper 2016-4671, 2016.
- [57] Lobb, R. K., "Experimental Measurement of Shock Detachment Distance on Spheres Fired in Air at Hypervelocities," AD0284378, Naval Ordnance Lab, 1962.
- [58] Yumusak, M., and Eyi, S., "Aerothermodynamic Shape Optimization of Hypersonic Blunt Bodies", AIAA Paper 2013-2693, 2012.
- [59] Onay, O. K., and Eyi, S., "Ablation Analyses of Optimized Nose-Tips for Hypersonic Vehicles", Journal of Thermophysics and Heat Transfer, No. 34, Vol. 1, 2020, pp. 78-89.
- [60] Evans, B., Kuo, K. K., Ferrara, P. J., Moore, J. D., Kutzler, P., Boyd, E., "Nozzle Throat Erosion Characterization Study Using a Solid-Propellant Rocket Motor Simulator," AIAA Paper 2007-5776, 2007.

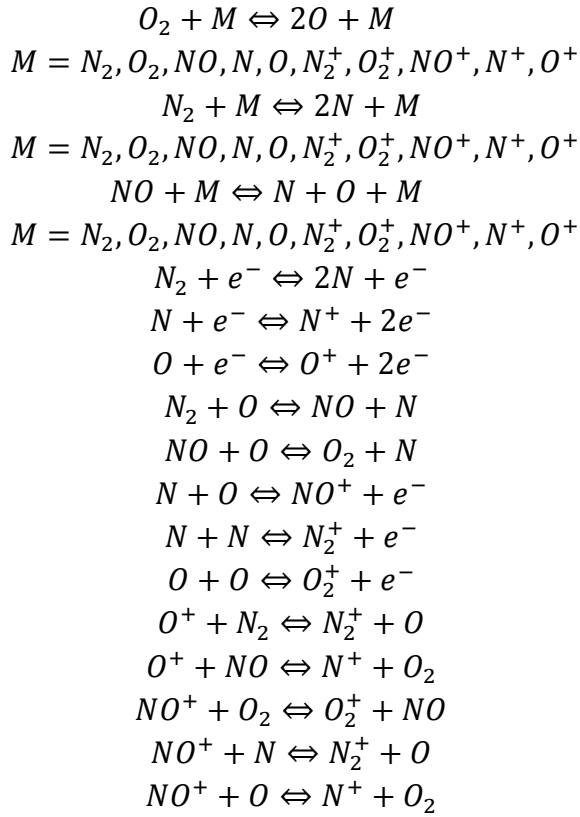
APPENDICES

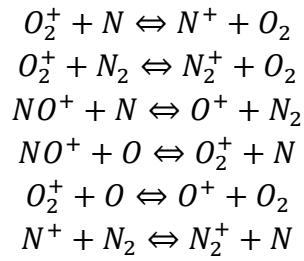
A. Flow Field Chemical Reactions

Air Reactions, 17 Step Mechanism

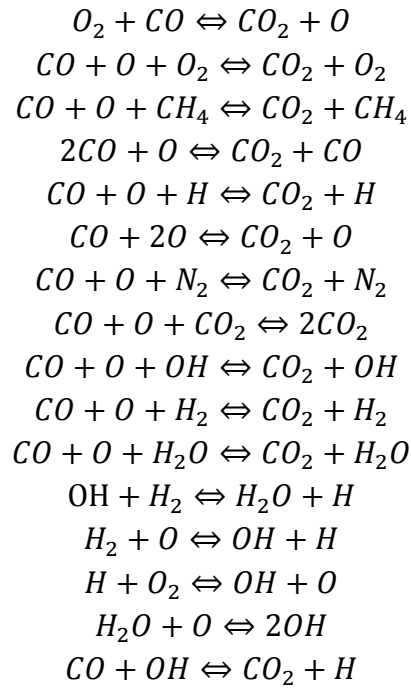


Air Reactions, 49 Step Mechanism





SRM Nozzle Reactions, 16 Step Mechanism
(CH₄ excluded in the flow field analysis)



B. Numerical Grids

Figure B.1 Grids for Grid Convergence Study - Aerothermodynamics Analysis

Model Validation

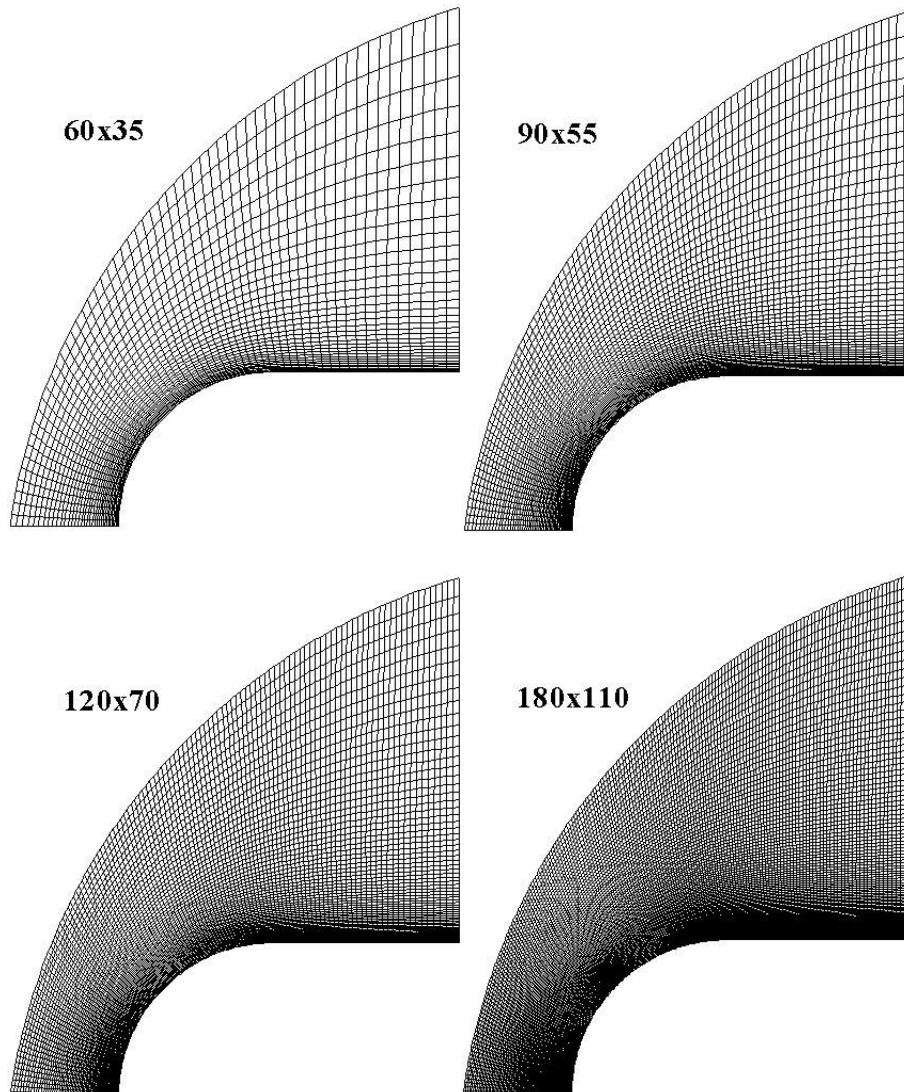


Figure B.2 Grids for Grid Convergence Study and Graphite in Air Ablation Analysis

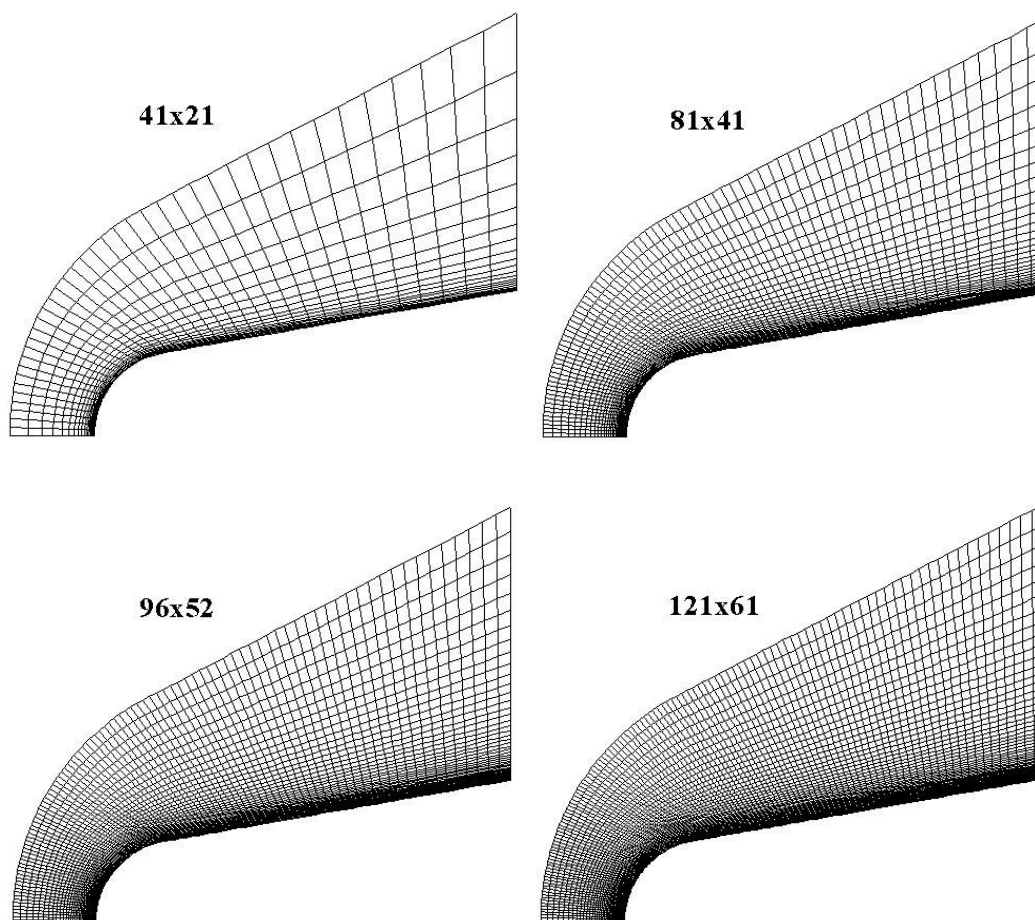


Figure B.3 Grid for Ablation Analysis of Drag Optimized Geometry

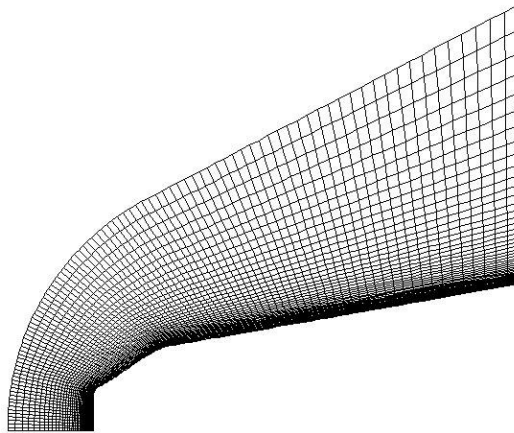


Figure B.5 Grid for Ablation Analysis – Graphite in SRM Nozzle (Decoupled Model
– Metallized Propellant)

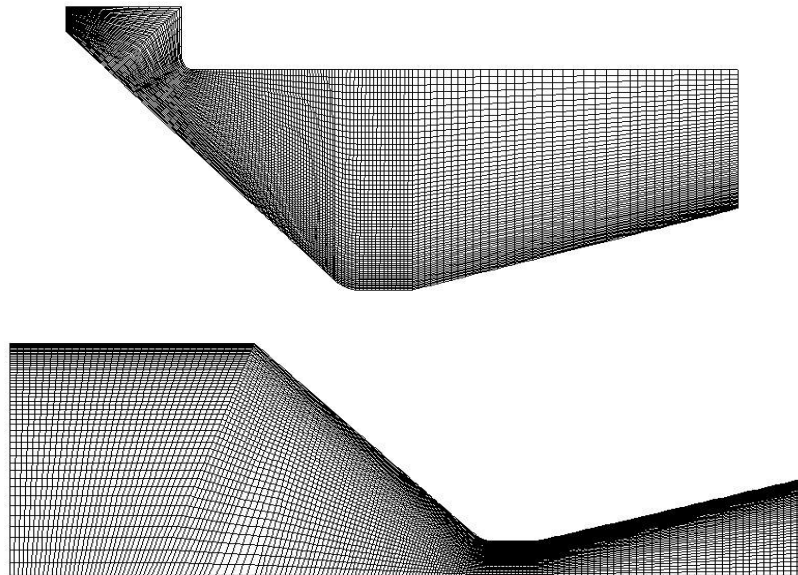


Figure B.6 Grids for Ablation Analysis – Graphite in SRM Nozzle (Decoupled and
Coupled Model – Nonmetallized Propellant)

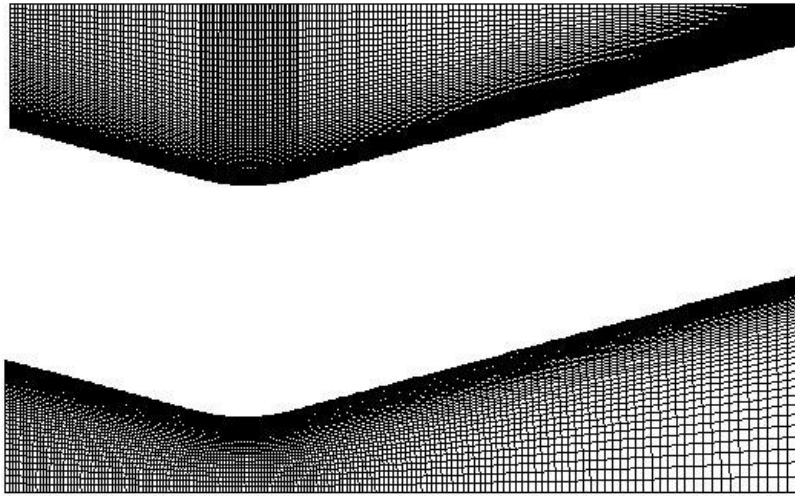
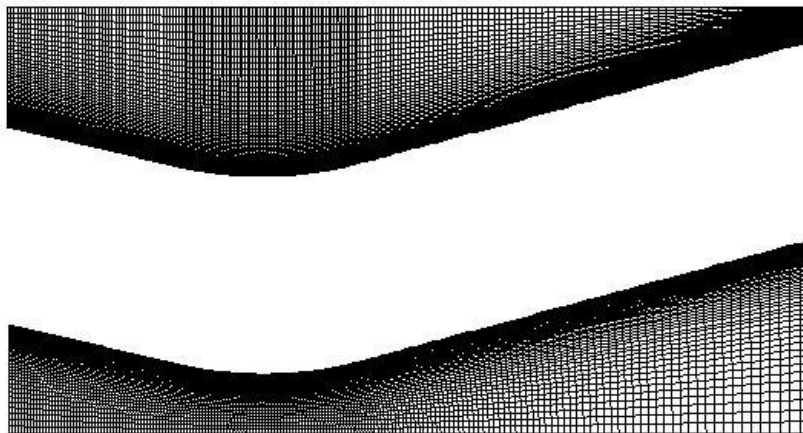


Figure B.7 Grids for Ablation Analysis – Graphite in SRM Nozzle (Coupled Model
– Metallized Propellant)



CURRICULUM VITAE

PERSONAL INFORMATION

Surname, Name : Onay, Oğuz Kaan
Nationality : Turkish (TC)
Date and Place of Birth : 30 March 1986, Sakarya
Phone : +905554775999
E-mail : e163523@metu.edu.tr

EDUCATION

Degree	Institution	Year of Graduation
MS	METU Aerospace Engineering	2013
BS	METU Mechanical Engineering	2009
High School	Zonguldak Science High School, Ankara	2004

WORK EXPERIENCE

Year	Place	Enrollment
2017-Present	ROKETSAN A.S.	Senior Expert Engineer
2014-2017	Middle East Technical University	Research Assistant
2013-2014	Vestel Defence Industry	R&D Engineer
2009-2013	Turbotek Limited Co.	Project Engineer

FOREIGN LANGUAGES

Advanced English, Elementary Arabic

PUBLICATIONS

Journal

Onay, O. K., Eyi, S., “Ablation Analyses of Optimized Nose Tips for Hypersonic Flows,” Journal of Thermophysics and Heat Transfer, No. 34, Vol. 1, 2020, pp. 78-89.

Conference Papers

Onay, O. K., Eyi, S., “Implicit Solution of One-Dimensional Transient Ablation,” AIAA Paper 2015-3882, AIAA Propulsion and Energy Forum, July 27-29 2015, Orlando, Florida, USA.

Onay, O. K., Eyi, S., “Adjoint Shape Optimization of Hypersonic Blunt Bodies Including the Effect of Graphite Ablation,” 9th International Conference on Computational Fluid Dynamics (ICCFD9), July 11-15 2016, Istanbul, TURKEY.

Onay, O. K., Eyi, S., “Transient Thermochemical Erosion Modeling for Solid Propellant Rocket Motor Nozzles Including the Effect of Shape Change and Anisotropy,” AIAA Paper 2018-3719, AIAA Aviation Forum, June 25-29 2018, Atlanta, Georgia, USA.

Onay, O. K., Eyi, S., “Comparison of Fully Coupled and Decoupled Modeling Results of Graphite Ablation in Hypersonic Flows,” 10th Ankara International Aerospace Conference, September 18-20 2019, Ankara, TURKEY.

Poster Presentation

Onay, O. K., Özen, G., Yumusak, M., Eyi, S., “Solid Rocket Motor Nozzle Erosion Modeling using Finite Rate and Equilibrium Methods,” 9th Ablation Workshop, August 30-31 2017, Bozeman, Montana, USA.